Nanoscale Thermal Transport Phenomena in Superstructured Semiconductors

A Study of Heat Transfer in Superatomic, Nanocrystalline,

and 2D Perovskite Structures

Submitted in partial fulfillment of the requirements for the degree of

Doctor of Philosophy

in

Mechanical Engineering

Alexander D. Christodoulides

B.S., Mechanical Engineering, University of Miami

M.S., Mechanical Engineering, Carnegie Mellon University

Carnegie Mellon University

Pittsburgh, PA

May 2022

Acknowledgements

I believe that a doctoral degree is rarely a singular effort, and that one's success relies almost entirely on those around them. No amount of solitary study can amount to the insights gained from conversation with friends, family, colleagues, and mentors. I rely heavily on the support given by those around me (from which they typically gain little or nothing of actual value) and I am confident that the material in this document would not be possible if not for their generosity and wisdom. I therefore extend my gratitude to the following people for their contributions, be them intellectual, physical, emotional, or otherwise:

- My family, without whom I would not exist
- My advisor, Jonathan A. Malen, for his unending support to this work and to me as a person, and for facilitating my growth as a student, researcher, and scientist
- Alan J.H. McGaughey, who served as a mentor and guided my progress as a doctoral student every step of the way
- My committee members, Jonathan A. Malen (chair), Alan J.H. McGaughey, Xavier Roy, and Shawn Litster, for their instrumental part in creating and refining this document.
- My lab mates (past and present), particularly Dipanjan Saha, Matthew Bartnof, Wee-Liat Ong, Henry Aller, Minyoung Jeong, Kevin Parrish, Lingyun Dai, and Yuxing Liang for their mentorship and guidance
- My colleagues and close friends S. Arman Ghaffarizadeh and Nicholas Maier for offering commiseration
- My collaborators, whose scientific contributions allowed for this research to be possible,

  - Evan S. O'Brien, Jake C. Russell, Xavier Roy, Jingjing Yang, and Colin Nuckolls in the Department of Chemistry at Columbia University,
  - Peijun Guo, Richard D. Schaller, Justin M. Hoffman, and Alexandra Brumberg in the Department of Chemistry at Northwestern University,
  - Zhongyong Wang and Robert Wang in the Materials Science Engineering and Chemical Engineering Department at Arizona State University,
  - Rahil Ukani, Ryan McGillicuddy, and Jarad Mason in the Department of Chemistry and Chemical Biology at Harvard University
- My partner, Asal Yunusova, for her invaluable and unwavering support during the tumultuous final months of my Ph.D.
- The Army Research Office for supporting this work through Grant No. W911NF-17-1-0397
- The Wilton E. Scott Institute for Energy Innovation for the resources (financial and experimental) made available for this work
- Neil and Jo Bushnell, whose generous fellowship helped fund this work
- Jean-Francois and Catherine Heitz, whose scholarship allowed this research to take place

Abstract

Nanoscale Thermal Transport Phenomena in Superstructured Semiconductors

A Study of Heat Transfer in Superatomic, Nanocrystalline, and 2D Perovskite Structures

Alexander D. Christodoulides

Chair: Professor Jonathan A. Malen

The underlying transport phenomena that dictate properties like thermal conductivity have been extensively investigated in small unit cell semiconductors and metals. However, more complex structures have received less attention. Here, we investigate heat transfer in superstructures, or materials with nanometer-scale periodicities that are longer than those seen in atomic crystals. We use a combination of theoretical, experimental, and modeling techniques to elucidate thermal transport mechanisms in superatomic structures, colloidal nanocrystals, and two-dimensional perovskites. Most notably, we use frequency-domain thermoreflectance to measure thermal conductivity in single crystal and thin film samples. Our results in certain superatom and perovskite materials are indicative of ordered-to-disordered phase transitions and coherent phonon transport. Our work highlights the tunability of all three groups of materials and emphasizes multifunctionalities that may be exploited in the design of next-generation photovoltaic, optoelectronic, and thermoelectric devices. Additionally, we shed light on phonon transport behaviors that result in ultralow thermal conductivities on the order of the lowest ever measured in fully-dense solids. Our results may be helpful towards a deeper understanding of thermal transport in superstructures as well as towards the development of novel technologies that are able to either functionalize or manage the heat transfer characteristics we observe.

Table of Contents

List of Figures

List of Symbols/Abbreviations

q – heat flux per unit area ($W \cdot m^{-2}$)

k, κ – thermal conductivity ($W \cdot m^{-1}K^{-1}$)

T – temperature (K, °C)

ρ – density ($kg \cdot m^{-3}$)

C_p/C_v – heat capacity at constant pressure/volume ($J \cdot m^{-3}K^{-1}$)

$\hbar$ - reduced Planck constant ($J \cdot s \cdot rad^{-1}$)

ω – frequency ($rads^{-1}$, Hz)

k_B – Boltzmann constant

v – phonon group velocity ($m \cdot s^{-1}$)

Λ –phonon mean free path (m)

S_β – normalized sensitivity

θ_{lag} – phase difference (deg, rad)

$\bar{u}$ – parameter uncertainty

E – Young's modulus (Pa)

n – identifier of organic or inorganic layer thickness of perovskites

FDTR – frequency-domain thermoreflectance

SAC – superatomic crystal

NCSL – nanocrystal superlattice

NCF – nanocrystal film

EMA – effective medium approximation

HOIP – hybrid organic-inorganic perovskite

PCE – power conversion efficiency

RP – Ruddlesden-Popper

BCE – barocaloric effect

1 Introduction

1.1 Fundamentals of Nanoscale Heat Transfer

Heat transfer is broadly concerned with the transmission of thermal energy, or heat, from one body or space to another. The main mechanisms by which heat is transferred are conduction, convection, and radiation. Conduction is the movement of heat in systems resulting from the random collision and resulting energy exchange of micro- and nanoscopic particles, or energy carriers. One-dimensional thermal conduction is often described as diffusive, where heat travels from hot regions to cold ones. Convection, while typically considered isolated from conduction, is in reality a combination of conduction (random motion of particles) and advection (collective motion, or bulk flow). Convection is a major contributor to the overall exchange of heat between systems composed of gases and liquids. The final mode is radiation, or heat transfer *via* electromagnetic radiation. Bodies are able to interact with one another without a medium by radiation exchange through the absorption, reflection, or emission of photons. Radiation is particularly important in vacuum environments that suppress conduction and convection, such as space.

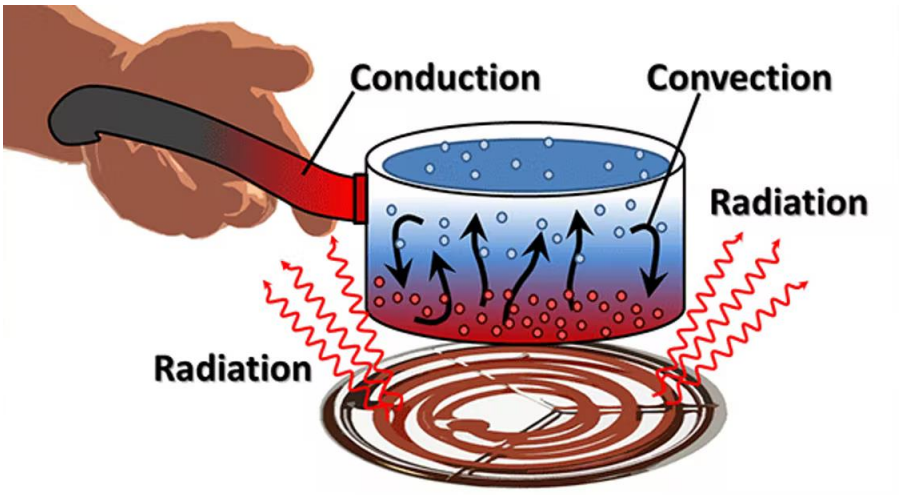

Figure 1.1. All three of the main mechanisms of heat transfer are involved in boiling water. The hot coil turns red, emitting photons that are absorbed by the pot as heat. The heat is transferred to the water at the bottom of the pot, which begins to flow due to the effects of natural convection. Excess heat is transferred to the user's hand *via* conduction from the hot water to the pot handle (image courtesy of MachineDesign.com).

In this document we will explore elements of thermal conduction, convection, and radiation, however the discussion will be primarily relegated to conduction as it is the mode that dictates heat transfer within fully-dense solids. The macroscopic theory of diffusive heat conduction is centered around the Fourier law, which identifies a linear relationship between the heat flux ($\boldsymbol{q}$) and temperature gradient ($\nabla \boldsymbol{T}$) in a system, as shown in Eq. 1.1.1.

$$\boldsymbol{q} = -k\nabla \boldsymbol{T} \qquad 1.1.1$$

Here, the constant of proportionality is the thermal conductivity, or k, which is a material dependent property that describes the ability of heat to travel within it. Naturally, the higher the

thermal conductivity, the better heat will be able to propagate. Inherent to the Fourier law, captured mathematically by the minus sign, is the notion that heat will travel opposite the direction of the temperature gradient, meaning that it will always flow from the region of lower temperature to that of higher temperature.

The Fourier law and thermal conductivity are massively important for engineering and design purposes and are widely accepted concepts in most macroscopic applications. This simple law is the basis of the heat diffusion equation, reproduced as Eq. 1.1.2.

$$\frac{\partial}{\partial x}\left(k\frac{\partial T}{\partial x}\right)+\frac{\partial}{\partial y}\left(k\frac{\partial T}{\partial y}\right)+\frac{\partial}{\partial z}\left(k\frac{\partial T}{\partial z}\right)+\dot{q}=\rho c_p\frac{\partial T}{\partial t} \qquad 1.1.2$$

This equation, sometimes simply known as the heat equation, can be solved given initial/boundary conditions and other system characterizations (i.e. thermal conductivity, volumetric internal energy generation) for the temperature distribution as a function of time of a system as governed by conductive thermal transport. The heat diffusion equation is ultimately a descriptor of energy conservation and is of utmost importance in most heat transfer applications.

Unsurprisingly, thermal conductivity is a significantly more complex concept than the Fourier law, as represented in Eq. 1.1.1, would imply. Thermal conductivity spans several orders of magnitude; at room temperature it can be as low as $0.05\ \mathrm{Wm^{-1}K^{-1}}$ in gases like air and as high as $2000\ \mathrm{Wm^{-1}K^{-1}}$ in ultra-stiff materials like diamond. Moreover, thermal conductivity and other thermophysical properties (i.e. heat capacity, density, thermal diffusivity and effusivity) exhibit significant temperature dependencies that make quantifying heat transfer *via* the Fourier law difficult without the use of advanced numerical and computational tools. A deep understanding of the underlying principles that dictate these important quantities is therefore needed.

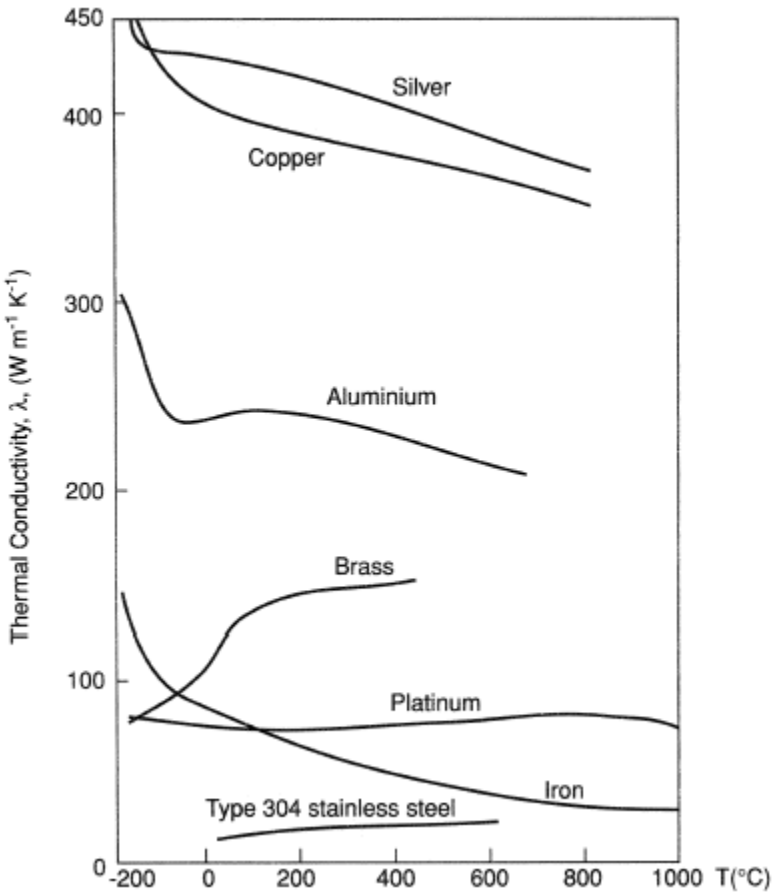

Figure 1.2. Thermal conductivity, here expressed as λ, of multiple metals across a wide range of temperatures. Dependencies on temperature are often highly nonlinear and exhibit non-monotonic trends (courtesy of thermopedia.com).

Thermal conductivity results from the movement and collisions of so-called 'heat carriers' within a system. As the term implies, heat carriers are molecules or other basic particles that carry energy that may manifest as heat, and includes species such as electrons, phonons, and photons. The heat carrier that dominates thermal conductivity is dependent on the system itself. Heat conduction in metals and other electrical conductors (materials for which there exists no electronic

bandgap) is overwhelmingly characterized by electrons. By contrast, phonons largely dictate thermal conductivity in non-metals such as semiconductors and insulators (for which electrical band gaps exist) since free electron density is greatly reduced. In this work we pay special attention to semiconducting materials, and a discussion of phonons is therefore necessary.

Phonons are quasiparticles that quantize the collective motion and vibration of atoms in a solid system. They conform to the wave-particle duality of elementary particles and are thus characterized by particle-like descriptors such as group velocity and momentum and simultaneously by wave-like descriptors such as frequency and wavevector. Furthermore, phonons behave as bosons, meaning that theoretically, unlike in systems of fermions, a single phonon state may be occupied infinitely. The occupation is, however, determined by the Bose-Einstein distribution reproduced in Eq. 1.1.3.

$$\langle n_{K,p} \rangle = \frac{1}{\exp\left(\frac{\hbar\omega_{K,p}}{k_B T}\right) - 1} \qquad 1.1.3$$

Here, $\langle n_{K,p} \rangle$ represents the number of phonons that occupy a state of wavevector K and polarization p, ω represents the phonon state energy, $\hbar$ represents the Planck constant, k_B represents the Boltzmann constant, and T represents the absolute temperature.

A phonon state, more commonly referred to as a phonon mode, is a vibrational wave within a crystalline solid of a specific wavevector and frequency. The sum of all modes that exist within a system dictate heat capacity and thermal conductivity within semiconducting and insulating materials. This can be represented conveniently in the dispersion relation, which relates phonon mode energy to wavevector, as shown in Fig. 1.3 for a diatomic chain.

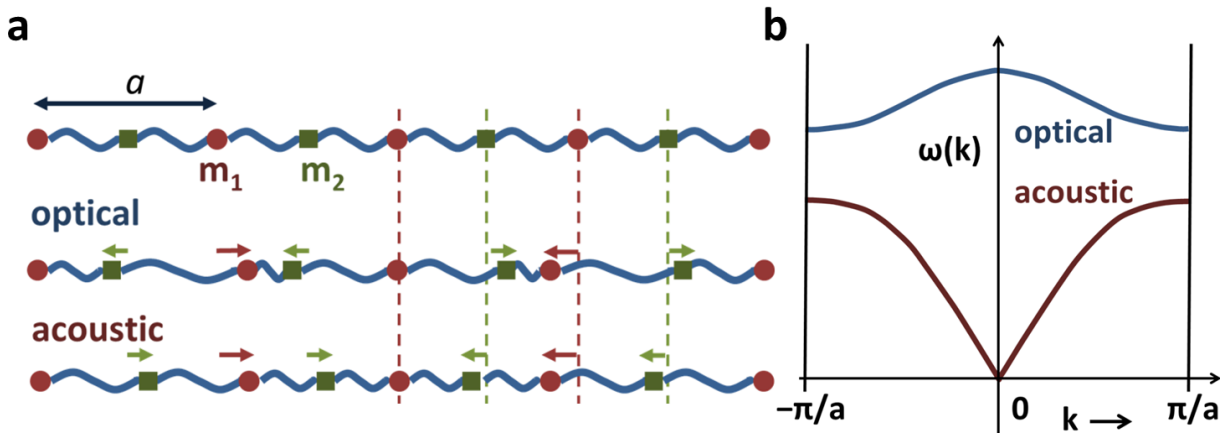

Figure 1.3. a) Phonon modes describe the collective vibration of atoms or molecules in a crystal lattice. This one-dimensional diatomic chain (for which the unit cell length is a) has two types of phonon modes: optical modes that describe vibrations in which neighboring atoms moving in alternating directions and acoustic modes in which, due to their low frequency, describe vibrations that move nearly synchronously. b) These modes are defined by precise wavevectors (represented in the figure by k) and frequencies (ω) within the first Brillouin zone, defined by ±π/a (courtesy of wikipedia.com).

The heat capacity at constant volume is defined as

$$C_V \equiv \left(\frac{\partial U}{\partial T}\right)_V \qquad 1.1.4$$

where U is the system internal energy and T is the temperature. The contribution of phonons to heat capacity (sometimes referred to as lattice heat capacity) is quantified based on the lattice energy:

$$U_{lat} = \sum_{K} \sum_{p} \langle n_{K,p} \rangle \, \hbar\omega_{K,p} \tag{1.1.5}$$

The summation over wavevectors may be replaced so that the expression is written in terms of the change in the quantity of modes per change in energy level, otherwise known as the density of states $D_p(\omega)$.

$$U_{lat} = \sum_{p} \int d\omega \, D_p(\omega) \frac{\hbar\omega}{\exp\left(\frac{\hbar\omega}{k_B T}\right) - 1} \tag{1.1.6}$$

If the substitution of $x = \frac{\hbar\omega}{k_B T}$ is made, Eq. 1.1.4 can be used to determine the lattice heat capacity:

$$C_{V,lat} = k_B \sum_{p} \int d\omega \, D_p(\omega) \frac{x^2 \exp(x)}{[\exp(x) - 1]^2} \tag{1.1.7}$$

The Debye model for the density of states relates the dispersion relation to the wavevector linearly *via* the speed of sound, which is constant across all polarizations, such that $\omega = vK$. The density of states if therefore

$$D(\omega) = \frac{dN}{d\omega} = \frac{VK^2}{2\pi^2} \frac{dK}{d\omega} = \frac{V\omega^2}{2\pi^2 v^3} \tag{1.1.8}$$

where N represents the number of modes having a wavevector equal to or less than K and V represents the volume of the model system.

If the phonon velocity is independent of polarization then the summation in Eq. 1.1.7 can be replaced by a factor of 3. Once this is done, the expression becomes

$$C_{V,lat} = 9Nk_B\left(\frac{T}{\theta}\right)^3 \int_0^{\theta/T} dx \frac{x^4 e^x}{(e^x - 1)^2} \qquad 1.1.9$$

where θ represents the Debye temperature, or the temperature at which the highest frequency acoustic phonon mode become occupied:

$$\theta = \frac{\hbar v}{k_B}\left(\frac{6\pi^2 N}{V}\right)^{1/3} \qquad 1.1.10$$

The Debye temperature of a material is a critical quantity as it generally represents the upper limit to phonon activation. While high frequency optical modes may remain inactive at this temperature, they generally contribute less to heat capacity and thermal conductivity than the acoustic modes and are therefore typically less important. Accordingly, understanding the Debye temperature is often useful in describing heat storage and transport phenomena in non-metals.

Thermal conductivity due to phonons (otherwise sometimes called lattice thermal conductivity) is related to their velocity and scattering rate. Conduction is the diffusive nature of thermal energy transport due to the random motion and consequent collision of heat carriers (which

are primarily phonons in semiconductors). The kinetic theory of gases can therefore be applied to develop an expression for thermal conductivity:

$$k = \frac{1}{3} C_V \bar{v} \bar{\Lambda} \qquad 1.1.11$$

where $\bar{v}$ is the average phonon group velocity and $\bar{\Lambda}$ is the average mean free path of all active phonons. Eq. 1.1.11 can be substituted into the Fourier law (Eq. 1.1.1) to create an equation that describes conductive heat flux in terms of a phonon gas[1,2].

$$\boldsymbol{q} = -\frac{1}{3} C_V v \Lambda \nabla \boldsymbol{T} \qquad 1.1.12$$

Eq. 1.1.12 presumes isotropic thermal transport in each direction, which we will see is often not the case. This expression will be used throughout the text as a basis for hypothesis and the foundation for understanding heat transfer in the complex material systems that will be introduced.

1.2 Applications and Areas of Interest

Devices that are developed and researched today such as computer chips often contain extremely small components with dimensions on the order of microns or nanometers. The continuum picture of heat transfer typically fails to capture the transport and storage phenomena present at this scale[3]. Researchers therefore focus on analyses and experimentation that are reliant on nanoscale considerations to yield more accurate predictions. These same concepts and practices

are also often useful in understanding thermal transport in situations where more conventional experimentation and modeling is difficult, such as in extreme temperatures and complex structures.

The fruits of the study of nanoscale heat transfer are evident in many fields of engineering, materials science, and chemistry. One of the highest thermal conductivities of $3500\ \mathrm{Wm^{-1}K^{-1}}$ was measured when a group of researchers successfully suspended a single-walled carbon nanotube (SWNT) between two metal contacts. Such a discovery had not previously been possible due to limitations in CNT synthesis and nanofabrication techniques at the time. The group reasoned that the trend they observed was due to a combination of Umklapp scattering and three phonon scattering processes[4]. Another team took a similar approach to measure the thermal conductivity of single-layer graphene and found it to be as high as $5300\ \mathrm{Wm^{-1}K^{-1}}$ [5]. On the opposite end of the spectrum, non-contact laser techniques have allowed for the discovery of ultra-low thermal conductivity materials. One study used time-domain thermoreflectance (TDTR) to measure the thermal conductivity of WSe_2, finding it to be as low as $0.05\ \mathrm{Wm^{-1}K^{-1}}$ [6]. Other groups have used similar techniques to measure PCBM and found its thermal conductivity to be below $0.06\ \mathrm{Wm^{-1}K^{-1}}$as a result of amorphous-regime scattering mechanisms[7–9].

These experimental and computational results are critical to the successful implementation of novel materials in next-generation devices. Thermal management is a core component of design of new devices used in electronics, electro-optics, thermoelectrics, photovoltaics. Such technologies often operate at extremely high powers per unit area, especially in localized hot spots, and are therefore prone to thermally induced degradation and even potential burning/melting[10]. Consequently, this area of research not only aims to elucidate the fundamental nature of thermal transport at small scales but also to aid in the advancement of technology by addressing thermal bottlenecks in all facets of engineering design, from microelectronics to nuclear reactors.

1.3 Thermal Transport in Superstructures

Much of the characterization of nanoscale transport, storage, and conversion phenomena has been relegated to popular small unit cell materials like silicon, carbon allotropes, perovskites, GaAs/GaN, and simple metals. This is because simpler materials are not only easier to create, but also easier to understand in terms of electronic and phononic behaviors. Fewer atoms per unit cell allows for modeling and simulation research to encapsulate more of the dynamics between modes (since more high energy modes can be calculated), including three-phonon and even four-phonon interactions[11]. However, there is an ever-increasing need for characterization of more complex structures that have larger unit cells owing to their layered or otherwise nano-patterned nature.

Much of this document will focus on three superstructured material classes: superatoms, two-dimensional perovskites, and nanocrystals. Broadly, the term superstructure is used to refer to a wider class of material defined by nanoscale periodicity that exceeds the length scales associated with atomic crystals. This periodicity may exist in one dimension, as is the case in most superlattices, two dimensions, such as in a forest of nanotubes, or in three dimensions, like in a nanoparticle or nanocage system.

Superatomic structures are defined by precisely composed clusters of atoms that are periodically spaced from one another and often conjoined by ligands that extend from the outer surface of the material. Colloidal nanocrystals are similarly sized but exhibit polydispersity in the total number of atoms per cluster[12]. Two-dimensional perovskites exhibit one-dimensional periodicity (the perovskites exist as two-dimensional sheets, hence their name), and are sandwiched with organic spacer layers. They contain periodicity similar to that seen in

superlattices or other two-dimensional materials like graphene, except with typically thicker layer spacing.[13]

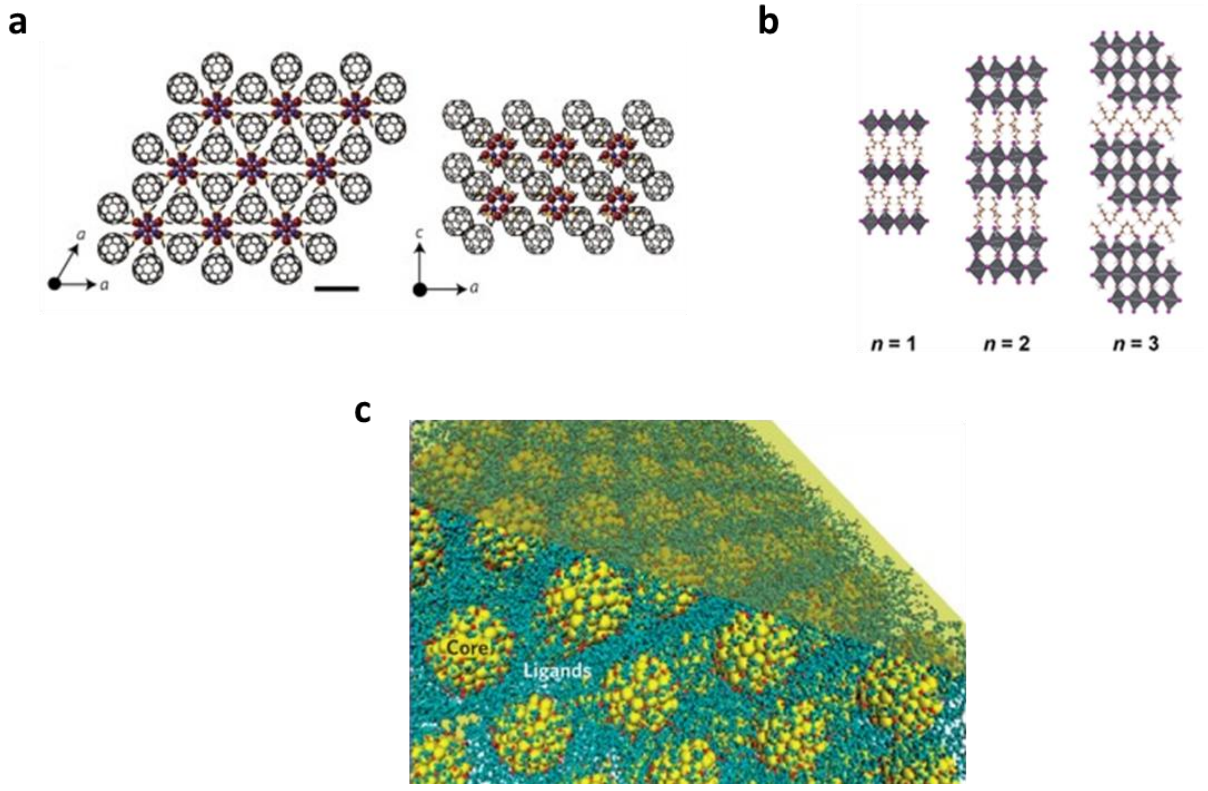

Figure 1.4. a) a schematic of a superatomic lattice of $[Co_6Te_8][C_{60}]_2$ from both a top-down and cross-sectional view[14], b) a cross-sectional view of a $BA_2MA_{n-1}Pb_nI_{3n+1}$ two-dimensional perovskite, where *n* represents the thickness of the perovskite layer[15], c) a cartoon of an array of nanocrystal cores connected by ligands extending from each core[16].

An understanding of thermal transport in these materials is necessary due to their growing popularity and their attractiveness in optoelectronic, photovoltaic, and thermoelectric devices. We therefore sought to undergo multifaceted experimental research to elucidate their thermal

conductivity and the underlying phonon behavior that controls phase change, order-to-disorder, and coherence dependencies.

1.4 Methodology – Frequency Domain Thermoreflectance

Our primary interest is to understand heat transfer and thermal conductivity in these novel materials. To do this, we employ an experimental technique known as frequency-domain thermoreflectance, or FDTR. This tool will be referred to repeatedly throughout the text, so a detailed description of its fundamental operation and daily use is necessary.

We use FDTR as opposed to the other techniques that exist to measure thermal conductivity for several reasons, the first of which being that it can be used to measure materials with ultrahigh[17] and ultralow thermal conductivity[6], and anything in between. Moreover, FDTR is a non-contact optical pump-probe technique, so unlike 3ω or transient hotwire it is completely non-destructive and does not require complex sample preparation. The technique can be used to interrogate samples kept at any temperature and in any transparent medium and can be used while samples are kept in vacuum with no additional challenge. Finally, and perhaps most importantly, FDTR, as well as time-domain thermoreflectance (TDTR), is highly sensitive to thermal conductivity in materials (high and low k) and samples (ultrathin, small lateral dimension) that conventional techniques typically are not[14,18].

In FDTR, a continuous-wave (CW) 488 nm laser is passed through an electro-optic modulator (EOM) to create a sinusoidal intensity modulation at a frequency set by a signal generator. This laser, called the pump laser, is directed at and focused on the sample to serve as a circular heat source. The periodicity of the heating causes the temperature of the nearby vicinity

to modulate at the same frequency but at a slight delay due to the sample's limited thermal responsivity at high frequencies. This induces a periodic variability in the reflectance of the sample (hence thermoreflectance), which is observed by a CW 532 nm 'probe' laser. The phase delay between the reflected pump and probe beams are collected by a photodetector which is locked into the same frequency as set by the signal generator, as shown in Fig. 1.5.

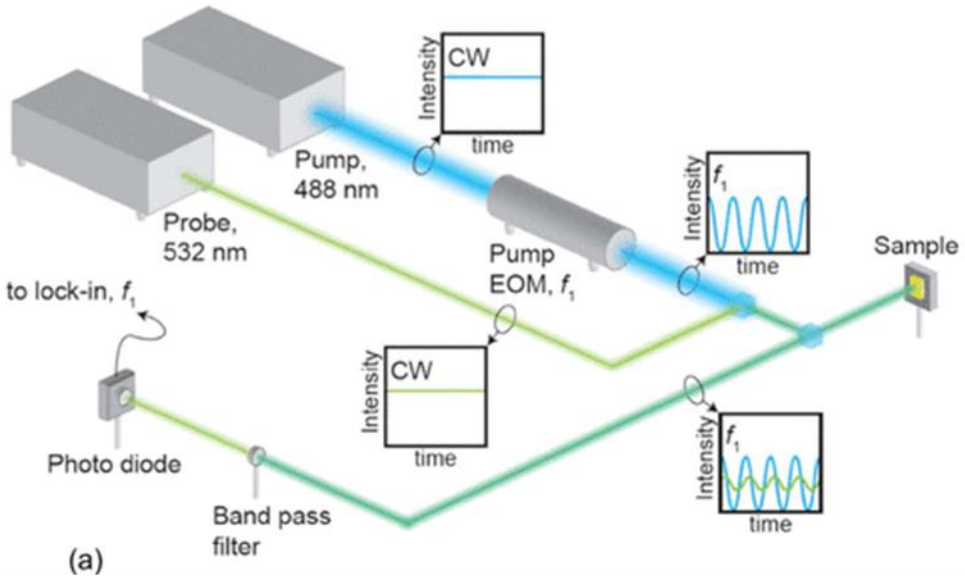

Figure 1.5. FDTR is represented in the schematic. The pump and probe lasers are directed at the sample and are both reflected towards a photodiode. The EOM and photodiode are set at the same frequency so that only signal generated by the thermoreflectance is captured in the measurement[19].

The phase information, an example of which is shown in Fig. 1.6, is fit to a model solution of the heat diffusion equation that relies on thermophysical inputs to determine the sample's thermal conductivity.

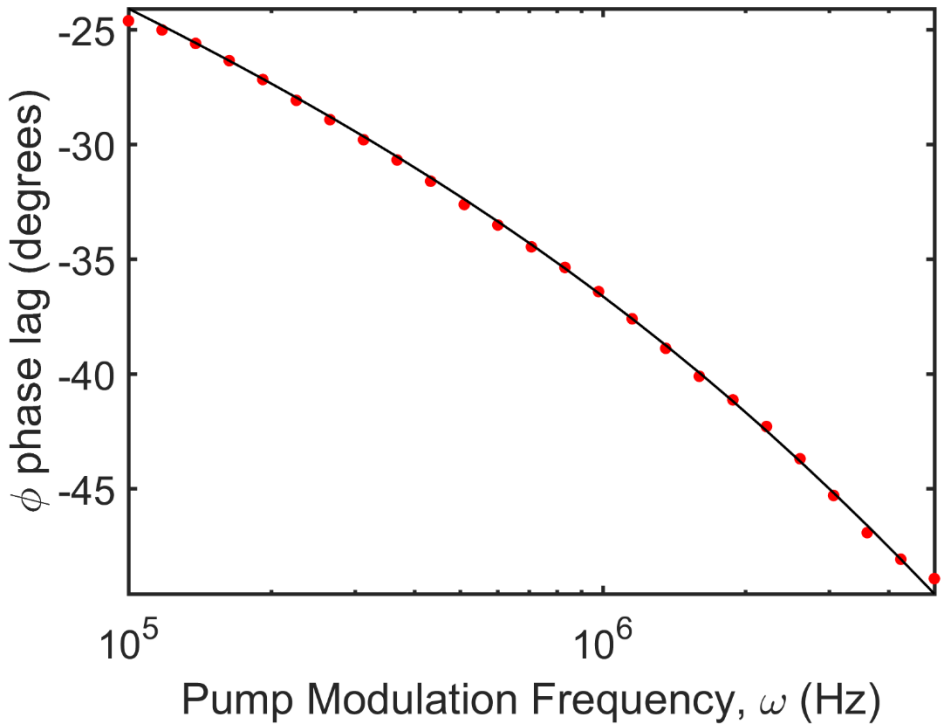

Figure 1.6. The data acquired from FDTR (red) is fit to the MSE-minimizing solution of the heat diffusion equation to determine the sample's thermal conductivity. In this example, the measurement was acquired at 25 points spaced logarithmically between 100 kHz and 5 MHz.

The sample thermal conductivity is evaluated numerically from the following expression which describes the range of sample temperature resulting from pump heating:

$$\Delta T_{AC} = 2\pi A \int_0^\infty G(\Lambda) \exp\left(-\pi^2 \Lambda^2 \frac{w_0^2 + w_1^2}{2}\right) \Lambda d\Lambda \qquad 1.4.1$$

Here, A represents the amplitude of the heat source, $G(\Lambda)$ is the Hankel transform of the radial heat source described by the pump laser where Λ is a transform variable, and $\frac{w_0^2+w_1^2}{2}$ is the square of the average laser spot size, where w_0 and w_1 represent the radius of the pump and probe beams.

For a single layer, $G(\Lambda)$ is

$$G(\Lambda) = \frac{1}{k\left(4\pi^2\Lambda^2 + \frac{i\omega}{D}\right)^{1/2}} \tag{1.4.2}$$

where k is the thermal conductivity, ω is the modulation frequency, and D is thermal diffusivity. This solution can be generalized for a multi-layered sample through an iterative approach. This is critically important for our work as samples are typically coated with a metal transducer, or signal amplifying layer, to improve the signal to noise ratio of our measurement. In Eq. 1.4.3, *n* represents the layer of the sample, where *n* = 1 represents the topmost layer.

$$\begin{pmatrix} B^+ \\ B^- \end{pmatrix}_n = \frac{1}{2\gamma_n}\begin{bmatrix} \exp(-u_n L_n) & 0 \\ 0 & \exp(u_n L_n) \end{bmatrix} \times \begin{pmatrix} \gamma_n + \gamma_{n+1} & \gamma_n - \gamma_{n+1} \\ \gamma_n - \gamma_{n+1} & \gamma_n + \gamma_{n+1} \end{pmatrix} \begin{pmatrix} B^+ \\ B^- \end{pmatrix}_{n+1} \tag{1.4.3}$$

Since the sample is assumed to be infinite in the thickness direction, the value of B^+ and B^- of the bottom layer are 0 and 1, respectively. Here,

$$u_n = \left(4\pi^2\Lambda^2 + \frac{i\omega}{D_n}\right)^{1/2} \tag{1.4.4}$$

$$\gamma_n = k_n u_n \tag{1.4.5}$$

Finally, $G(\Lambda)$ is expressed as

$$G(\Lambda) = \left(\frac{B_1^+ + B_1^-}{B_1^- - B_1^+}\right)\frac{1}{\gamma_1} \qquad 1.4.6$$

This expression can be put back into Eq. 1.4.1 to predict the pump-induced temperature modulation (ΔT, which turns out to be a complex number) at which point the thermal conductivity can be iteratively fit to the solution by finding the value for k that creates a predicted phase delay that most closely matches the experimental data.[20] The phase delay is calculated from ΔT_{AC} as

$$\theta_{lag} = \tan^{-1}\frac{\Delta T_{AC,imaginary}}{\Delta T_{AC,real}} \qquad 1.4.7$$

The fully-developed solution combining Eq. 1.4.1 with Eq. 1.4.6 can be applied to predict the temperature of the local region of the sample subjected to laser heating. This is done by summing the DC and AC contributions from the relevant lasers:

$$\Delta T_{tot} = \Delta T_{DC,pump} + \Delta T_{AC,pump} + \Delta T_{DC,probe} \qquad 1.4.8$$

Since the probe is unmodulated, heating is not frequency dependent. Fig. 1.6 shows the sample thickness dependance of localized temperature rise. The samples measured using FDTR often have low thermal conductivities and diffusivities and are therefore heated well beyond room temperature if sufficiently thick. This poses a considerable challenge when measuring single-crystal samples, as we will see in subsequent sections.

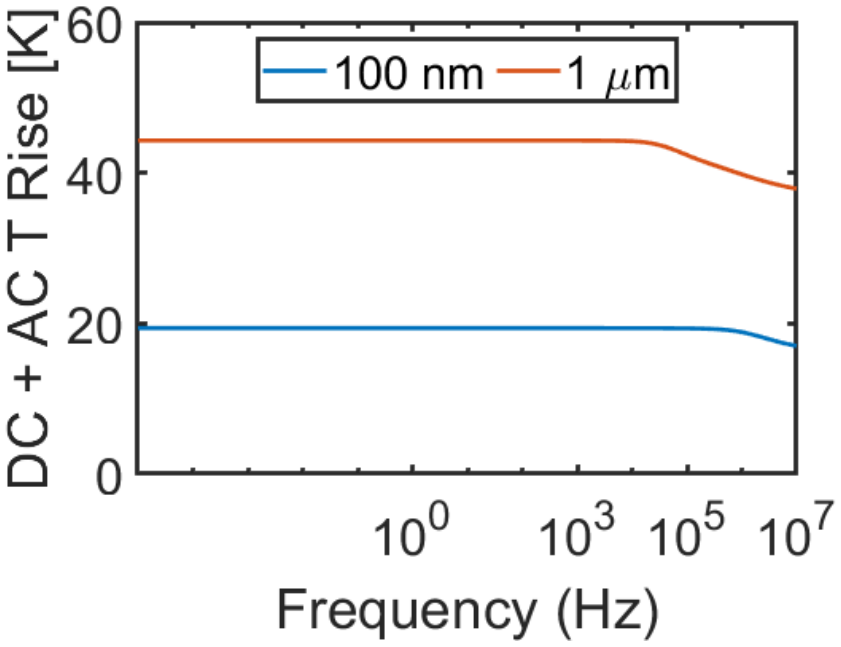

Figure 1.7. Localized temperature rise is a result of steady-state, or DC heating as well as the component of heating from the pump that is periodic. The effects of modulation only become visibly present when the EOM frequency is sufficiently larger than the thermal response time of the material.

It is important to assess the sensitivity of the model to the parameters which it invokes in order to gauge the model's, and by association the measurement's, sensitivity to the sample's thermal conductivity. The sensitivity to a specific parameter β is

$$S_\beta = \frac{\beta \partial \varphi}{\varphi \partial \beta} = \frac{\partial \ln(\varphi)}{\partial \ln(\beta)} \approx \frac{\Delta \ln(\varphi)}{\Delta \ln(\beta)} = \frac{\ln\left(\varphi_{\beta_{adj}}\right) - \ln(\varphi_\beta)}{\ln(\beta_{adj}) - \ln(\beta)} \qquad 1.4.9$$

where the term β/φ is introduced to normalize the sensitivity parameter[21]. This definition of sensitivity is standard and has been used in a plethora of both TDTR and FDTR analyses (φ is replaced by $-V_{in}/V_{out}$ in TDTR)[7,22–25].

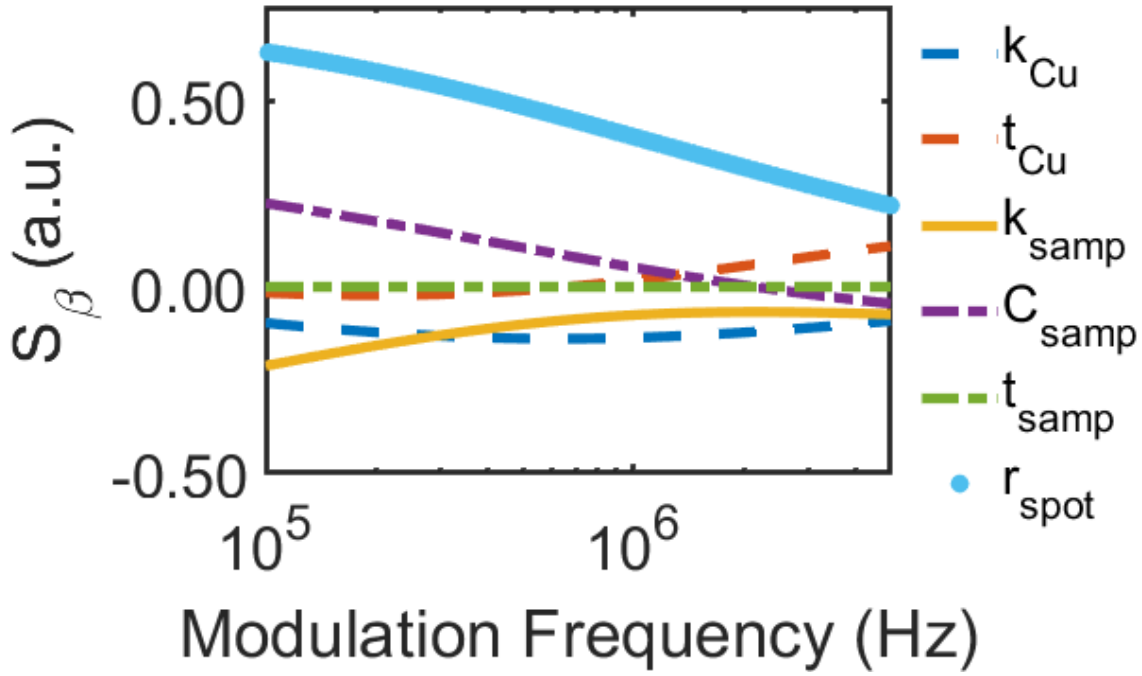

Figure 1.8. Model sensitivity to parameters β. The model is typically very sensitive to laser spot size, and metal transducer thermal conductivity. Uncertainties that result from negative and positive sensitivities can potentially nullify one another, so the resulting uncertainty in thermal conductivity is not simply the aggregate of the sensitivities at that modulation frequency.

The sensitivity for a simple sample comprised of 60 nm of Cu on top of a 10 μm thick investigative material resting on a SiO_2 wafer is shown in Fig. 1.8. As the figure suggests, the model is overwhelmingly sensitive to the laser spot size compared to any other parameter. This is not necessarily concerning, however, since the spot size is well understood and is not expected to vary significantly to introduce error in the fit of thermal conductivity. Moreover, uncertainty

resulting from this sensitivity can be managed using mathematical techniques[26]. Fortuitously, parameters that are unknown at the time of measurement, such as sample heat capacity (denoted by C_{samp}) do not significantly affect the model and are unlikely to diminish the quality of fit.

2 Superatomic Structures

2.1 Background and Introduction

Precision and tunability of material composition, and the associated effects on functional properties, are critical to the development of modern technology. Generally, compositional tunability of conventional crystalline solids is limited by the number of thermodynamically stable compounds that can be created from elements and polyatomic molecules. The creation of hierarchical materials from these basic building blocks, which can then serve as the basis for highly tunable nanocomposites is therefore an attractive concept. One such class of material is the nanocrystal solid, which exhibits exciting optoelectronic properties. These materials, however, are typically polydisperse and often do not have the atomic precision needed to gain insight on key relationships between crystal structure and resulting energy transport, storage, and conversion characteristics[27–29].

Thermodynamically stable atomically precise clusters, or intermediately sized groups of atoms, that exhibit collective behavior are termed ‘superatoms.’ They gained this term for their tendency for collective behavior, much like one might expect from a singular large, or super, atom. There are many types of superatoms, the most notable of which include metal-chalcogenides and fullerenes stabilized with capping ligands that encourage self-assembly and cluster organization. The long-range assembly of such superatoms are commonly referred to as superatomic crystals, or SACs. Efforts to study, develop, and utilize superatomic crystals has culminated in a vast library of materials with a wide variety of functional properties such as redox activity, large magnetic moment, and luminescence[12].

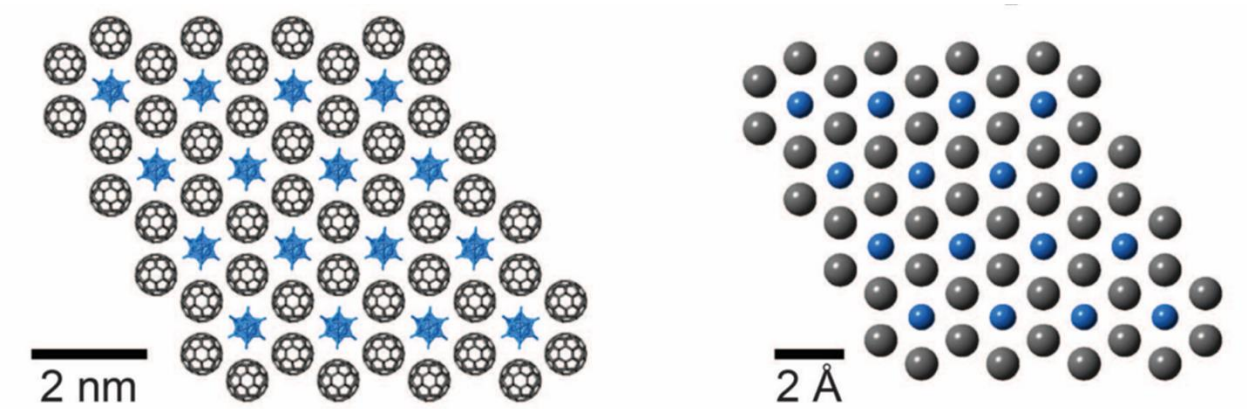

Figure 2.1. The cross-sectional image of a metal chalcogenide – fullerene SAC (left) is shown against CdI_2 to illustrate the similarities between superatoms and their elemental counterparts[30]. While visually similar, superatoms differ from nanocrystals in their atomic precision and slightly reduced size.

2.1.1 Thermal Transport in Superatomic Crystals

Heat transport in SACs and other crystalline dielectrics is mediated primarily by phonons. However, the main mechanisms by which heat is transferred from cluster to cluster or across ligands was largely unknown until only a few years ago. Nanocrystal arrays exhibit a high degree of phonon scattering across organic-inorganic interfaces and are thus described well by effective medium approximations (EMAs)[16,31,32]. SACs, however, are built from smaller clusters that are not large enough to exhibit bulk-like transport properties, therefore requiring different treatment. Ong *et al*. used FDTR to measure the thermal conductivity of both unary and binary SACs composed of metal chalcogenides $Co_6S_8(PEt_3)_6$, $Co_6Se_8(PEt_3)_6$, $Co_6Te_8(PEt_3)_6$, and the fullerene C_{60}[14].

Ong *et al*. found that SAC room temperature thermal conductivity is linearly proportional to the average sound speed of phonons, consistent with the phonon gas model expressed in Eq. 1.1.11. Moreover, they suggested that the temperature-dependency of thermal conductivity of $Co_6Se_8(PEt_3)_6(C_{60})_2$ at low temperatures is representative of a crystalline material. They reason that at low temperatures the fullerenes are locked in place, but that they become orientationally disordered at temperatures above 190 K and scatter phonons, initiating an amorphous-like heat transfer regime. This phenomenon is not seen in $Co_6Te_8(PEt_3)_6(C_{60})_2$ due to the considerably larger chalcogenide superatom size which inhibits short-range anisotropic interactions that induce fullerene rotation[33,34].

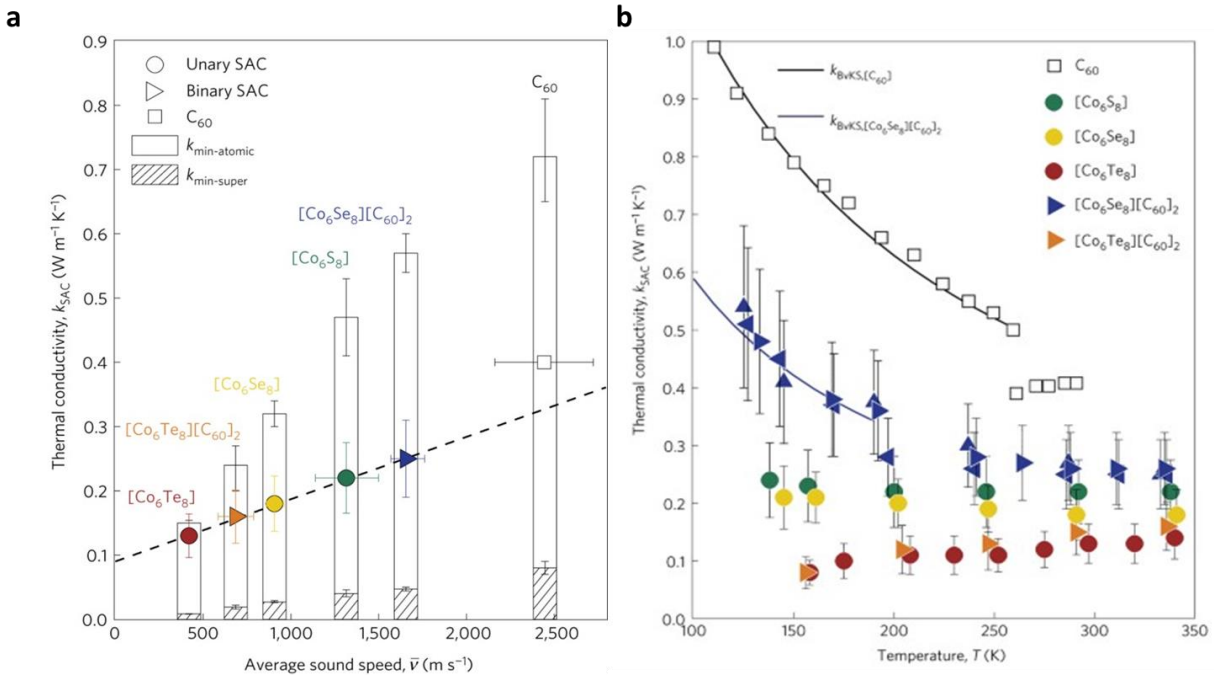

Figure 2.2. a) SAC thermal conductivities are plotted against the average phonon sound speed within each structure to highlight to linear dependence and conformity to the standard phonon gas model, b) most SACs have amorphous-like thermal conductivities (temperature independent),

however $[Co_6Se_8][C_{60}]_2$ experiences an order-to-disorder transition around 190 K which allows the fullerenes to rotate freely and scatter phonons, thereby catalyzing an amorphous-like regime[14].

2.2 $[Co_6Te_8(PEt_3)_6][C_{70}]_2$ Superatomic Crystals

The order-to-disorder transition and consequent effects on thermal transport behavior in $Co_6Se_8(PEt_3)_6(C_{60})_2$ naturally raised the question of whether similar phenomena could be observed in other SAC materials, and if so, what functionalities or tunable properties might arise. In this study, we considered a novel superatomic crystal created by our collaborators at Columbia University, $[Co_6Te_8(PEt_3)_6][C_{70}]_2$, due to the complementary size of the metal and fullerene cluster[35]. C_{70} is larger and more oblong than C_{60} and is similar in shape to a rugby ball. We therefore hypothesized that this structure posed a larger probability of exhibiting orientational disorder, particularly along the long axis, as opposed to a structure that paired C_{70} with a Se-based metal cluster.

Unlike the binary SACs studied by Ong *et al*., this structure, which will be referred to as $[CoTe][C_{70}]$ henceforth for brevity, exhibits two distinct thermally driven phase transitions. The three structural phases are identified using a technique known as single crystal X-ray diffraction, or SCXRD. This experiment subjects the sample to a beam of X-rays with wavelengths on the order of the crystal structure which are diffracted according to Bragg's law and collected as the sample is rotated. The X-ray count is collected at every orientation and fit computationally to determine the atomic structure of the compound[36].

An Agilent SuperNova diffractometer was used to collect SCXRD data at 100, 250, and 340 K. The low temperature phase, or Phase A, is distinguished by a combination of orientationally

ordered monomers (C_{70}^-) and dimers (C_{140}^{2-}), the latter of which consist of two C_{70}s chemically bound together along the long axis. The fullerenes become orientationally disordered in the intermediate phase, Phase B, and rotate about their axis of symmetry. The dimers finally dissociate at 340 K as they enter Phase C due to reversible homolytic cleavage that decouples their rotation and delocalizes electrons at the intersection of the two C_{70}s, resulting in nearly spherical electron densities surrounding the fullerenes.

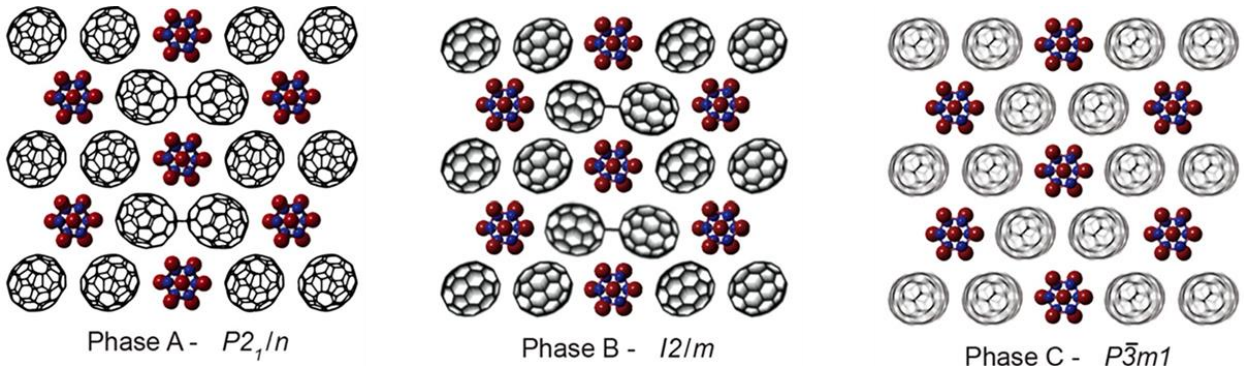

Figure 2.3. a) some C_{70}^-s form dimeric C_{140}^{2-} compounds at low temperatures, b) all fullerenes become able to rotate about their long axis in the intermediate temperature phase, c) dimers are separated *via* homolytic cleavage, making the full structure monomeric and enabling full orientational disorder and electronic delocalization[35].

Homolytic cleavage was identified as the separation mechanism in the fullerenes based on a previous report[37] and was characterized in the $[CoTe][C_{70}]_2$ structure using differential scanning calorimetry, or DSC. This thermoanalytical technique is commonly used to measure the location of phase changes by recording the temperature of the sample as a function of the heat flow, thereby enabling calculation of the heat capacity of the material. The heat capacity of $[CoTe][C_{70}]_2$ was measured using a TA Instruments Q20 Differential Scanning Calorimeter and is shown in Fig. 2.4.

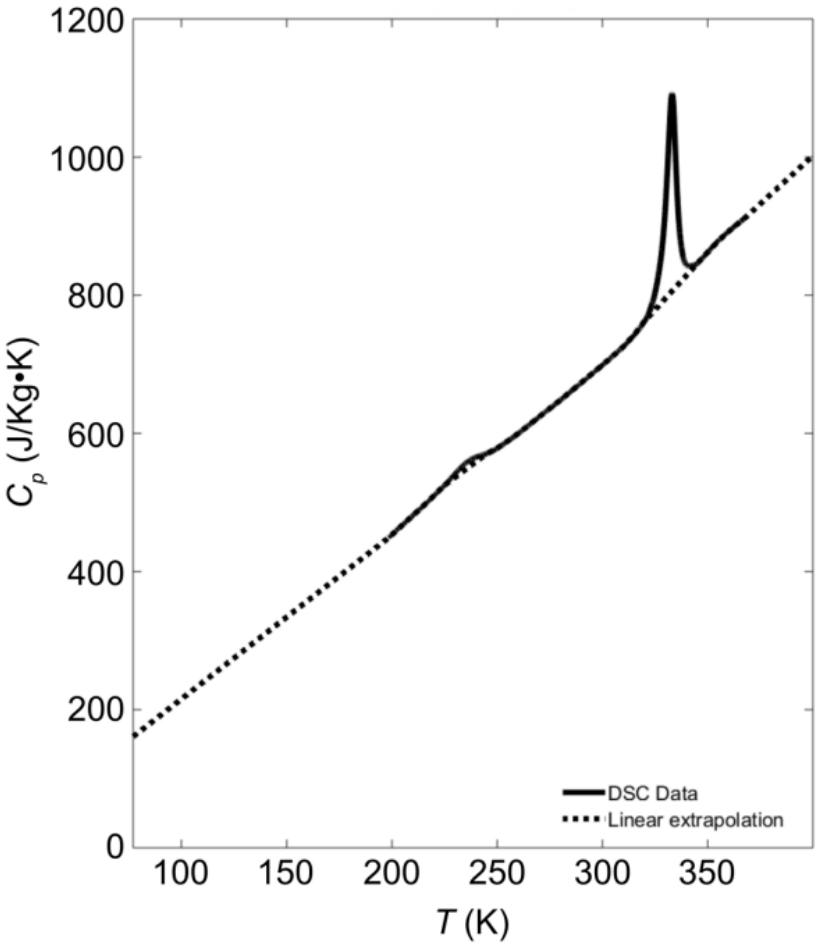

Figure 2.4. Heat capacity of $[Co_6Te_8(PEt_3)_6][C_{70}]_2$ as a function of temperature. A linear interpolation and extrapolation is performed to compensate for effects of phase change on the measurement and to provide an estimation of low temperature heat capacity.

Samples between 8 and 15 mg were loaded into non-hermetic aluminum pans and run between 200 and 370 K at a rate of 10-20 K/min with an isothermal interval of 5 minutes between cycles. The phase change from Phase A to Phase B is minor in terms of formation enthalpy compared to the high temperature phase change, consistent with the idea that additional energy is needed to cleave the bond joining neighboring C_{70}s. Moreover, optical gap energy data shown in Fig. 2.5a

reveal the emergence of a low energy gap at this phase change, greatly increasing the material's electrical conductivity (σ) by two orders of magnitude (shown in Fig. 2.5b) and increasing lattice spin density and therefore the molar magnetic susceptibility (shown in Fig. 2.5c).

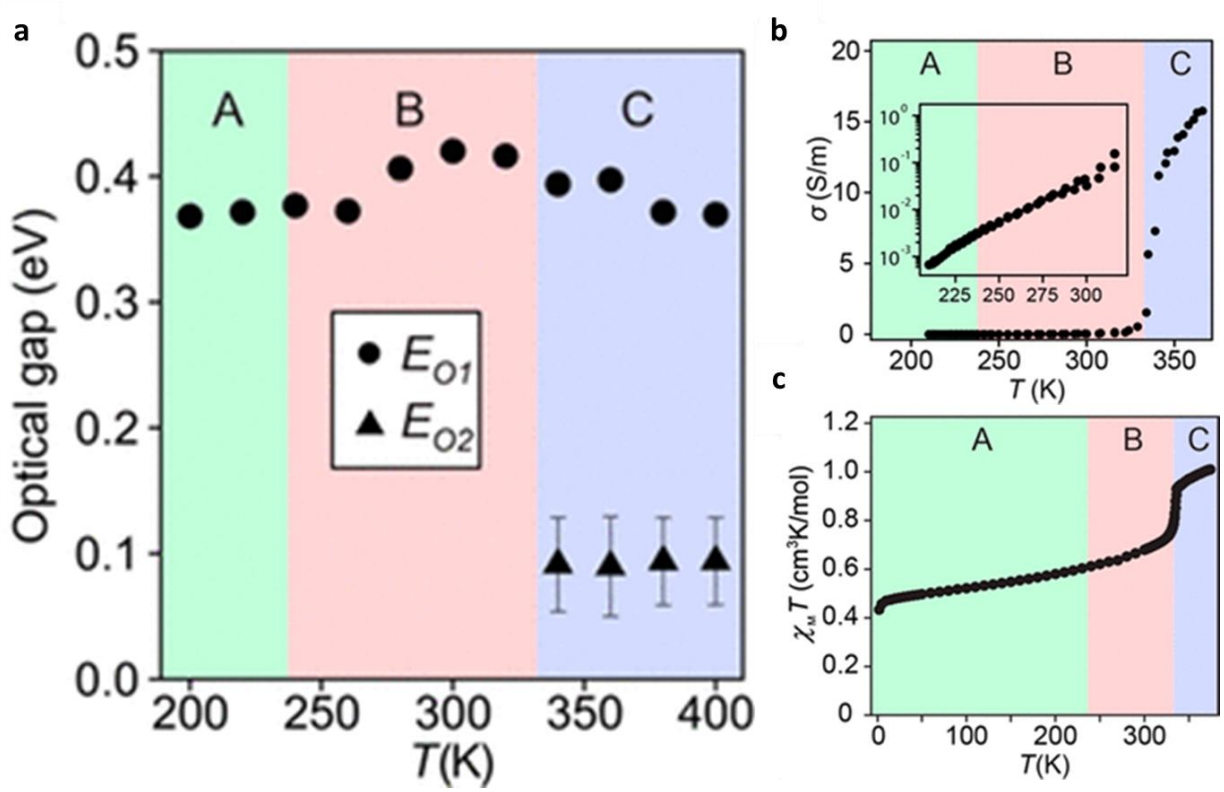

Figure 2.5. a) optical gap energy, obtained from the absorption spectra, reveals a new gap in phase C, which is responsible for increased free electron density and thus b) increased electrical conductivity and c) higher molar magnetic susceptibility in that phase.

The effects of homolytic cleavage on electrical and optical properties appear to be completely relegated to the high temperature phase transition. However, thermal conductivity is comparatively more affected by the low temperature phase transition. We collected thermal conductivity data using frequency-domain thermoreflectance, or FDTR, which is shown in Fig.

2.6. Data was acquired at a wide range of temperatures by placing samples in an Oxford Instruments Microstat He. The chamber was evacuated to pressures below 10^{-5} Torr using a Pfeiffer HiCube 80 Eco and the mounting platform was cooled using liquid nitrogen.

For this experiment, we adhered single crystals of thickness less than 100 μm on SiO_2 wafers using a non-degassing epoxy developed by 3M. The assemblies were then placed in a Perkin Elmer 6J sputtering system and coated with a transducer layer of 60-100 nm of Au. The thickness of the Au was confirmed using an X-ray reflection technique on the X'Pert Pro MRD X-Ray Diffractometer. The Au thermal conductivity was obtained *via* four-point probe resistivity measurements using a Lucas-Signatone Corp 302 Resistivity Stand in conjunction with the Weidemann-Franz law, shown in Eq. 2.2.1.

$$k = \sigma L T \qquad 2.2.1$$

Here, σ represents electrical conductivity, T represents absolute temperature and L represents the Lorenz number which is typically equal to or near $2.44 \times 10^{-8}\ \mathrm{W\Omega K^{-2}}$. This relation is a useful and often accurate approximation of thermal conductivity of materials in which the heat carriers are predominantly electrons. Bulk values of k_{Au} are not reliable for films of such thickness due to the boundary scattering events that limit the cross-layer propagation of low-frequency or long mean free path states of heat carriers (primarily electrons).

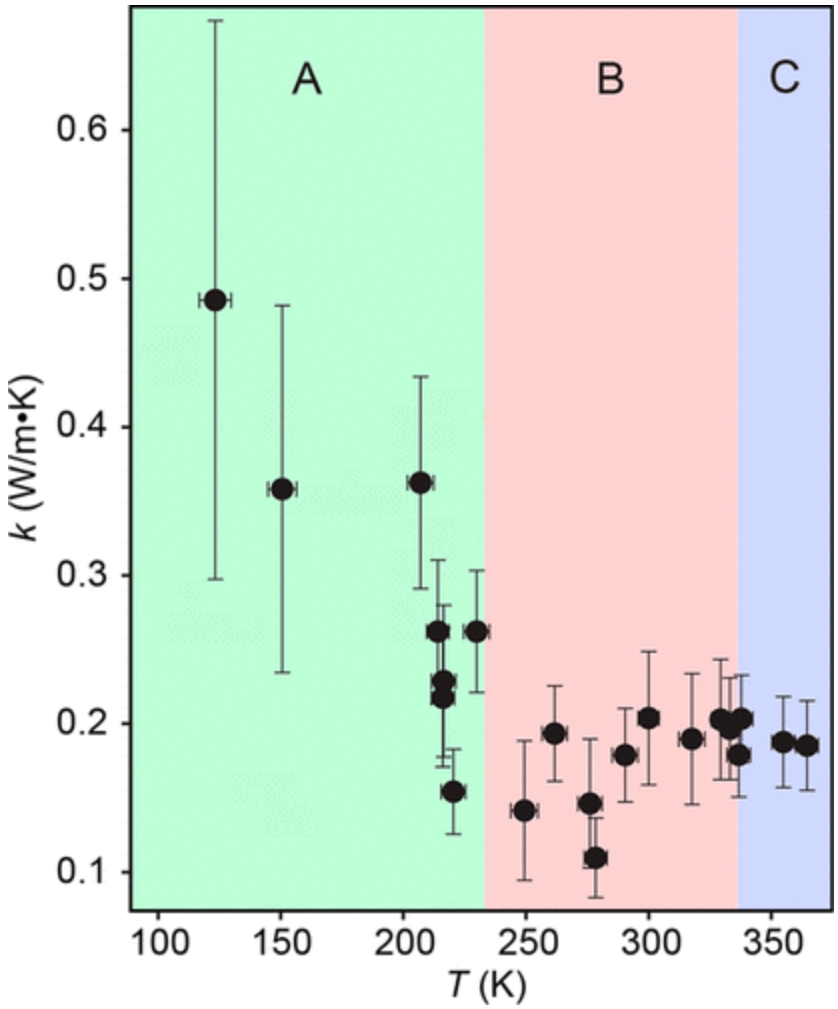

Figure 2.6. Thermal conductivity data from ~100 – 360 K, where each structural phase is distinguished by background color. A strong temperature-dependence is observed in the low temperature phase but disappears in Phases B and C.

Thermal conductivity data is shown in Fig. 2.6, where nominal temperatures were calculated using an iterative approach where heating is modeled using the theory established in section 1.4 and the sample's absorbed thermal energy, which was measured using a Thorlabs PM100D Digital Optical Power Meter, to determine the sample's thermophysical properties at that temperature. The error bars represent uncertainty for a cluster of measurements which were

deemed acceptable ($\pm$ 0.45 μm from the measured spot size and error, quantified as a mean squared error (MSE) no greater than 1.2 times the global minimum). The average thermal conductivities and temperatures (denoted generally in Eq. 2.2.2 as x) of the cluster of measurements were calculated as

$$\bar{x} = \frac{1}{N}\sum_{i=1}^{N} x_i \qquad 2.2.2$$

where N represents the number of measurements within the cluster. The total uncertainty of the cluster, u, was calculated based on a formulation derived in previous work[32,38]:

$$u = \left\{\left[\frac{1}{N}\sum_{i=1}^{N}(u_i^2 + x_i^2)\right] - \bar{x}^2\right\} \qquad 2.2.2$$

k decreases strongly with temperature in Phase A, following the typical behavior of a crystalline material and plummeting from $0.49 \pm 0.19\ \mathrm{Wm^{-1}K^{-1}}$ to approximately $0.16 \pm 0.08\ \mathrm{Wm^{-1}K^{-1}}$. This is attributed to the activation of phonon modes that begin to scatter with one another, reducing the average phonon mean free path and therefore thermal conductivity. However, the temperature dependence is no longer present in phases B and C due to the orientational disorder of the fullerenes which create incoherent vibrations that scatter lattice phonons and induce an amorphous transport regime. Because electrons contribute very little to thermal conductivity in this material (less than ~$10^{-4}\ \mathrm{Wm^{-1}K^{-1}}$), the effects of increased σ are not evident in the thermal conductivity across the high temperature phase transition.

These results confirm our initial hypothesis that orientational disorder could exist in materials beyond those discussed by Ong *et al.*[14]. In this work we found that the SAC $[Co_6Te_8(PEt_3)_6][C_{70}]_2$ exhibits three distinct structural phases. The low temperature phase transition is distinguished by C_{70} rotation that scatters phonons and causes thermal behavior to switch from that akin to a crystalline material to that of an amorphous one. The high temperature phase transition is marked by the homolytic cleavage of the C_{140}^{2-} dimer into two C_{70}^{-}s which creates a low energy optical gap. The increased free electron density greatly increases electrical conductivity, and an increased spin density increases molar magnetic susceptibility. This study demonstrates the expansiveness of property tunability, reversibility, and engineering in SACs.

2.2.1 Statement of Contribution

Alexander D. Christodoulides, Matthew Bartnof, Alan J.H. McGaughey, and Jonathan A. Malen: Metal deposition and other sample preparation for thermal conductivity measurements, FDTR measurement of thermal conductivity and related analysis.

Evan S. O'Brien, Jake C. Russell, Kihong Lee, Jordan A. DeGayner, Daniel W. Paley, X.-Y. Zhu, and Xavier Roy: Sample synthesis, SCXRD, DSC, electrical, optical, and magnetic measurements and related analysis.

2.3 $[Co_6Te_8(PPr_3)_6][PBCM]_n$ Amorphous Thin Films

The previous study exhibits SACs with highly reversible and functionalized phase transitions through careful selection of the constituent superatoms ([CoTe] and $[C_{70}]$) that self-

assemble due to size and mass pairing. However, it is also possible to frustrate electrostatic interactions using larger clusters that inhibit ionic cluster pairs and therefore overall crystallization. This type of structure, no longer a superatomic crystal but rather an amorphous superatomic thin film, shows similar levels of tunability to SACs due to their shared solution processability but with enhanced properties that make it attractive for thermoelectric applications.

Our collaborators at Columbia University prepared fully amorphous superatomic thin films containing large clusters, $Co_6Te_8(PPr_3)_6$ (or simply [Co]) and $C_{72}H_{14}O_2$ (or PCBM) in order to disperse electric charge over large volumes thereby weakening local electrostatic interactions. This is made possible by the inclusion of tri-*n*-propylphosphine as the metal-core ligand as opposed to the triethylphosphine (PEt_3) used in previous studies[14,35]. The increased flexibility of these chains greatly reduces the strength of electrostatic interactions that bind superatoms together, enabling fully amorphous structures. In this study we examined the properties emergent from compositional tunability in this compound by through variation of the molar ratio of PCBM to $Co_6Te_8(PPr_3)_6$ (2:1, 3:1, 4:1, 5:1, 7:1, and 9:1). This ratio will henceforth be represented by *n*, being that it is always an integer value.

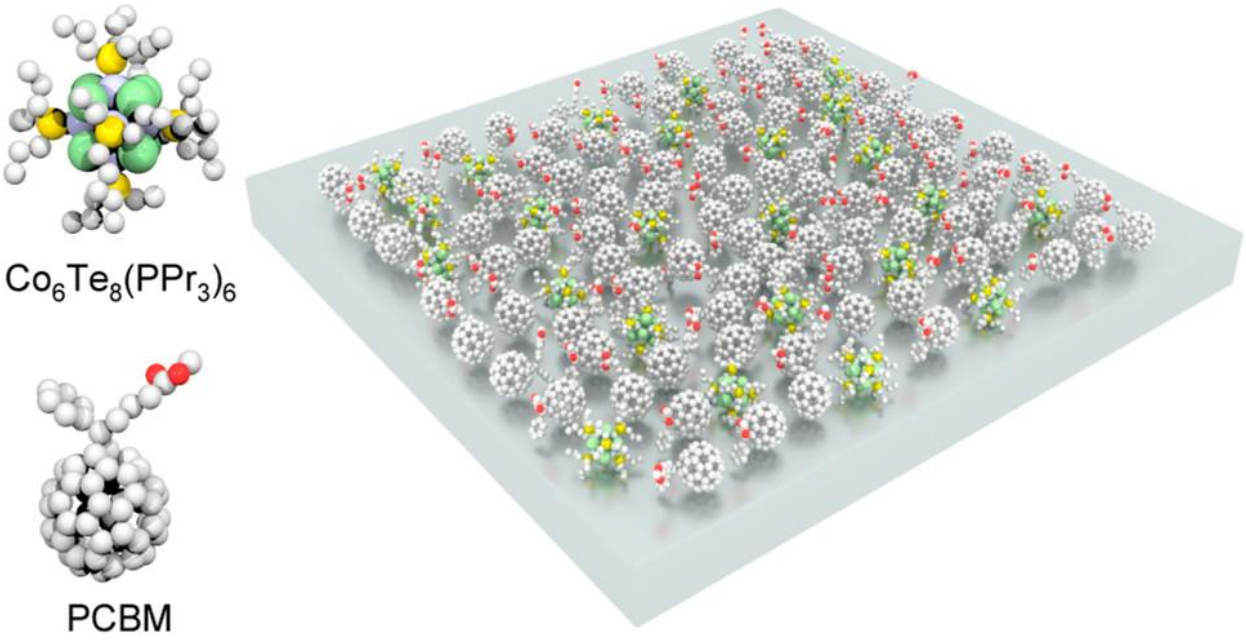

Figure 2.7. A schematic of a $[Co_6Te_8(PPr_3)_6][PCBM]_n$ superatomic thin film is shown, where the orientation of both clusters appears random as would be expected in an amorphous structure.

Superatomic thin films, such as the one depicted in Fig. 2.7, were spin-coated on silicon substrates and structurally characterized using scanning electron microscopy (SEM) and energy dispersive X-ray spectroscopy (EDS) to ensure uniformity and homogeneity. In SEM, the sample is bombarded by an electron gun with primary electrons which generates secondary electrons which are collected as the gun rasters to generate a high-magnification image. EDS, by comparison, relies on the interaction of the sample with X-rays to emit atomically characteristic electromagnetic waves. Sample thicknesses were gauged using atomic force microscopy, or AFM, which measures vertical movement of a probe tip as it moves across the sample based on the deflection of a laser that is reflected off the probe. This type of microscopy has extreme precision and is capable of characterizing the topography of nanometer scale thin films, such as the ones that were used in this study (~100 nm).

Electrical conductivity (σ) of each compound was measured at room temperature using a two-point resistivity approach on the Agilent 4155C semiconductor parameter analyzer in a N_2 glovebox enclosure. 40 nm of Au was deposited underneath the films to serve as source and drain electrodes. σ varies across all n from 19 to 301 S/m and appears to peak at n = 5, as shown in Fig. 2.8. Variable temperature electrical resistivity measurements reveal similar activation energies between n = 5 and n = 9 (87 vs 86 meV), suggesting that the higher conductivity seen in the n = 5 mixture is due to a higher ratio of $Co_6Te_8(PPr_3)_6$ which serves as the electron donating molecule. This mixture more optimally encourages free electron transport than n = 2 which was measured to have a significantly higher activation energy of 101 meV.

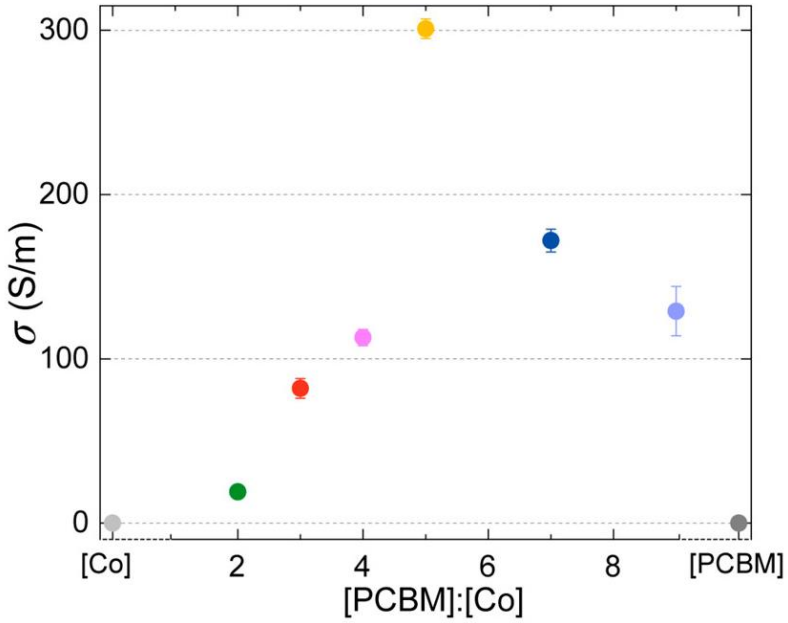

Figure 2.8. σ has a volcano-like relationship with molar composition. While [Co] and [PCBM] are both insulating materials in their pure form, molar mixtures of the two results in more electrically conductive thin films.

We used FDTR to measure the room temperature thermal conductivities (k) of these binary mixtures. Thermal conductivity data fitting requires knowledge of the mixtures' densities and heat capacities, which were unknown. We therefore defined the mixture density as

$$\rho_{[Co][PCBM]n} = \frac{M_{[Co][PCBM]_n}}{V_{[Co][PCBM]_n}} \qquad 2.3.1$$

where $M_{[X]}$ represents the molar mass and $V_{[X]}$ represents the molar volume of the mixture. This expression was then modified in terms of the properties of the mixture constituents:

$$\rho_{[Co][PCBM]n} = \frac{M_{[Co]} + M_{[PCBM]_n}}{V_{[Co]} + V_{[PCBM]_n}} = \frac{M_{[Co]} + nM_{[PCBM]}}{M_{[Co]}/\rho_{[Co]} + nM_{[PCBM]}/\rho_{[PCBM]}} \qquad 2.3.2$$

where $\rho_{[Co]}$ and $\rho_{[PCBM]}$ were determined previously[39,40], and molar mass was calculated as the summation of the molar mass of the constituents. Finally, we represented the specific heat as a function of the constituent heat capacity, density, and molar mass.

$$c_{[Co][PCBM]n} = \frac{\frac{C_{[Co]}M_{[Co]}}{\rho_{[Co]}} + \frac{nC_{[PCBM]}M_{[PCBM]}}{\rho_{[PCBM]}}}{M_{[Co]} + nM_{[PCBM]}} \qquad 2.3.3$$

Here, $c_{[X]}$ represents the specific heat whereas $C_{[X]}$ represents the volumetric heat capacity. $C_{[PCBM]}$ was obtained from previous work[9] and $C_{[Co]}$ was measured using a DSC technique.

These calculations are not exact, so we managed the operation of FDTR to minimize sensitivity to mixture heat capacity and density. According to our sensitivity analysis, shown in Fig. 2.9 for [Co][PCBM]$_2$, sensitivity to $k_{[Co][PCBM]n}$ is largest for modulation frequencies of 100 kHz to 2 MHz, so data was constrained to this range. Additionally, thermal time constants of the films,

$$\tau_{[Co][PCBM]n} = \frac{t_{[Co][PCBM]n}^2}{\alpha_{[Co][PCBM]n}} \qquad 2.3.4$$

where t and α represent film thickness and thermal diffusivity, are small compared to $1/f$, indicating an approximately steady state temperature that is insensitive to heat capacity.

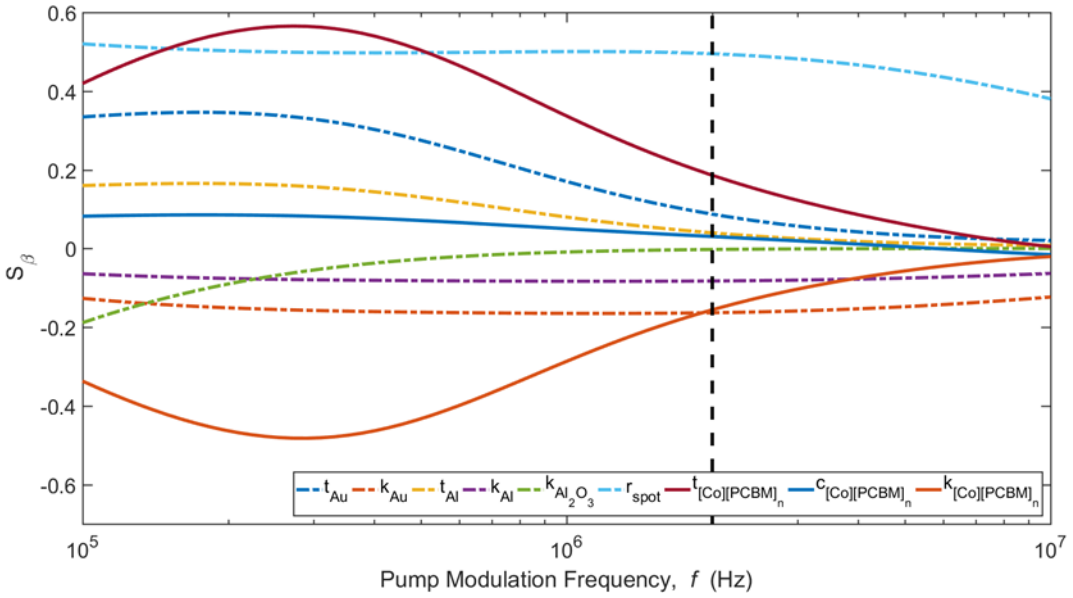

Figure 2.9. Normalized sensitivity of the model used to fit FDTR data is shown for modulation frequencies of 100 kHz to 10 MHz. FDTR data was only collected up to 2 MHz, represented by

the dashed vertical black line. The model is primarily sensitive to laser spot size, mixture thickness, and mixture thermal conductivity.

We find that all mixtures possess k of $0.05 - 0.07\ \mathrm{Wm^{-1}K^{-1}}$ with no observable dependency on molar ratio, as shown in Fig 2.10a. While $n = 5$ exhibits comparatively high σ, the Wiedemann-Franz law suggests that thermal conductivity is largely dictated by lattice contributions, k_l, and that electrical contributions, k_e, are less than 3% of the total value. The amorphous nature of all film compositions likely scatters almost all low-frequency vibrational modes that might exist in crystalline materials, leaving only high-frequency intermolecular modes to carry heat. This results in a consistently ultralow thermal conductivity nanocomposite that stands among the lowest ever recorded in fully dense materials[6], and well below that of its crystalline relatives ($0.16\ \mathrm{Wm^{-1}K^{-1}}$ of $[Co_6Te_8(PEt_3)_6][C_{60}]_2$ and $0.25\ \mathrm{Wm^{-1}K^{-1}}$ of $[Co_6Se_8(PEt_3)_6][C_{60}]_2$)[14].

The apparent decoupling of electrical and thermal conductivity behavior with *n* motivated us to explore the thermoelectric capabilities of these mixtures. A thermoelectric material is one that exhibits the creation of an electric potential due to a temperature gradient or vice versa. Such materials have shown great promise at extremely high temperatures but have struggled to achieve similar efficiencies at room temperature[41–44]. Thermoelectric performance is typically assessed using a figure of merit, ZT.

$$ZT = \frac{\sigma S^2 T}{k} \qquad 2.3.5$$

Here, S represents the Seebeck coefficient, which is the ratio of voltage to temperature gradient. The highest room-temperature ZT comes from bismuth chalcogenides Bi_2Te_3 and Bi_2Se_3 at around 0.8 – 1.0 [44]. By comparison, lead telluride compounds are capable of ZTs as high as 1.4 – 1.8 when subjected to temperatures more than 750 K[41–43]. While these values are promising, thermoelectric materials that may be used for solid-state cooling or parasitic heat recycling need to be capable of operating at lower temperatures that are typical of computer parts and other electronic devices.

Our collaborators measured the Seebeck coefficients of higher electrical conductivity mixtures (n = 5 and 9) and found them to be -129 and -169 μVK^{-1} respectively, resulting in ZT values of ~0.02 at room temperature for both compositions (shown in Fig. 2.10b).

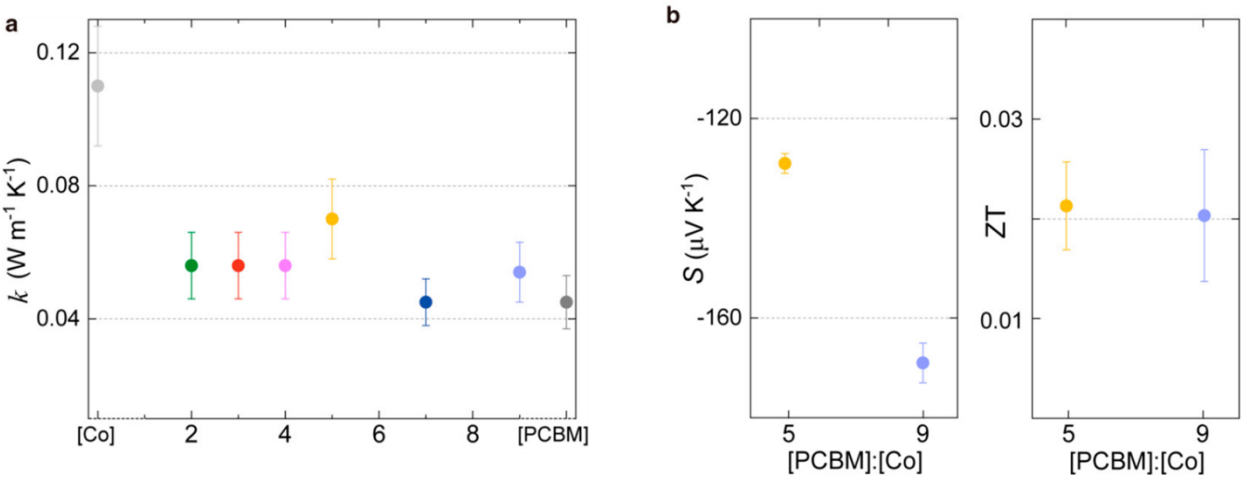

Figure 2.10. a) k measured using FDTR for [Co][PCBM]$_n$ mixtures of n = 2, 3, 4, 5, 7, and 9. Pure [Co] and [PCBM] were also measured, and the latter was comparable to that measured in previous reports[8,9], b) Seebeck coefficient measurements and ZT calculations for n = 5 and 9. The negative value of Seebeck coefficient indicates that the voltage at the low temperature terminal is higher, and that the potential gradient points opposite the temperature gradient.

While these mixtures may not be competitive with bismuth chalcogenides as thermoelectrics, they garner their own sphere of influence owing to their high compositional and consequent property tunability. Mixtures exhibit both high and low electrical conductivities while maintaining record low thermal conductivities as a result of their amorphous structure. The solution processability combined with the high degree of property flexibility opens pathways for the development of other multifunctional cluster solids.

2.3.1 Statement of Contribution

Alexander D. Christodoulides, Lingyun Dai, and Jonathan A. Malen: FDTR measurements of thermal conductivity and related analysis.

Jingjing Yang, Boyuan Zhang, Qinzhi Xu, Amirali Zangiabadi, Samuel R. Peurifoy, Christine K. McGinn, Elena Meirzadeh, Xavier Roy, Michael L. Steigerwald, Ioannis Kymissis, and Colin Nuckolls: material synthesis and sample preparation, SEM imaging, AFM characterization, TEM characterization, electrical conductivity, and thermoelectric measurements.

3 PbS Colloidal Nanocrystals

3.1 Background and Introduction

Colloidal nanocrystals (NCs) are clusters of inorganic particles several nanometers in diameter that are connected and stabilized by a matrix of ligand molecules connected to the nanocrystal surface. They are typically solution-grown, and they self-assemble into solid materials when deposited onto a substrate. The solid solutions, commonly termed NC solids, have found use in electronic[45–47], photovoltaic[48,49], thermoelectric[50], and optoelectronic[45–47,51] applications. While nanocrystals are unable to achieve the atomic precision of the superatomic structures discussed in the previous chapter, they exhibit superior monodispersity to materials used for similar applications such as molecular beam epitaxy-grown quantum dots[52]. This monodispersity results in enhanced property precision which, combined with convenient solution-processability and high tunability, makes NC solids attractive candidates in many facets of engineering design.

The thermal properties of NC solids are important for their successful implementation in functional devices. Prior research on thermal conductivity of NC solids shows that they have exceptionally low values of k of $0.1 - 0.4\ \mathrm{Wm^{-1}K^{-1}}$ [16,53,54]. These low thermal conductivities are useful in applications where large temperature gradients are needed, such as in thermal barrier coatings or thermoelectric devices. However, they may be problematic in applications where parasitic heat dissipation is needed, such as in electrical parts that generate significant amounts of thermal energy. Accordingly, a deep understanding and control of thermal transport in these materials is needed.

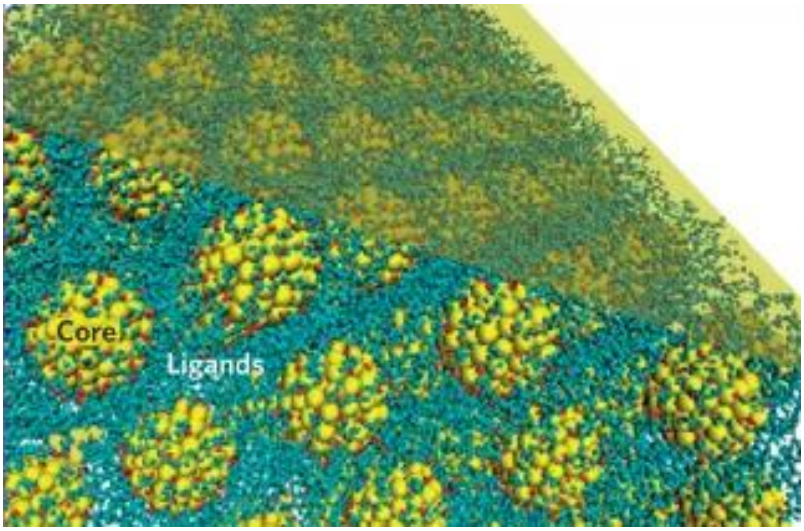

Figure 3.1. Inorganic nanocrystal cores are surrounded by a matrix of ligand molecules that stabilize the structure into a solid material when drop-cast or spin-coated on a substrate[16].

Prior work has identified different mechanisms that bottleneck thermal transport in NC solids. Ong *et al*. found that the bulk k of the NC core material has a minimal effect on the NC solid k, while core diameter is significantly more impactful[16]. This result suggests that the high thermal conductivity of different core materials is bottlenecked by core/ligand phonon mode mismatch, resulting in poor thermal communication. Liu *et al*. identify that the binding strength of the ligand end molecule is unimportant, but that backbone length is inversely correlated towards NC solid k *via* its effect on ligand volume fraction[54]. Finally, Wang *et al*. demonstrate that covalently crosslinking ligands greatly increases thermal conductivity in Fe_3O_4 NC solids by increasing the mean free path of acoustic phonon modes[53].

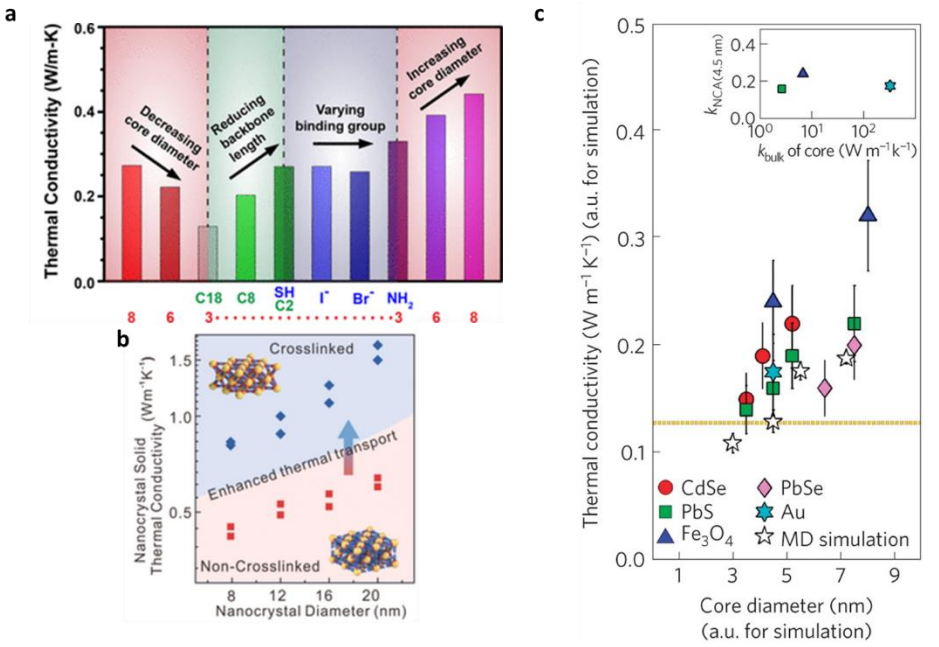

Figure 3.2. a) thermal transport in NC solids is not strongly affected by binding group but rather by ligand length and NC core diameter[54], b) crosslinking oleic acid ligands results in a four-fold increase in iron oxide NC solids[53], c) NC solid *k* is unaffected by changing core *k* by orders of magnitude[16].

3.2 PbS Nanocrystal Superlattices and Thin Films

Prior work has demonstrated that improved chain alignment of similarly bonded polymer chains results in increased thermal conductivity and strength[55,56], and that alignment of hydrocarbon chains in self-assembled monolayers (SAMs) enhances thermal conductances[32,57,58]. However, until now, the effects of ligand ordering and consequent core organization on thermal conductivity and elastic modulus in NC solids have been unexplored.

In this study, our collaborators at Arizona State University created single domain PbS NC superlattices (NCSLs) which exhibit excellent long-range order compared to conventional NC

solid thin films (NCFs). They produced such pristine samples by invoking slow diffusion of non-solvent (ethanol) into the NC solution. This was done by placing the NC/touluene solution at the bottom of a beaker, creating a buffer layer of proponal, and capping the heterogenous liquid mixture with ethanol. A silicon substrate was placed vertically within the tube, and diffusion of solvent into the NC solution, resulting in destabilization and NCSL crystallization, occurred within a 1 – 2-week period. The substrate was then carefully removed, rinsed with ethanol, and blow-dried with N_2.

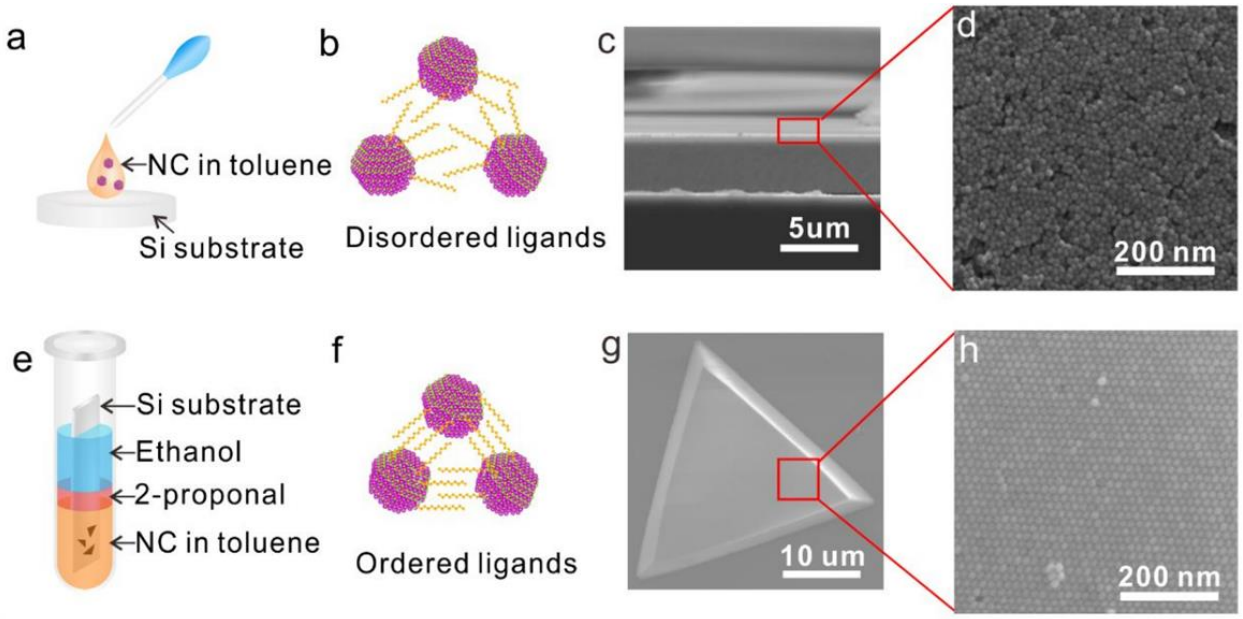

Figure 3.3. a) Typical NC solids were created by spin-coating NC solution on a substrate, b) the result of such preparation is an array of NC cores connected by disordered ligands, c) a cross-sectional SEM of the NC thin film; d) high-resolution SEM reveals disordered packing of PbS cores, e) NCSLs were prepared by slow diffusion of ethanol into NC solution, f) resulting in comparatively more ordered ligands; g) SEM image of an NCSL crystal, which typically takes a triangular or hexagonal form; h) high-resolution SEM shows ordered packing compared to NC thin films.

This synthesis technique was used to create monodisperse PbS NCSLs with core diameters of 3.0 – 6.1 nm with oleic acid ligands. A traditional method (shown in Fig. 3.3a) was also employed to create PbS NCFs as a basis of comparison. TEM imaging reveals average interparticle, or edge-to-edge, spacing of ~1.5 nm across all nanocrystals, and that NCFs present slightly higher core-core spacing. This is attributed to the fast-drying nature of the spin-coated solution which does not allow cores and ligands to order into a more thermodynamically favorable state. Such a phenomenon has been previously studied in PbS nanocrystals using small-angle-X-ray scattering (SAXS), which characterizes samples by detecting the scattering of slightly angled X-rays as they pass through a sample. Lee *et al*. report a 33% increase in interparticle spacing between three-dimensional crystals and films[59], and our collaborators therefore approximated the average interparticle spacing of NCSLs to be ~1.2 nm.

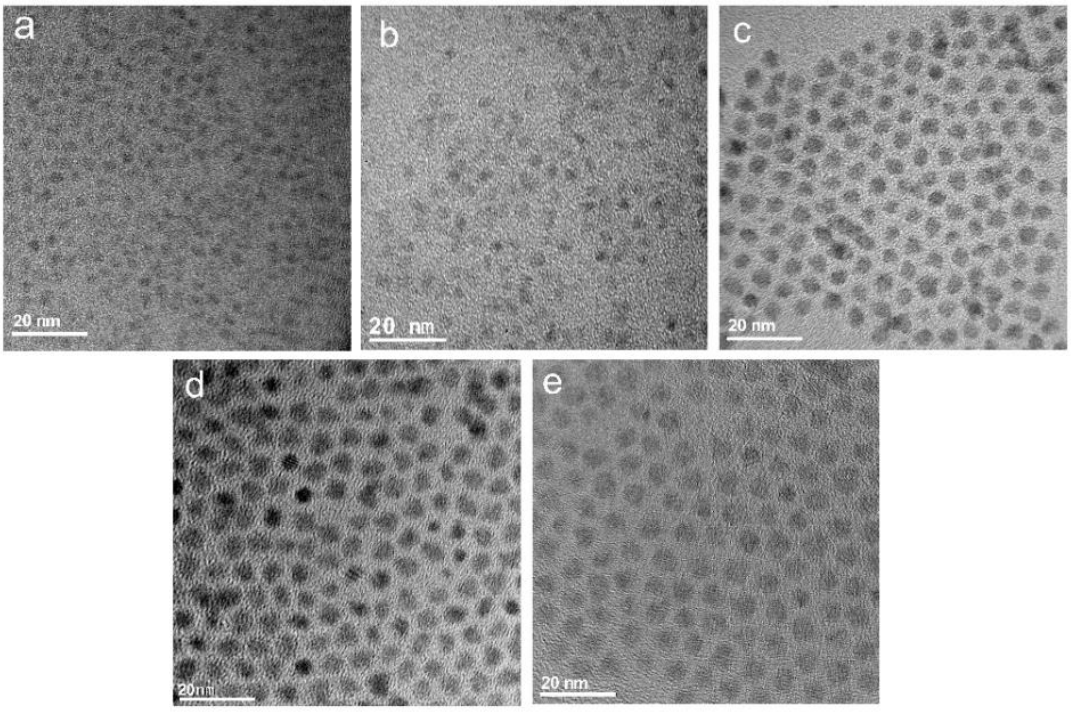

Figure 3.4. TEM imaging of PbS nanocrystals with OA ligands for core diameters of a) 3.0 nm, b) 3.5 nm, c) 4.9 nm, d) 5.0 nm, e) 6.1 nm.

We used FDTR, as illustrated in Fig. 3.5a to measure the thermal conductivity of samples of PbS NCSLs with core diameters of 3.0, 3.5, 4.9, 5.0, and 6.1 nm, and NCFs with core diameters of 3.0, 3.5, 4.9, and 6.1 nm. FDTR data (phase difference) is shown for representative samples of NCFs and NCSLs in Fig. 3.5b, where the good agreement between measurement and model fitting indicates reliable results of thermal conductivity. The fitting results are plotted in Fig. 3.5c, where the measurements of Ong *et al.* are included as a benchmark of comparison to our NCF measurements[16]. Lower and upper error bars in Fig. 3.5c represent the 10^{th} and 90ths quantiles of fit distributions gathered by a Monte Carlo estimation of uncertainty. All samples were coated with a Au transducer layer of 70 nm in thickness using electron-beam evaporation prior to FDTR measurement to enhance the thermoreflected signal. PbS nanocrystal specific heat was measured using differential scanning calorimetry (DSC).

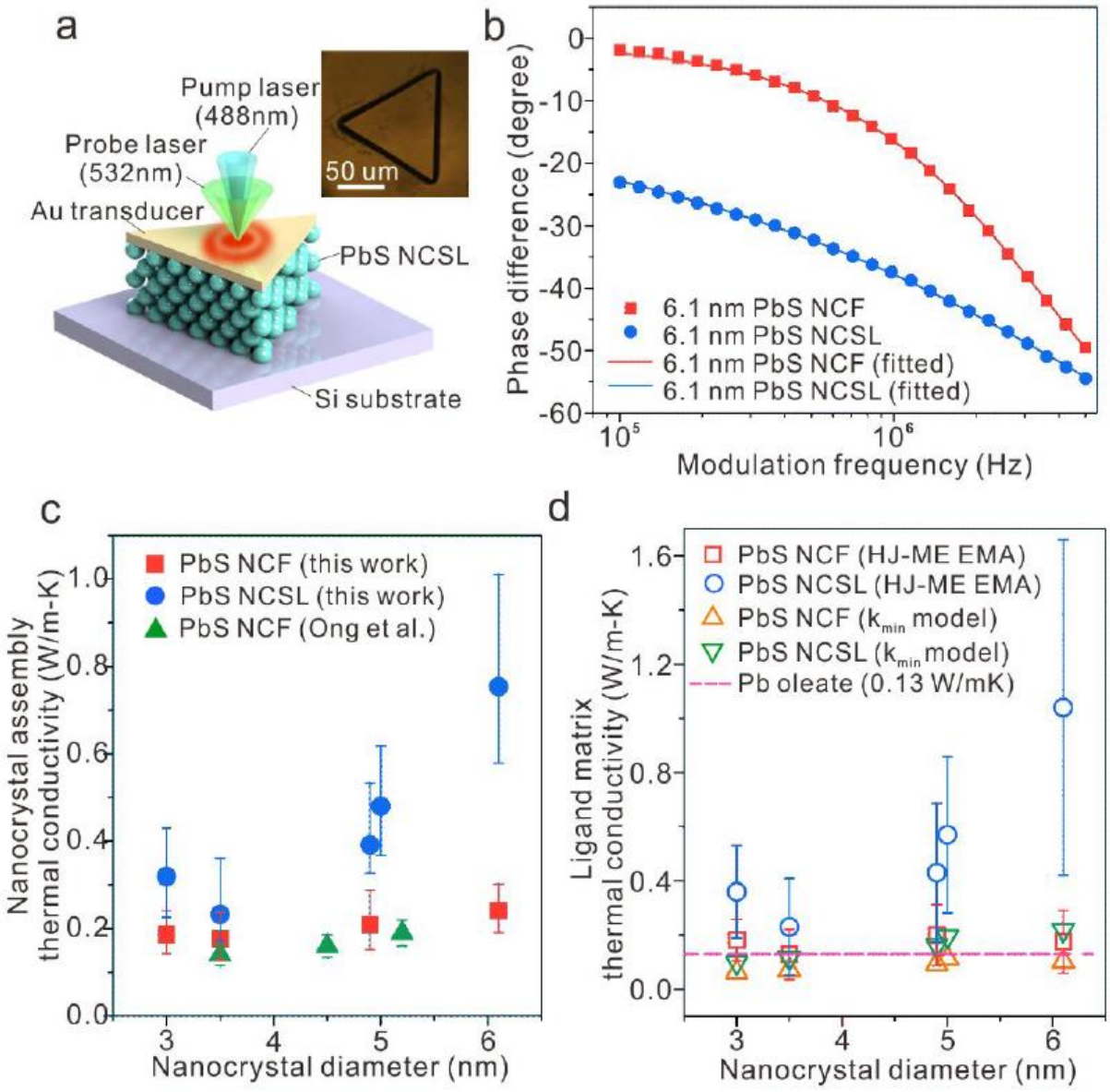

Figure 3.5. a) FDTR was used to probe *k* of PbS NCSLs and NCFs, where the inset shows an optical microscope image of a Au-coated NCSL; b) data and fits of measurements used to determine NSCL and NCF *k*, where good agreement between fits and data indicate reliable measurement, c) thermal conductivity measurements of NCFs and NCSLs as a function of PbS core diameter where error bars represent the 10th and 90th quantiles of fit distributions created using a Monte Carlo estimation of uncertainty; NCF measurements performed by Ong *et al.* agree well with our own measurements; d) ligand matrix thermal conductivity of NCSLs and NCFs

determined using the Hasselman Johnson Maxwell Euken (HJ-ME) effective medium approximation (EMA); results are compared to predictions of a minimum thermal conductivity model and the thermal conductivity of Pb-oleate wax.

We perform a sensitivity analysis on the FDTR model and find that it is largely controlled by spot size (r_{spot}) and Au thermal conductivity (k_{Au}), as shown in Fig. 3.6b. Spot size is well understood in our system and is unlikely to vary based on the sample under investigation. However, Au k could not be measured on NCSL samples since the four-point probe resistivity method requires a larger surface area than that shown in the inset of Fig 3.5a. Therefore, central values used in the fitting of NCSLs are based on resistivity measurements conducted on NCFs that are converted to thermal conductivity using the Wiedemann-Franz law. While this is likely an adequate approximation considering that PbS NCFs exhibit low electrical conductivities (thereby allowing most of the measured voltage to be a result of electron transport in the Au layer), actual values may deviate slightly due to differences in grain-boundary formation in the Au layer resulting from interlayer stresses that differ between the two nanocrystal systems. We therefore elected to include k_{Au} as a variable parameter in the fitting, resulting in high-quality fits that match multiple measurements shown in Fig. 3.6c. Mean-squared error (MSE) contours, as shown in Fig. 3.6d show that only fits that use values of k_{Au} that fall within a small range that is near the measurement done on NCFs result in high-quality fits.

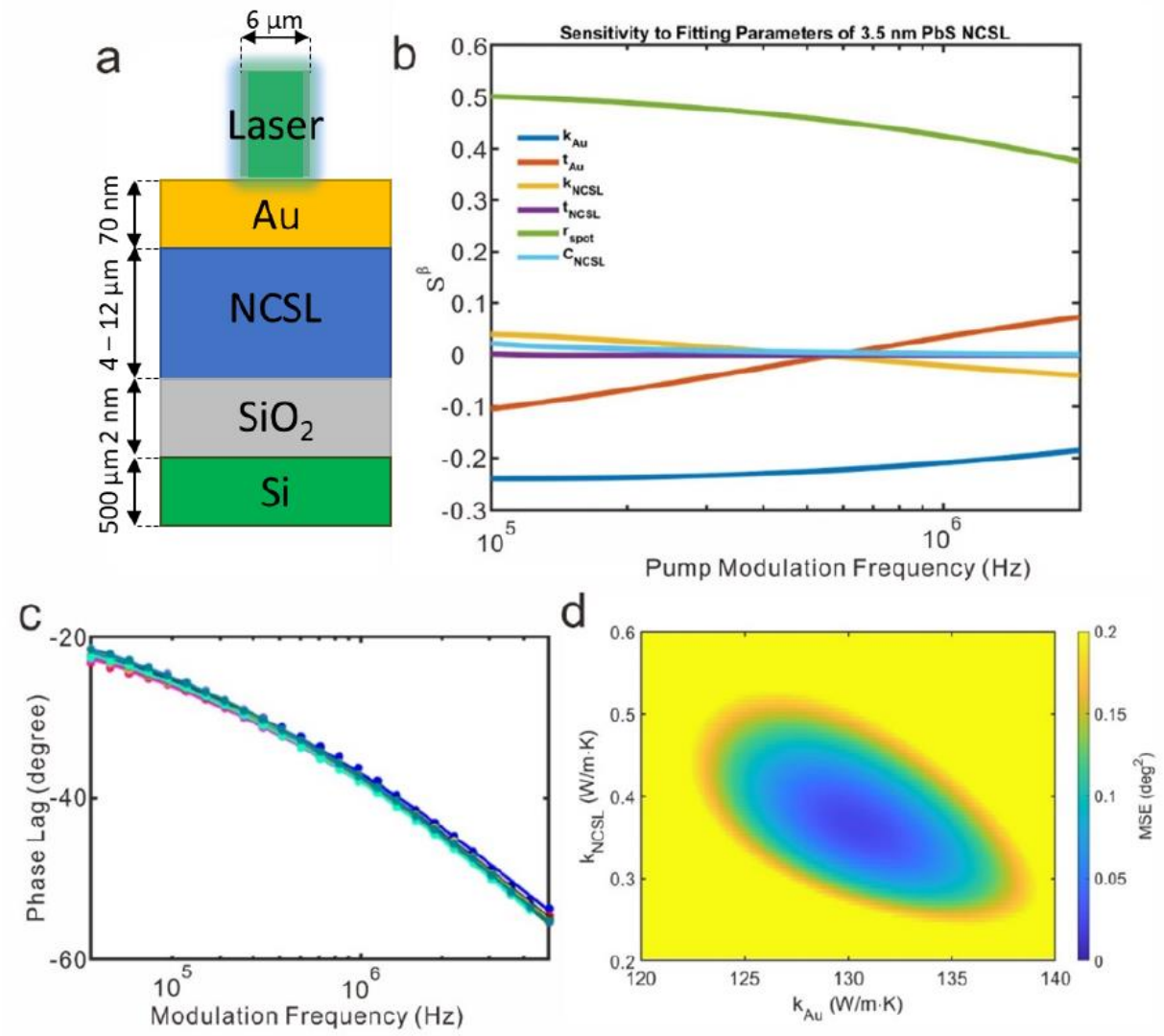

Figure 3.6. a) sample configuration (including typical layer thicknesses) used in FDTR measurements; b) sensitivity analysis of FDTR model of a NCSL with 3.5 nm PbS cores, c) phase data and model fits of measurements taken on different NCSL crystals, where the similarity between fits indicates measurement consistency, d) the mean squared error (MSE) contour plot highlights fit quality dependence on NCSL thermal conductivity (k_{NCSL}) and Au thermal conductivity (k_{Au}); only fits that use values of k_{Au} that reside within a narrow range and close to that measured on NCFs using four-point probe resistivity and the Wiedemann-Franz law yield low-MSE results.

We generated the error bars presented in Fig. 3.5c using an approach previously employed to study the effects of uncertainty in fitting parameters in measurements of interface resistances[60,61]. Each fitting parameter was modeled as a normally distributed random variable described by a mean value and standard deviation based on literature or experimental measurement, as shown for spot size as an example in Fig. 3.7. The uncertainty of each measurement was determined by sampling from the distribution of each fitting parameter 1000 times to create a matrix of 1000 combinations of fitting parameters which were input to the FDTR model to create 1000 fits of NC sample k. The distribution generated from each measurement of the same sample type belong to one statistical population and were therefore combined into a single distribution from which statistically meaningful information was calculated. These distributions are often non-normal and so the medians were used as the indicators of central tendency rather than the means. The distributions of NCSL and NCF thermal conductivities are shown in Fig. 3.8.

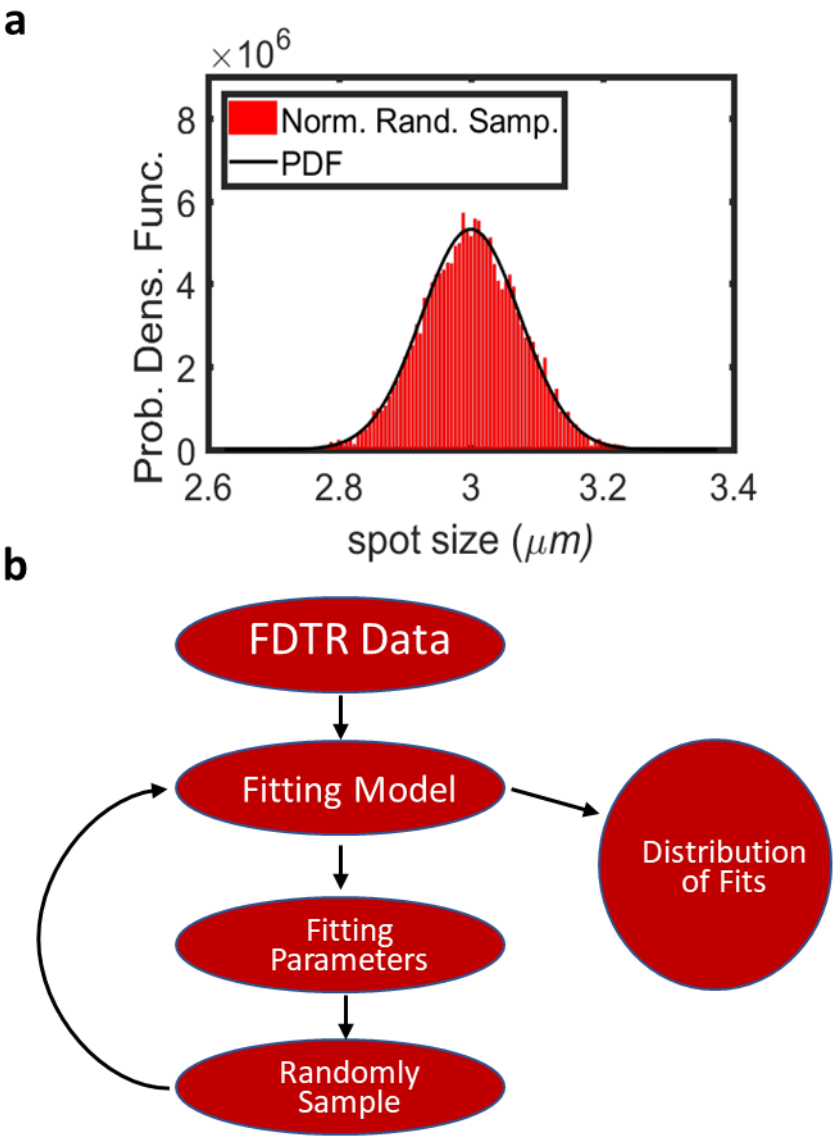

Figure 3.7. a) a normal random distribution was assigned to each parameter, like spot size, where the mean and variance were prescribed by experimental experience or literature, b) a flow chart of the uncertainty algorithm is presented; the fitting model is first used to determine rough fitting parameters, which were then modeled as random variables and sampled by the fitting model to create a distribution of fits to NC sample thermal conductivity.

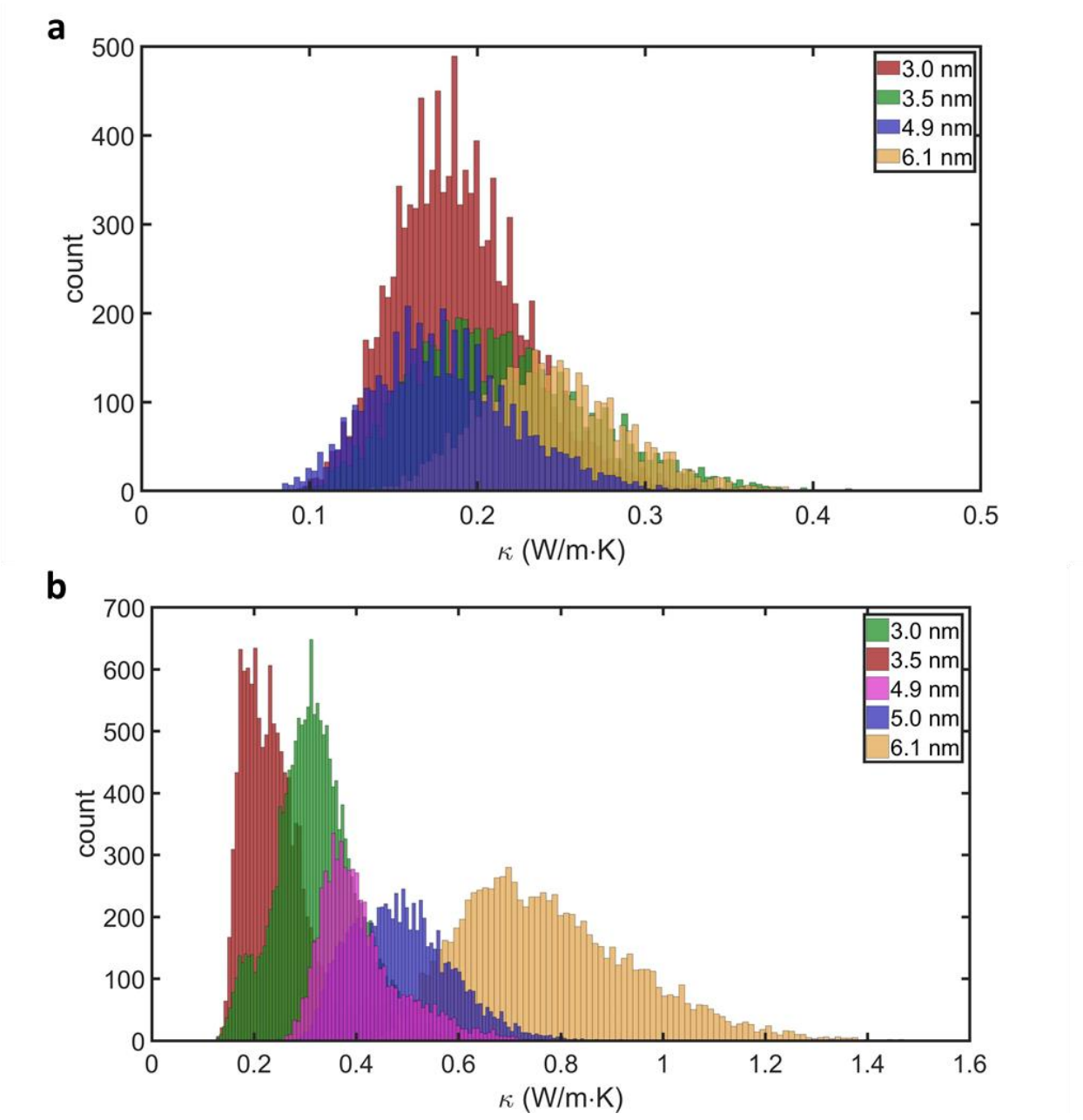

Figure 3.8. Thermal conductivity distribution of fits for a) 3.0, 3.5, 4.9, and 6.1 nm PbS NCFs and b) 3.0, 3.5, 4.9, 5.0, and 6.1 nm PbS NCSLs; distinct differences are present in the location of peaks of NCSL distributions but not of NCF distributions, indicating that thermal conductivity is a stronger function of core diameter in NCSLs.

The FDTR results shown in Fig. 3.5c reveal that k of PbS NCSLs generally exceed those of NCFs, and that the k of NCFs increased from $0.19 \pm 0.05/-0.04$ to $0.24 \pm 0.06/0.05\ \mathrm{Wm^{-1}K^{-1}}$ as the NC diameter increases from 3.0 to 6.1 nm, consistent with past research[16,54]. By comparison, k of NCSLs are up to thrice those of NCFs, particularly at higher diameters ($0.32 \pm 0.11/-0.09$ to $0.75 \pm 0.26/0.18\ \mathrm{Wm^{-1}K^{-1}}$), as k_{NCSL} experiences greater enhancement due to core diameter enlargement. The difference in k behavior between these two groups is reminiscent of that seen in crosslinked versus non-crosslinked iron oxide NCs[53], albeit due to different underlying mechanisms. PbS NCSLs feature weak vdW ligand-ligand interactions, so enhanced thermal transport cannot be attributed to improved ligand-ligand interactions resulting from chemical bond strength.

Our collaborators at the University of Washington performed stiffness measurements on the samples to better understand mechanical behavior and its relationship to thermal transport in these materials. The average speed of sound in a material is linked to the elastic modulus as

$$v_s \propto \sqrt{\frac{E}{\rho}} \tag{3.2.1}$$

where E and ρ are the Young's modulus and density. We therefore sought to measure E, and, having already known ρ through thermogravimetric analysis (TGA), determine the average sound speed which could be used as a basis for approximating thermal conductivity using the phonon gas model described in Eq. 1.1.11.

A Ubi-1 Nanoindenter by Hysitron was used to perform mechanical measurements. The machine, equipped with a diamond Berkovich tip, was initially calibrated with a fused silica

sample. 20 200 nm indentations were made per sample using a 3-segment (10s load, 5s hold, 10s unload) load cycle to get an average Young's modulus. The reduced modulus was calculated as

$$E_r = \frac{S}{2}\sqrt{\frac{\pi}{A}} \tag{3.2.2}$$

where S is the stiffness based on the unloading curve and A is the contact area (which is a calibrated function of depth). E_r is related to the Young's modulus of the sample (E) and that of the indenter (E_i) by

$$\frac{1}{E_r} = \frac{1-\vartheta^2}{E} + \frac{1-\vartheta_i^2}{E_i} \tag{3.2.3}$$

where ϑ and ϑ_i represent the Poisson's ratio of the sample and indenter, respectively. Values of the diamond tip are known, and a universal Poisson ratio of 0.3 is used for ϑ. Finally, longitudinal, transverse, and total sound speed were calculated as

$$v_L = \sqrt{\frac{E}{\rho}\left[\frac{1-\vartheta}{(1+\vartheta)(1-2\vartheta)}\right]} \tag{3.2.4}$$

$$v_T = \sqrt{\frac{E}{2\rho(1+\vartheta)}} \tag{3.2.5}$$

$$v_S = \frac{v_L + 2v_T}{3} \qquad 3.2.6$$

It should be noted that sound speed is the low-frequency limit of phonon group velocity, as it represents the slope of the dispersion relation, $\frac{\partial \omega_k}{\partial k}$, of acoustic phonon modes. In other words, the sound speed does not consider the velocity of non-acoustic modes or those outside the linear, low-frequency range of the acoustic branches, and therefore may not be fully representative of the average phonon group velocity invoked in Eq. 1.1.11.

Nanoindentation reveals that NCSLs possess Young's moduli that are up to thrice that of NCFs, as shown in Fig. 3.9f, increasing from 360 to 1770 MPa as opposed to 110 to 600 MPa. This increased diameter-dependence is the result of two phenomena, the first being an increased volume fraction of NC cores, as lower interparticle spacing allows for higher NC packing densities. We also attribute the higher stiffness to improved alignment and interdigitation of ligands, which we suspect increases with NC diameter and opposite surface curvature[62,63].

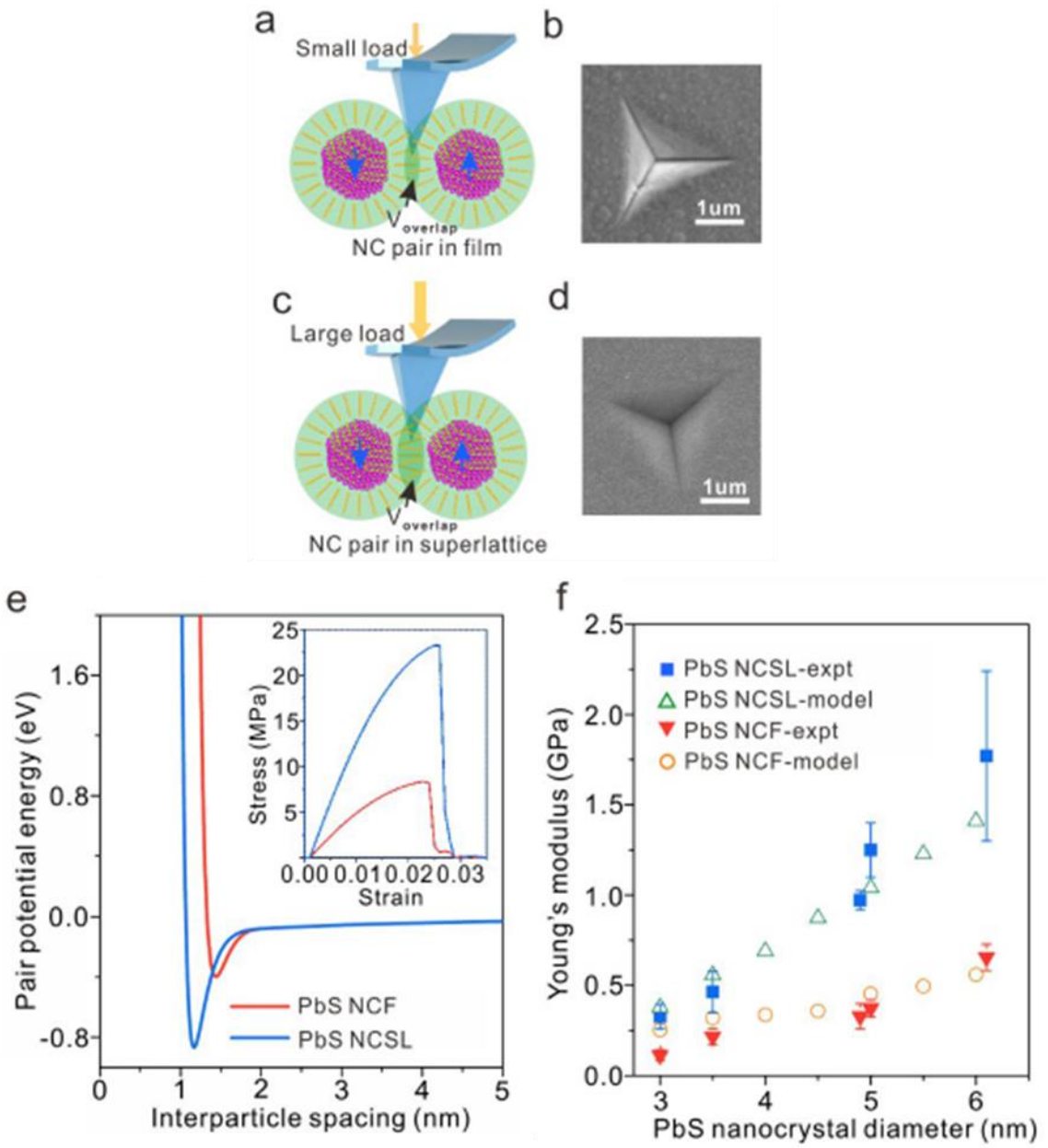

Figure 3.9. a,c) illustration of NCF and NCSL response to indenter load, respectively; the indenter penetrates equally in both circumstances despite unequal load due to the improved stiffness in NCSLs resulting from higher volume overlap, alignment, and interdigitation of ligands; b,d) SEM images of nanoindentation of an NCF and NCSL sample, respectively, e) NC pair potentials derived from coarse-grained modeling and the resultant stress-strain behavior in NCFs and NCSLs,

f) Young's modulus data obtained *via* nanoindentation compared to fitted results from coarse-grained model.

We used Young's modulus data to calculate the average speed of sound, as shown in Fig. 3.9f. v_s increases by approximately ~40 – 60% with increasing diameter in NCSLs, however this alone is insufficient to explain the strong diameter dependence of thermal conductivity observed in Fig. 3.5c (since k scales with $E^{1/2}$). Moreover, not only are our DSC measurements of C_V quite similar across all core diameters, but there is a decreasing trend which opposes that of k. This leads us to conclude that the final variable of Eq 1.1.11, average phonon mean free path, $\bar{\Lambda}$, must increase with NC diameter. We hypothesize that enhanced ligand and core ordering that results from increased core volume fraction results in increasing k with core diameter, and that this behavior is enhanced in NCSLs due to their improved long-range order resulting from the slow-diffusion process.

We used the Hasselman Johnson – Maxwell Euken (HJ-ME) effective medium approximation (EMA) to model thermal transport in NCSLs and NCFs in terms of the properties of the individual components of the composite NC material[64]. According to this model, thermal conductivity of composite materials that are constructed of a spherical dispersion (here, the nanocrystals) within a matrix (here, the oleic acid ligands) is a function of the dispersion thermal conductivity (k_{NC}), matrix thermal conductivity (k_m), NC core volume fraction (V_d), NC core radius (a), and core-ligand interfacial thermal conductance (G), as shown in Eq. 3.2.7.

$$k_{eff} = k_m \frac{2\left(\frac{k_d}{k_m} - \frac{k_d}{ah_c} - 1\right)V_d + \frac{k_d}{k_m} + \frac{2k_d}{ah_c} + 2}{2\left(1 - \frac{k_d}{k_m} + \frac{k_d}{ah_c}\right)V_d + \frac{k_d}{k_m} + \frac{2k_d}{ah_c} + 2} \quad 3.2.7$$

k_{eff} is obtained through our FDTR results to be $0.32 \pm 0.11/0.09$, $0.23 \pm 0.13/0.06$, $0.39 \pm 0.14/0.07$, $0.48 \pm 0.14/0.11$, and $0.75 \pm 0.26/0.18$ $\mathrm{Wm^{-1}K^{-1}}$ for NCSLs with core diameters of 3.0, 3.5, 4.9, 5.0, and 6.0 nm, and $0.19 \pm 0.05/0.04$, $0.18 \pm 0.06/0.05$, $0.21 \pm 0.08/0.06$, , and $0.24 \pm 0.06/0.05$ $\mathrm{Wm^{-1}K^{-1}}$ for NCFs with core diameters of 3.0, 3.5, 4.9, and 6.1 nm. k_d is assumed to be ~2.6 $Wm^{-1}K^{-1}$ based on previous work on thermal transport in undoped PbS[65–67]. h_c is set as 150 $\mathrm{Wm^{-2}K^{-1}}$ based on model fitting of other PbS nanocrystal materials[16]. Ong *et al.* define the volume fraction of an FCC system based on the face-diagonal dimension, $F_{dist} = 2d + 2L$, where d and L represent the core diameter and interparticle separation[16].

$$V_{cell} = \frac{\left[F_{dist}\cos\left(\frac{\pi}{4}\right)\right]^3}{4} \quad 3.2.8$$

$$V_d = \frac{\frac{4}{3}\pi a^3}{V_{cell}} \quad 3.2.9$$

V_{cell} represents the effective volume of a cell containing a singular core, since there are four cores per unit cell. The ratio of the core volume to this value is then taken as the volume fraction of cores within the structure in Eq. 3.2.9.

We performed a sensitivity analysis on Eq. 3.2.7 to assess the parameters that most strongly effect k_{eff}.

$$S_\beta = \frac{\partial \ln(k_{eff})}{\partial \ln(\beta)} \approx \frac{\Delta \ln(k_{eff})}{\Delta \ln(\beta)} = \frac{\ln\left(k_{eff,\beta_{adj}}\right) - \ln(k_{eff})}{\ln(\beta_{adj}) - \ln(\beta)} \qquad 3.2.10$$

β_{adj} was set as 1% of the nominal value of β. We assessed sensitivity at core diameters of 3.0, 3.5, 4.9, 5.0, and 6.1 nm and interpolated within this range, as shown in Fig. 3.10.

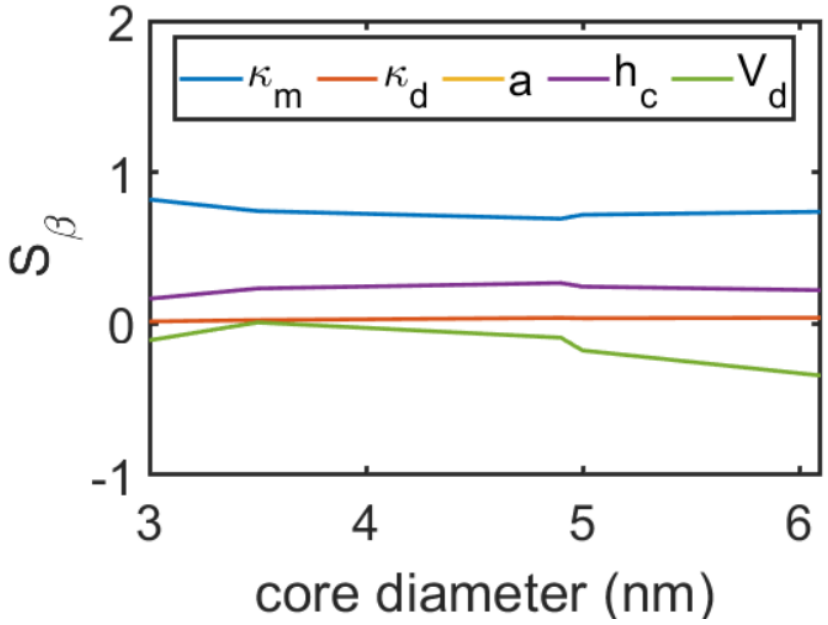

Figure 3.10. Sensitivity of the HJ-ME EMA to parameters β, shown in the legend.

The sensitivity analysis reveals that the model is overwhelmingly sensitive to k_m, consistent with prior work[53,54]. In order to better understand the role that ligands play in thermal transport in the PbS system, we rearranged Eq. 3.2.7 to solve for the matrix thermal conductivity, k_m. This expression takes the form of a quadratic equation, $\alpha k_m^2 + \mu k_m + \gamma = 0$, where

$$\alpha = 2(V_d - 1)\left(\frac{k_d}{ah_c} + 1\right)$$
$$\mu = k_{eff}(V_d + 2)\left(\frac{k_d}{ah_c} + 1\right) - k_d(1 + 2V_d) \quad 3.2.11$$
$$\gamma = k_{eff}k_d(1 - V_d)$$

and

$$k_m = \frac{-\mu \pm \sqrt{\mu^2 - 4\alpha\gamma}}{2\alpha} \quad 3.2.12$$

Eq. 3.2.12 grants two results, both of which are real positive values. We therefore matched this analytical approach with a numerical mean squared error minimization to determine the physically meaningful result. The agreement between the two techniques reveals nominal k_m of 0.36, 0.23, 0.43, 0.57, and 1.04 $\mathrm{Wm^{-1}K^{-1}}$ for NCSLs with nanocrystal diameters of 3.0, 3.5, 4.9, 5.0, and 6.1 nm, and nominal k_m of 0.18, 0.13, 0.20, and 0.18 $\mathrm{Wm^{-1}K^{-1}}$ for NCFs with nanocrystal diameters of 3.0, 3.5, 4.9, and 6.1 nm, as shown in Fig. 3.5d. The error bars in Fig. 3.5d represent the cumulative uncertainty in the parameters of Eq. 3.2.11 and 3.2.12:

$$\delta k_m = \left[\left(\frac{\partial k_m}{\partial k_{eff}}\delta k_{eff}\right)^2 + \left(\frac{\partial k_m}{\partial k_d}\delta k_d\right)^2 + \left(\frac{\partial k_m}{\partial h_c}\delta h_c\right)^2 + \left(\frac{\partial k_m}{\partial V_d}\delta V_d\right)^2 + \left(\frac{\partial k_m}{\partial a}\delta a\right)^2\right]^{1/2} \quad 3.2.13$$

where δk_{eff} is taken as the larger of the difference between the median and the 10th or 90th quantiles of fit. δk_d is set at 0.1 $\mathrm{Wm^{-1}K^{-1}}$ due to the consistency at which it is reported[65–67]. The HJ-ME EMA is not sensitive to h_c, which makes assessing its true value and dependency on core diameter and ligand-ligand interaction in the PbS system difficult[16,31]. δh_c was therefore overestimated as 100 $\mathrm{MWm^{-2}K^{-1}}$, based on the uncertainty reported by Ong *et al.*[16]. δa was set at 0.3 nm based on monodispersity observations in high-resolution TEM imaging. Uncertainty in interparticle spacing, δL (which effects δV_d) was liberally prescribed as 0.5 nm, though we expect that the true value is much lower.

The total uncertainties presented in Fig. 3.5d are decomposed by each contributor shown in Eq. 3.2.13, and are shown in Table 3.1 below. The contribution of k_{eff} is largest and decreases with increasing core diameter. δk_{eff} shows the opposite trend, meaning that its contribution to uncertainty is an artifact of the close relationship between the two values, as shown in the sensitivity analysis, rather than the magnitude of uncertainty in k_{eff}. A trend of increasing k_m is evident despite the size of the error bars, with most values greatly exceeding that of Pb-oleate wax ($k_{Pb-O} = 0.13$ $\mathrm{Wm^{-1}K^{-1}}$)[16] and liquid oleic acid ($k_{OA} \approx 0.22$ $\mathrm{Wm^{-1}`K^{-1}}$)[68].

	Core Diameter (nm)	3.0	3.5	4.9	5.0	6.1
Contribution to Uncertainty (%)	a	0.70	0.48	0.63	0.65	0.24
	V_d	14.07	0.03	3.61	16.53	28.87
	k_d	0	0	0	0	0
	h_c	7.74	7.33	18.73	20.21	11.19
	k_{eff}	77.49	92.16	77.02	62.61	59.70

Table 3.1. Contributions to uncertainty in k_m decomposed by parameter, where the sum of each column is unity. Uncertainty is almost entirely dominated by k_{eff} due to the solution's large sensitivity to that parameter.

This result reaffirms the notion that stronger ligand-ligand interactions that result from improved order and interdigitation act to increase effective thermal conductivity far past those of NCFs, which are bottlenecked by thermal transport across neighboring ligands. Additionally, NCSLs show an increase in k_m with increasing diameter due to the reduction in surface curvature of the cores which allows well-ordered ligands to interdigitate better. By contrast, NCF k_m is insensitive to surface curvature because its effects are obscured by disordered NC packing and consequent ligand randomness. Ligand order and its impact on thermal transport appears to be analogous to thermal transport in polymers, where chain alignment improves heat conduction along the molecule's backbone.

Heat transfer in polymers and other amorphous materials has been successfully predicted by Cahill's minimum thermal conductivity model[69–72]. This model only considers incoherent phonon modes, or vibrational waves that travel randomly. We employed this model to understand how well such a model predicts k_m of NCFs and NCSLs. The high temperature limit of the minimum thermal conductivity model is

$$k_{min} = \left(\frac{9\pi}{16}\right)^{1/3} k_B n_{eff}^{2/3} v_{s,m} \quad 3.2.14$$

where k_B, n_{eff}, and $v_{s,m}$ represent the Boltzmann constant, atomic density, and sound speed in the matrix. Not all vibrational modes are active at room temperature, so we adjusted the atomic density to reflect the degree of phononic activation using the heat capacity.

$$n_{eff} = \frac{C_m}{3k_B} \quad 3.2.15$$

Here, C_m represents the volumetric heat capacity of the ligand matrix. Eq. 3.2.14 can therefore be rewritten as

$$k_{min} = \left(\frac{\pi}{16}\right)^{1/3} k_B^{1/3} C_m^{2/3} v_{s,m} \quad 3.2.16$$

where matrix heat capacity was taken to be $2.043\ \mathrm{Jkg^{-1}K^{-1}}$ based on reporting in the literature[73]. $v_{s,m}$ was calculated using Eq. 3.2.1 based on the Young's modulus of the matrix, E_m, which was

derived from the composite (E) and nanocrystal (E_{NC}) Young's modulus according to Halpin-Tsai theory[74] which has been previously applied to NC systems[53,75].

$$\frac{E}{E_m} = \frac{1 + \delta\eta V_d}{1 - \eta V_d} \tag{3.2.17}$$

$$\eta = \frac{E_{NC}/E_m - 1}{E_{NC}/E_m + \delta} \tag{3.2.18}$$

δ in Eq. 3.2.17 and 3.2.18 represents the shape parameter for the filler material, which here is spherical, so $\delta = 2 + 40 \cdot V_d$.

The model predictions of k_m are shown in Fig. 3.5d. While it accurately traces the calculations of the HJ-ME model for NCFs, it grossly underestimates values for NCSLs. This result further substantiates the hypothesis that oleic-acid ligands are disordered in the PbS NCFs (and therefore behave thermally similar to an amorphous material), and that they are comparatively better ordered in NCSLs and are therefore able to carry more heat. This model assumes that phonon mean free path is approximately half the phonon wavelength, resulting in mean free paths close to the interatomic spacing of the amorphous solid. The mismatch between k_m of NCSLs predicted by this model and the HJ-ME model suggests that longer-range phonon modes may be present within the ligand matrix that enhance thermal transport.

In this study, we showed that a slow-diffusion method facilitates the development of PbS nanocrystal superlattices that exhibit superior core and ligand ordering compared to NC films prepared according to a quick-drying process. We measured thermal conductivity using FDTR and

elastic modulus using nanoindentation and found threefold thermal and mechanical enhancements in NCSLs compared to NCFs. Our effective medium approximation and minimum thermal conductivity modeling suggests that improved core ordering also increases interdigitation and alignment of ligands, improving thermal transport in the ligand matrix and increasing effective thermal conductivity. We find that both ligand matrix and effective thermal conductivities increase with core diameter due to the decreasing surface curvature that allows for improved ligand-ligand interactions. Our work demonstrates that improved ordering sits with crosslinking[53] and ligand backbone tuning[54] as an effective method to boosting thermal and mechanical robustness in colloidal nanocrystal solids, and that it may serve as a viable technique to improve their performance in next-generation technology.

3.2.1 Statement of Contribution

Alexander D. Christodoulides, Lingyun Dai, and Jonathan A. Malen: FDTR measurement of thermal conductivity.

Alexander D. Christodoulides and Jonathan A. Malen: MC estimation of uncertainty of thermal conductivity data.

Alexander D. Christodoulides, Jonathan A. Malen, Zhongyong Wang, and Robert Wang: EMA modeling of NCSL and NCA systems.

Yang Zhou and Junlan Wang: Nanoindentation and mechanical measurements.

Zhongyong Wang, Rui Dai, Yifei Xu, Qiong Nian, and Robert Wang: minimum thermal conductivity modeling, pair potential modeling, atomistic molecular dynamics simulations

4 Two-Dimensional Perovskites

4.1 Thermal Transport in Three-Dimensional Perovskites and Motivation

Perovskite materials are characterized by the general chemical formula ABX_3, where sites A and B are occupied by cationic molecules and X is occupied by an anionic molecule. This structure is recognizable for the way the anionic molecules are often depicted as forming octahedra surrounding the B sites. Such materials are found in nature but are also synthesizable in the laboratory and have been found to exhibit wide-ranging properties useful in a myriad of applications[76].

Halide perovskites, or those for which the X site is occupied by a halide atom (X = F, Cl, Br, or I), are semiconducting materials that have found use in many areas of technology. These structures have been lauded for properties including easy solution processability[77], enhanced defect tolerance[78–80], long-carrier lifetime[78,79,81,82], optical bandgap suitability[83], and high absorption coefficient[84]. The first reports of three-dimensional hybrid organic-inorganic perovskites (HOIPs) of the sort came out in 1978[85,86], but research on their exceptional photovoltaic and optoelectronic properties[77–79,83,84,87,88] only began in the 1990s. Since then, incredible strides have been made in the improvement of HOIP photovoltaic power conversion efficiency (PCE) and light emitting capabilities. Specifically, the PCE of $MAPbI_3$ (where MA represents methylammonium, or CH_3NH_3) has been optimized from less than 3% to 24% in just over a decade[84,87,89], and its external luminescence efficiency has been improved to make it a contender for future lasing applications[78,84,87].

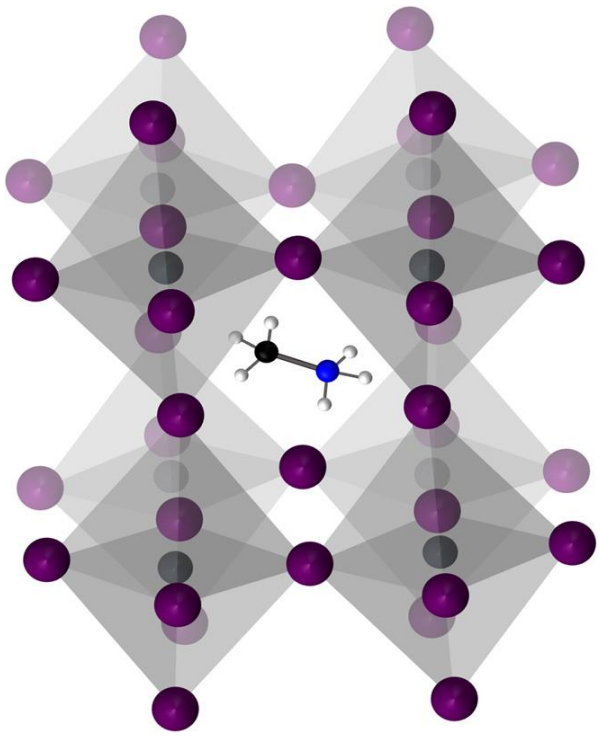

Figure 4.1. The structure of methylammonium lead iodide, or $MAPbI_3$, where methylammonium is CH_3NH_3 [90]. This material exhibits high power conversion efficiency (PCE) and good external luminescence efficiency which has made it the centerpiece of perovskite research for the past two decades.

Research on HOIPs has largely been focused on properties pertinent to their implementation as photovoltaic and optoelectronic devices, particularly stability and charge transport. However, concentration began to shift towards thermal transport after ultralow thermal conductivity was discovered in $MAPbI_3$, a HOIP well-known for its exceptionally high PCE[91]. This new information was at once exciting and problematic: ultralow thermal conductivity presents a huge challenge for HOIP-based solar cells due to their typically high operational temperatures and maintenance regulations[92] but also stages potential for thermoelectric capabilities, which has

been further realized by studies of high Seebeck coefficient compared to other solution-processed materials[93–96].

Halide perovskites are classified as phonon glasses while also as electron crystals (PGECs) due to the ballistic charge transport and diffusive phonon transport that are simultaneously present[90], and are therefore sometimes referred to as "crystalline liquids"[97]. This phenomenon results from efficient charge transport across a large electronic bandwidth but low thermal transport occurring across a comparatively small phonon bandwidth. The exact mechanisms by which this occurs has been debated, but it is thought to result in scattering of long-range vibrational modes, leaving mostly local, intermolecular modes to diffusively carry heat across small length scales[13,90,98–101].

In their seminal study, Pisoni *et al*. observed decreasing thermal conductivity with increasing temperature in $MAPbI_3$, and an ultralow thermal conductivity of $0.5\ \mathrm{Wm^{-1}K^{-1}}$ for single crystals at room temperature[91]. They employed the Callaway model[102] to explain this behavior in terms of scattering event relaxation rates, τ:

$$k_l = C_V T^3 \int_0^{\theta_D/T} \tau(x) \left[\frac{x^4 e^x}{(e^x - 1)^2}\right] dx \qquad 4.1.1$$

where scattering mechanisms (boundary, defect, and Umklapp) are treated as independent, parallel events (according to Matthiessen's rule) such that $\tau^{-1} = \sum_i \tau_i^{-1}$. In Eq. 4.1.1, $x = \hbar\omega/k_B T$ and θ_D is the Debye temperature. Only Umklapp scattering exhibits temperature dependence, so the authors attributed the trend they observe to increased phonon-phonon scattering commensurate with the activation of additional modes, as is expected in a crystalline material. They claim that

resonant scattering, emergent from a high density of modes with similar energies, is responsible for increased scattering beyond 160 K that create a glass-like regime consistent with the "crystalline liquid" previously described. Moreover, these scattering events, which they liken to those seen in materials with dynamical disorder[103], are suggested to be induced by the activation of rotational degrees of freedom of the CH_3NH_3 molecule, resulting in an ultralow thermal conductivity of $0.5\ \mathrm{Wm^{-1}K^{-1}}$ at room temperature[91]. Below the activation temperature of these dynamical disorder modes, it is believed that the orientational distribution of the A site molecule dictates thermal transport anisotropy[98]. However, while dynamical disorder of the A site molecule has been extensively studied, its effect on thermal transport has remained ellusive[91,99,101,104,105].

Elbaz *et al.* identified room temperature thermal conductivities of different lead-halide perovskites using FDTR to understand common underlying phonon transport mechanisms[101]. Their study considered $MAPbX_3$, where X = Cl, Br, and I, as well as $APbBr_3$, where A = MA, FA (formamidinium), and Cs. While Pisoni *et al.* identify dynamic disorder of the noncentrosymmetric A site cation as the cause of ultralow thermal conductivity, FDTR measurements revealed a weak A site dependency (~10% variation) and a strong halide dependency. This result was impactful considering that $CsPbBr_3$, a structure with a centrosymmetric A site molecule, should, according to Pisoni *et al.*, exhibit high thermal conductivity compared to when A = MA and FA due to the muted effects of dynamical disorder. Using nanoindentation and kinetic theory, Elbaz *et al.* identified that low-frequency acoustic phonon speed (sound speed) differentiates thermal transport in these perovskites, and that optical phonons contribute little to lattice thermal conductivity. Further, they used the thermal conductivity accumulation function with a Bon von Karman adjustment to the acoustic branches of the dispersion relation to study size dependence of resonant scattering mechanisms. They found that such scattering only impacts thermal conductivity in

structures with grains of ~50 nm or smaller, and that all perovskites exhibit similar accumulation functions, suggesting that low thermal transport in these materials is a consequence of low frequency phonon group velocity[101].

While three-dimensional perovskites show great potential in next generation technology, they are often unstable under ambient conditions. $MAPbI_3$, for example, has been demonstrated to rapidly degrade into solid PbI_2 and vaporous MA^+ and I^- even while subjected to dark vacuum environments[106,107]. Degradation is accelerated by oxygen[108], moisture[108–110], light[109,111,112], and heat[109–112], and control techniques such as encapsulation[89,113] and pinhole control[114] fail to improve lifetimes to something that would be comparable to Si- or Ga-based compounds. Two-dimensional, layered perovskites have therefore been studied as potential avenues towards improving stability while maintaining the positive attributes of three-dimensional HOIPs like solution processability and excitonic effects that make them competitive photovoltaics[115–117]. Many varieties of two-dimensional perovskites have been developed, and while their photovoltaic performance and stability characteristics have been extensively studied[109,118], their thermal behavior, which is critically important towards thermal management, has remained unexplored. The two following studies aim to illuminate the thermal transport phenomena that result in ultralow thermal conductivity in two families of two-dimensional perovskites: $BA_2MA_{n-1}Pb_nI_{3n+1}$ Ruddlesden-Popper (RP) perovskites, and $\chi MnCl_4$ ($\chi = (C_nH_{2n+1}NH_3)_2MnCl_4$ for n = 10 and 12, termed "C_{10}" and "C_{12}" respectively, and $\chi = (NH_3(CH_2)_4C_6H_5)_2$, or "$C_4$-phenyl").

4.2 $BA_2MA_{n-1}Pb_nI_{3n+1}$ Ruddlesden-Popper Perovskites

The success and potential of $MAPbI_3$ motivated the development of a more stable two-dimensional Ruddlesden-Popper (RP) perovskite, $BA_2MA_{n-1}Pb_nI_{3n+1}$. In this structure, $MAPbI_3$-based perovskites are layered between organic spacer layers composed of butylammonium (BA), as shown in Fig. 4.2. Here, *n* represents the number of repeated units of perovskite octahedra per inorganic layer, such that the structure becomes $MAPbI_3$ as $n \rightarrow \infty$. The inclusion of hydrophobic BA improves the perovskite's stability compared to $MAPbI_3$, and even reduces its rate of heat-based degradation at 80 °C[109,117,119,120]. Further, these RP phases exhibit PCEs of ~12.5%, which are among the highest reported for lower-dimensional perovskites[109,121,122]. However, while they were known to be laden with promising photovoltaic properties, their thermal transport properties were not understood. Their thermal conductivities were expected to be ultralow like that of their relative, $MAPbI_3$, however reduced dimensionality and structural complexity make such an approximation inappropriate for design purposes.

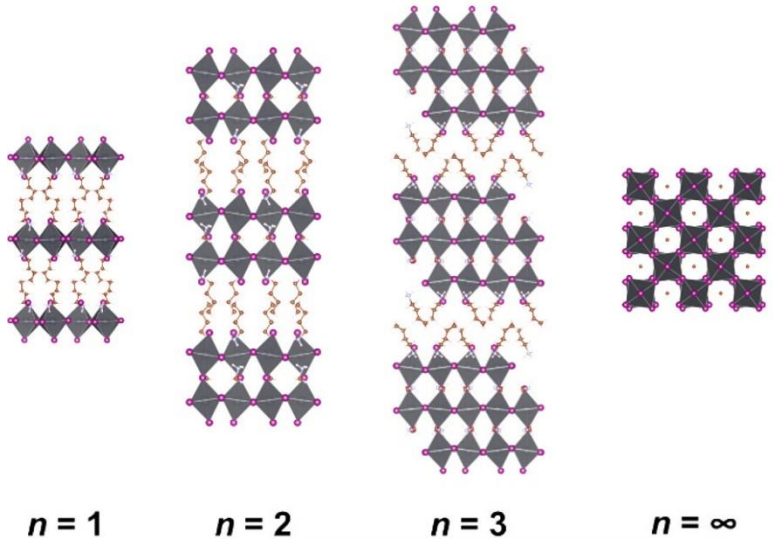

Figure 4.2. Crystal visualization of $n = 1 – 3$ members of the $BA_2MA_{n-1}Pb_nI_{3n+1}$ family, where *n* represents the number of repeated perovskite octahedra within each inorganic layer.

Knowledge of the thermal conductivity of $BA_2MA_{n-1}Pb_nI_{3n+1}$ RP phases has two primary values, the first of which is the practical need to understand thermal transport to predict and manage thermal loads during device operation. The second is the enhancement of our phenomenological understanding of thermal transport in materials with nanometer-scale two-dimensional architectures. The organic-inorganic repeating unit shown in Fig. 4.2 is highly reminiscent of a superlattice: a periodic structure composed of two or more materials. Such materials, like GaAs/AlAs and $(SrTiO_3)_m/(CaTiO3)_n$, exhibit signatures of coherent phonon transport in their thermal conductivities when layer thickness is low enough[123,124]. Low layer thickness and correspondingly high interface density (number of interfaces per unit length) is typically observed to decrease thermal conductivity due to increased boundary scattering and the restriction of long-wavelength and long mean free path phonon modes. However, when layer thickness is sufficiently low, coherent phonons, or those that emerge from the secondary periodicity of the structure, propagate successfully across these interfaces and therefore sometimes have mean free paths that exceed the period of the structure. These phonons are often described as exhibiting "wave-like" transport qualities as compared to other "particle-like" modes that scatter at the interfaces.

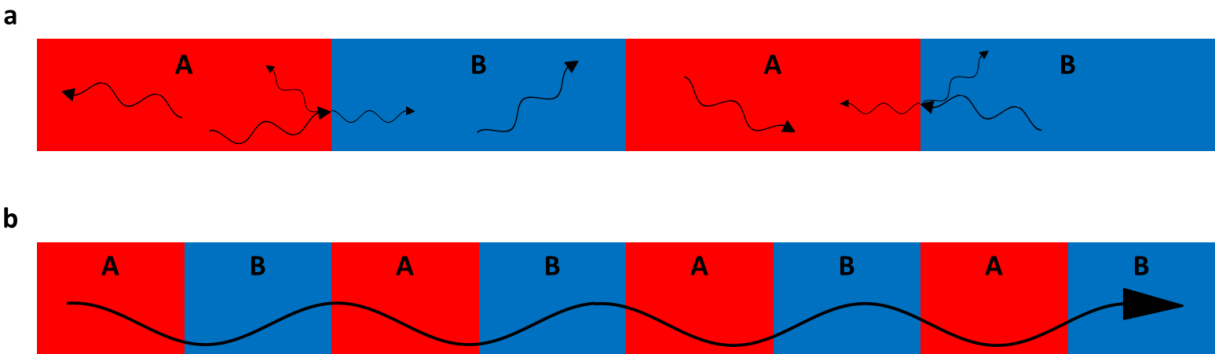

Figure 4.3. a) When interfaces are far apart, heat is primarily transported within layers by phonon modes that exist in the bulk of the constituent materials (here denoted by A and B). These phonons scatter heavily at interfaces and are therefore classified as ‘particle-like’ modes. b) When interfaces are close enough together, phonon modes that do not necessarily exist in the pure form of either constituent material but are rather built from the superstructure (coherent phonons), propagate across interfaces seamlessly, and are hence called ‘wave-like’ modes.

Coherent phonons have been demonstrated to carry significant amounts of heat resulting in elevated thermal conductivity compared to superlattices with lower interface densities[123,124]. However, these enhancements are often muted by imperfect interfaces that disrupt periodicity. We were therefore interested to determine whether coherent phonon effects could be observed in the thermal conductivity of $BA_2MA_{n-1}Pb_nI_{3n+1}$, where interface density is controlled by tuning n. Secondary periodicity and coherent phonons in two-dimensional perovskites had been previously studied[125–127], however their effects on thermal conductivity were contested. While one study identified longer lifetimes of transient reflectance oscillations in $(PEA)_2Pb_nI_{3n+1}$ (PEA = phenethylammonium) in higher n structures as indicative of higher thermal conductivities[128], another employed atomistic simulation to conclude that thermal conductivity of $SrTiO_3$-based RP phases should decrease with increasing n[129]. These discrepancies left ambiguity surrounding coherent phonon contributions to thermal conductivity in two-dimensional perovskites which we sought to clear with direct measurement.

Our collaborators at Northwestern University and Argonne National Laboratory created thin film $BA_2MA_{n-1}Pb_nI_{3n+1}$ RP perovskites of n = 1 – 4 as well as single crystals of n = 3 – 6. Single crystals were synthesized according to methods previously employed[116,120,130] which

generally involve precipitation from precursor solution. Thin films were prepared using a modified hot-casting method[109] in which samples were spin-coated onto pre-heated silicon wafers (n-type, Sb doped; 0.007 to 0.02 Ω·cm in resistivity corresponding to dopant concentration of 1018 – 1019 cm^{-3}; 700 µm in thickness).

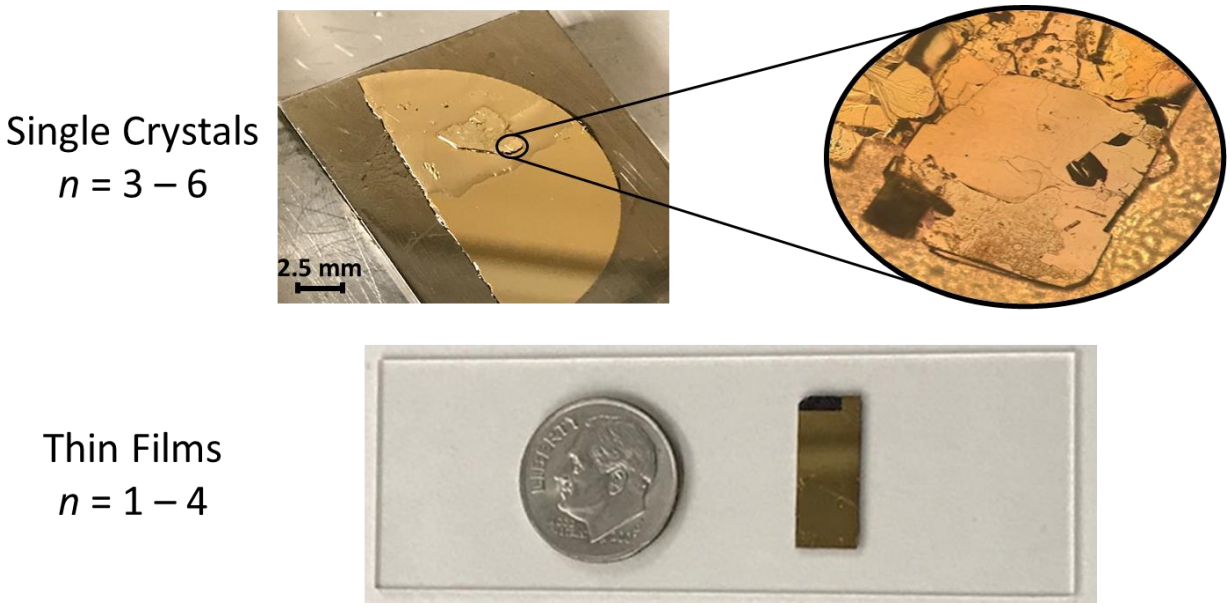

Figure 4.4. Single crystals (top) and thin films (bottom) of $BA_2MA_{n-1}Pb_nI_{3n+1}$ perovskites after being coated with a thin layer of Au. Crystals vary in size, and tend to increase in size with increasing *n*. The crystal depicted here is attached to quartz with a thin layer of epoxy that covers the top half of the wafer.

We adhered single crystals to SiO_2 (quartz) substrates using either carbon tape or non-degassing epoxy while in an Ar glovebox to limit harmful exposure to ambient conditions. A ~90-115 nm Au transducer layer was sputtered on the crystals once the epoxy was fully cured using a Perkin-Elmer 6J sputtering system. Thin films were also coated with Au (~70 nm) but with a Lesker PVD250 Electron-Beam evaporator system instead. Perovskite thin film and Au layer

thicknesses were measured using a Tencor P15 Profilometry System. Au layer thermal conductivity was calculated from electrical resistivity measurements (done using a four-point probe resistivity method) *via* the Wiedemann-Franz law. Sample properties are tabulated in Table 4.1.

		sample type						
		thin film samples				single crystal samples		
parameter	Layer	Si	SiO_2	RP Perovskite	Au	SiO_2	RP Perovskite	Au
	κ (W/m·K)	130	0.14	-	150-190	1.3	-	130-150
	C (MJ/m^3·K)	1.63	1.67	0.84-1.14	2.50	1.67	0.84-1.14	2.50
	t (nm)	5E+05	2	34-244	67-70	5E+05	5E+03	93-112
	spot size (μm)	3						

Table 4.1. Parameters relevant to FDTR measurement and modeling. Certain values, such as Au thermal conductivity and thickness, are sample dependent and have slight variations. Volumetric heat capacity is not variable across different samples, but is rather a function of *n*.

We measured the thermal conductivities of $n = 1 – 4$ thin films and $n = 3 – 6$ single crystals of $BA_2MA_{n-1}Pb_nI_{3n+1}$ RP perovskites using FDTR. Our fitting required knowledge of volumetric heat capacity, $C_{v,n}$, which was not directly measured. We instead made estimations based on the molar heat capacities of the RP phases' constituent molecules: BA, $MAPbI_3$, and PbI_4.

$$C_{mol,n} = N_{n,BA}C_{mol,BA} + N_{n,MAPbI_3}C_{mol,MAPbI_3} + N_{n,PbI_4}C_{mol,PbI_4} \qquad 4.2.1$$

Here, $N_{n,x}$, and $C_{mol,x}$ represent the number of molecule x per unit cell and the molar heat capacity of that molecule. Molar heat capacities of $MAPbI_3$ and PbI_4 were gathered from the literature[131,132]. That of BA was estimated using a DFT simulation designed to calculate the response of a butylammonium molecule to a physical perturbation. $C_{mol,n}$ was converted to specific heat by dividing by molar mass.

$$c_{m,n} = \frac{C_{mol,n}}{M_n} \qquad 4.2.2$$

We finally convert to volumetry heat capacity by multiplying with density:

$$C_{v,n} = c_{m,n}\rho_n \qquad 4.2.3$$

These calculations yielded $C_{v,n}$ of 0.84, 0.98, 1.04, 1.08, 1.11, and 1.14 $MJm^{-3}K^{-1}$ for n = 1 – 6 RP perovskites. That of n = 1 was externally reported to be 1.18 $MJm^{-3}K^{-1}$ based on molecular dynamics simulations[133]. The 36% increase from our estimation is mostly inconsequential in FDTR fitting due to relative insensitivity of the model to C_v for thin films, as shown in Fig. 4.5.

The degree to which FDTR fitting is affected by any one parameter listed in Table 4.1 is assessed through a sensitivity analysis as outlined in section 1.4. Model sensitivity to each term in the fitting, S_β, is shown for thin films and single crystals of $BA_2MA_{n-1}Pb_nI_{3n+1}$ in Fig. 4.5. Sensitivity to sample thermal conductivity, k_{RP}, is different between the two sample groups since single crystals are significantly thicker. The dissonance between sample and Au thermal conductivity encourages lateral heat diffusion, and the increased thickness of single crystals further

exacerbates this tendency, reducing cross-layer heat transfer and therefore lowering sensitivity to layers beneath the Au.

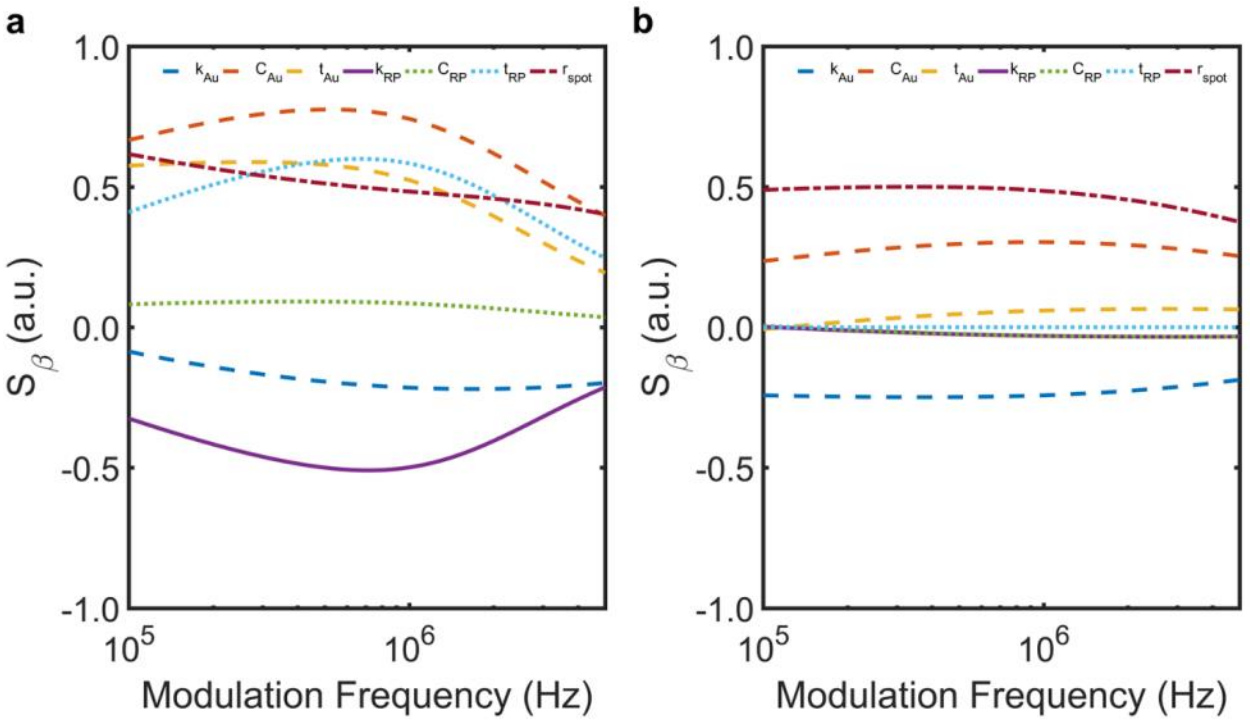

Figure 4.5. Relative sensitivity of the model used to fit FDTR data to parameters outlined in Table 4.1 for a) thin films and b) single crystals of $BA_2MA_{n-1}Pb_nI_{3n+1}$. Sensitivity to the thermal conductivity for single crystals is lower than that for thin films due to the increased thickness of the RP layer.

Nominal phase difference data was collected *via* FDTR at pump modulation frequencies ranged logarithmically from 100 kHz to 5 MHz for $n = 1 – 4$ thin films and $n = 3 – 6$ single crystals. Examples of data for each sample type are shown in Fig. 4.6a. Data collected for crystals show a smaller spread compared to those collected for thin films, however all data are fit well by the model. Nominal fits are shown as semitransparent data points in Fig. 4.6b. Opaque points are

created through a Monte Carlo (MC) analysis of uncertainty, the method for which is discussed for PbS nanocrystal solids in section 3.2. In brief, every modeling parameter is treated as a normally distributed random variable with a standard deviation based on observation or literature, shown in Table 4.2, such that 95% of each parameter's distribution falls within 2σ of the central value. Upper and lower error bars represent the 90th and 10th quantiles of the distribution of fits generated by the MC analysis. Histograms of the distributions for each sample type are shown in Fig. 4.7.

standard deviation (% of input)	Layer	Si	SiO_2	RP Perovskite	Au
	κ	2.5	2.5	-	2.5
	C	2.5	1	10	1
	t	0	2.5	5	2.5
	spot size	2.5			

Table 4.2. Standard deviations, σ, used to describe each modeling parameter as a normally distributed random variable. Each value is set according to literature or experimental observation.

Generally, the data suggests that the thermal conductivities of all perovskites are ultralow, with those of n = 1 – 4 thin films measuring at $0.37 \pm 0.13/0.12$, $0.17 \pm 0.08/0.07$, $0.21 \pm 0.05/0.04$, and $0.19 \pm 0.04/0.03$ $\mathrm{Wm^{-1}K^{-1}}$, and those of n = 3 – 6 single crystals measuring even lower at $0.08 \pm 0.06/0.04$, $0.06 \pm 0.04/0.03$, $0.06 \pm 0.03/0.03$, and $0.08 \pm 0.07/0.04$ $\mathrm{Wm^{-1}K^{-1}}$. Thermal conductivities appear to decrease with increasing n, as would be expected in a primarily wave-like regime as coherent phonons increasingly become hindered by the increased period length, but plateau at higher n. Thermal conductivity measurements of n = 3

– 6 single crystals are among the lowest reported for fully dense solids[6]. It also appears that thermal conductivities of n = 3 and 4 thin films are significantly larger than those of single crystals.

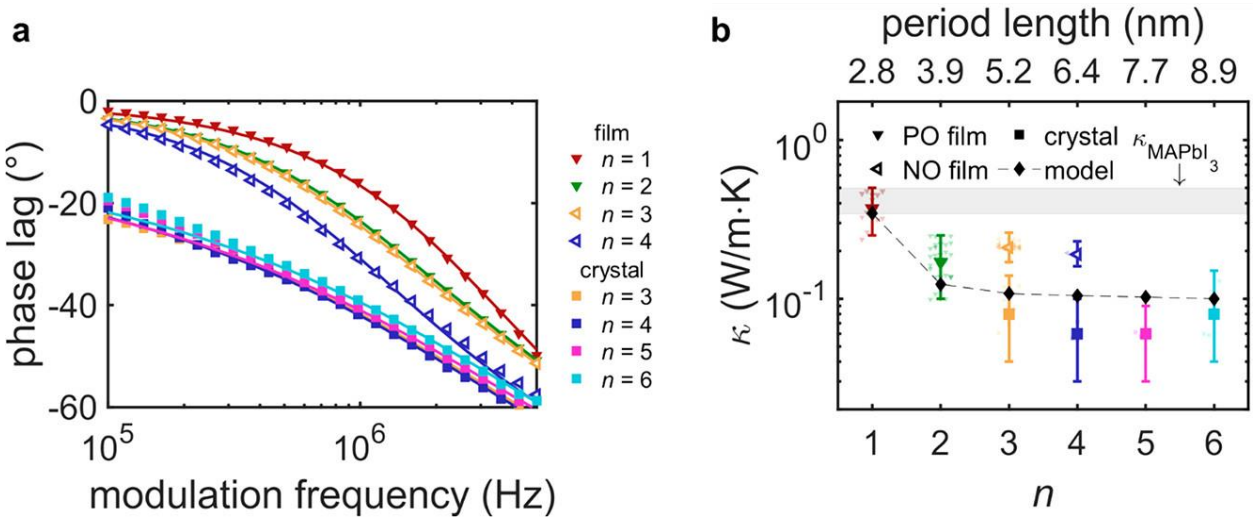

Figure 4.6. a) phase difference data and fits plotted against pump modulation frequency for thin films and single crystals of $BA_2MA_{n-1}Pb_nI_{3n+1}$. The differences in trends are indicative of differences in the heat transfer that occurs within the sample due to, among other things, variation in RP thermal conductivity. b) Thermal conductivity of $BA_2MA_{n-1}Pb_nI_{3n+1}$ with respect to n. Semitransparent markers represent nominal fits of individual measurements whereas opaque markers represent the medians of fit distributions obtained *via* a MC estimation of uncertainty technique. Downward oriented triangles represent films with layers of parallel orientation (PO) with respect to the substrate while sideways oriented triangles represent films with layers of normal orientation (NO) with respect to the substrate. Upper and lower error bars represent the 90th and 10th quantiles of fit for each distribution. The gray area represents the range of thermal conductivities of $MAPbI_3$ reported in past research[91,101,134]. The period length of each perovskite is shown on the top horizontal axis.

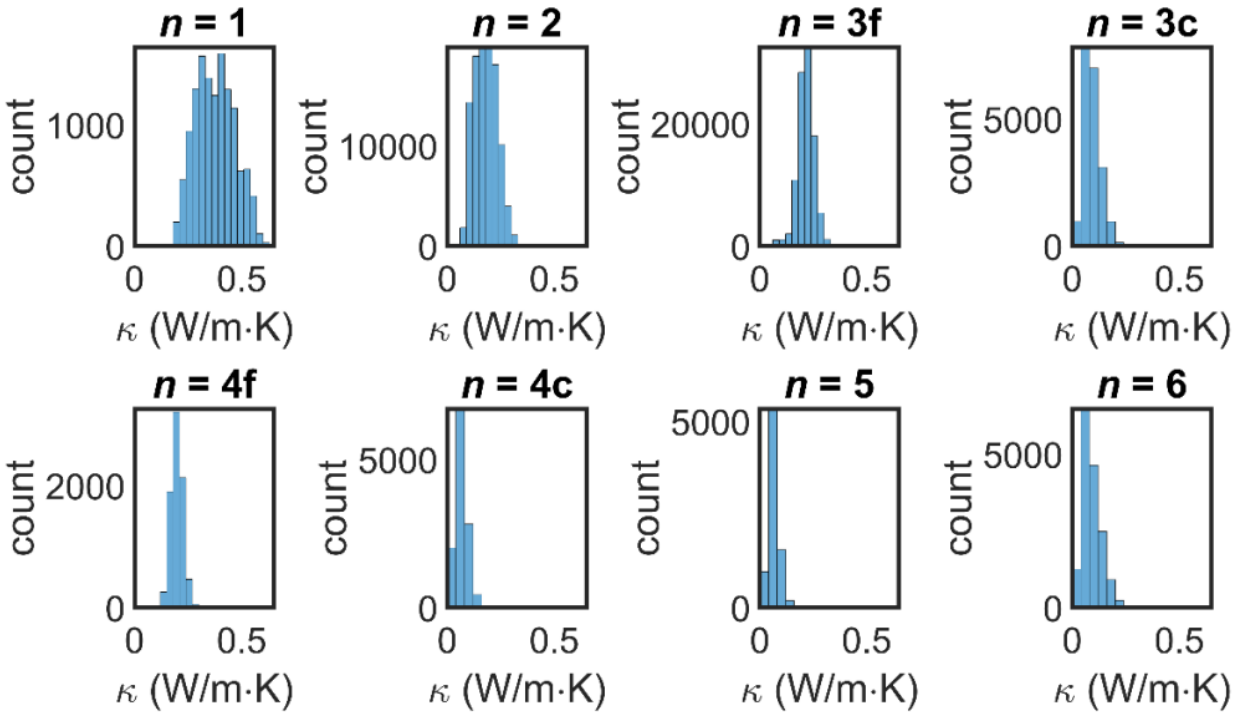

Figure 4.7. Histograms generated from the Monte Carlo (MC) estimation of uncertainty approach. Distributions are generally non-normal, so the median of each is generally a better descriptor of central tendency than the mean. Distributions with tighter spreads correspond to data points in Fig. 4.6b with smaller error bars. ‘f’ and ‘c’ denote distributions for films and crystals, respectively.

Laser power was controlled in the FDTR measurements so that laser-based heating was minimized without compromising signal strength. This type of heating is composed of steady state, or DC, heating created by both pump and probe beams as well as modulated, or AC, heating created only by the pump beam, as described in Eq. 1.4.8. We limited cumulative incident laser power to ~2.6 mW and ~0.5 mW for thin films and single crystals, respectively, and measured the absorbed power as the difference in power between the incident and reflected beams using a Thorlabs PM100D Digital Optical Power Meter. The absorbed pump and probe power were input to the heat diffusion model to calculate the maximum temperature rise, tabulated in Table 4.3 below.

n	type	Max Temperature Rise (K)	DC Component (K)	AC Component (K)
1	film	18.4	14.6	3.8
2		27.0	21.5	5.6
3		28.7	22.8	6
4		31.1	24.7	6.4
3	crystal	28.4	24.2	4.2
4		29.7	25.4	4.3
5		29.7	25.4	4.3
6		28.4	24.2	4.2

Table 4.3. The maximum temperature rise of each sample type is decomposed into a steady state (DC) and alternating (AC) component. Calculations were performed at a modulation frequency of 100 kHz, since AC heating-induced temperature fluctuations are largest at lower frequencies. DC heating induced temperature rise is frequency independent.

Our collaborators performed structural characterization measurements on the RP phase thin films to better understand the origins of the discrepancies in thermal conductivity, κ, seen in Fig. 4.6b between thin films and single crystals of $n = 3$ and 4. Atomic composition and grain formation of $n = 1 - 4$ thin films were assessed using grazing-incidence wide-angle X-ray scattering (GIWAXS) at Beamline 12-ID-B of the Advanced Photon Source at Argonne National Laboratory. This technique angles an X-ray laser beam toward the sample, almost to the point of total external reflection, that is reflected towards a nearby detector granting angstrom-level detail of atomic structure and orientation[109,135].

Data collected for $n = 1 - 4$ are shown in Fig. 4.8a-d, and schematic representations are presented in Fig. 4.8e-h. Data were fit using the LineFit toolbox and were plotted using the GIXSGUI program[136]. Data collected for $n = 1$ present peaks that indicate layer orientation that is

consistently parallel to the substrate. Since FDTR primarily probes thermal transport perpendicular to the sample surface, this result suggests that FDTR measurements are observations of cross-plane thermal conductivity, $\kappa_\perp$. Small peaks at low q may be representative of impurities in n = 1 thin films, perhaps a consequence of solvated phases formed during film creation[137,138]. Data collected for n = 2 reveal a bimodal distribution of grain orientations, at an approximately 1:2 ratio of grains with layers oriented normal and parallel to the substrate. n = 3 and 4 data display peaks consistent with layers oriented normal to the substrate. n = 4 peaks are broadened along the angular axis, χ, meaning that grains may be slightly angled from perfectly normal. In comparison to n = 1, n = 3 and 4 thin films will experience heat flow parallel to the layers during FDTR measurement, meaning that the fit thermal conductivity will describe in-layer thermal conductivity which we expect to resemble that of bulk $MAPbI_3$ ($\kappa = 0.34 - 0.50\ \mathrm{Wm^{-1}K^{-1}}$) due to phonon transport primarily along the inorganic perovskite layers. We therefore conclude that the higher thermal conductivities measured in n = 3 and 4 thin films relative to single crystals is a consequence of grain orientation rather than a physical difference in $\kappa_\perp$ between the two sample types.

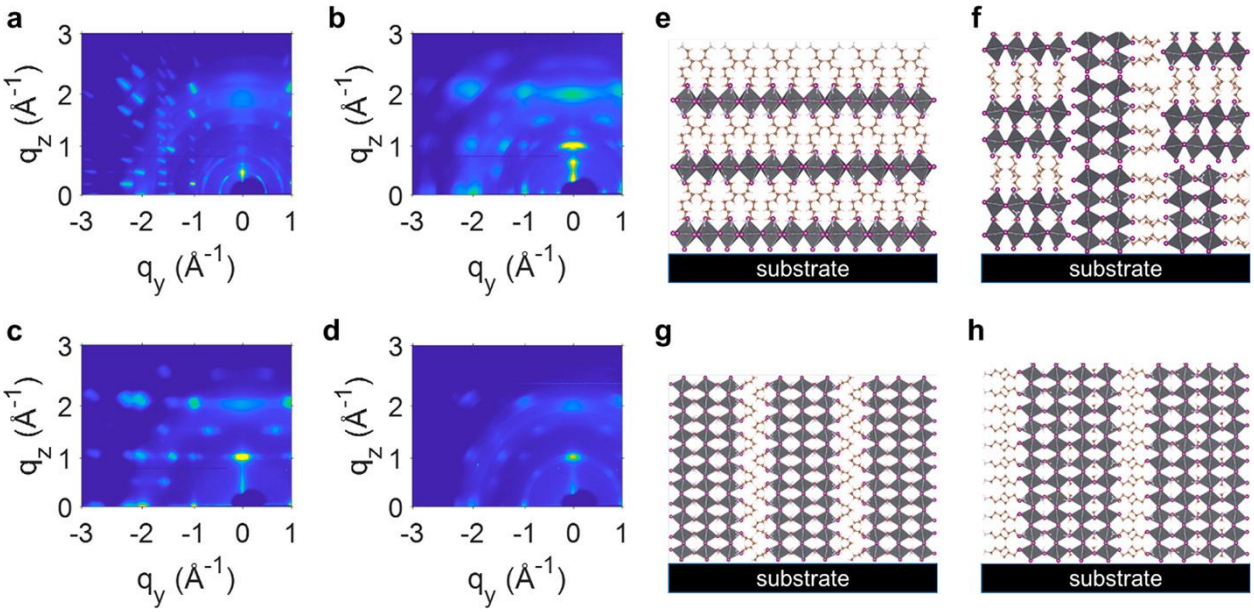

Figure 4.8. GIWAXS data, plotted using GIXSGUI, are shown in a – d for n = 1 – 4 thin films, and interpretive schematics are presented alongside them in e – h. The [0 1 0] crystal direction of n = 1 is directed perpendicular to the substrate, whereas it is parallel to the substrate in n = 3 and 4 thin films. n = 2 is bimodal and exhibits a 2:1 ratio of grains with the [0 1 0] direction oriented perpendicular and parallel to the substrate.

Our collaborators complimented GIWAXS measurements with powder X-ray diffraction (PXRD) performed on a D2 Phaser (Bruker) diffractometer, as shown in Fig. 4.9. Peaks for n = 1 are consistent with the cross-plane crystal directions, whereas peaks for n = 2 represent both cross- and in-plane crystal directions, as would be expected for a bimodal distribution. Measurements of n = 3 and 4 thin films reveal major peaks that correspond to the (2 0 2) crystal plane, which is perpendicular to the substrate, and minor ones that correspond to the (1 1 1) crystal plane, which is angled with respect to the substrate. The difference in amplitude of the peaks suggests that the majority of grains have layers oriented perpendicular to the substrate, while some rest at a slight angle.

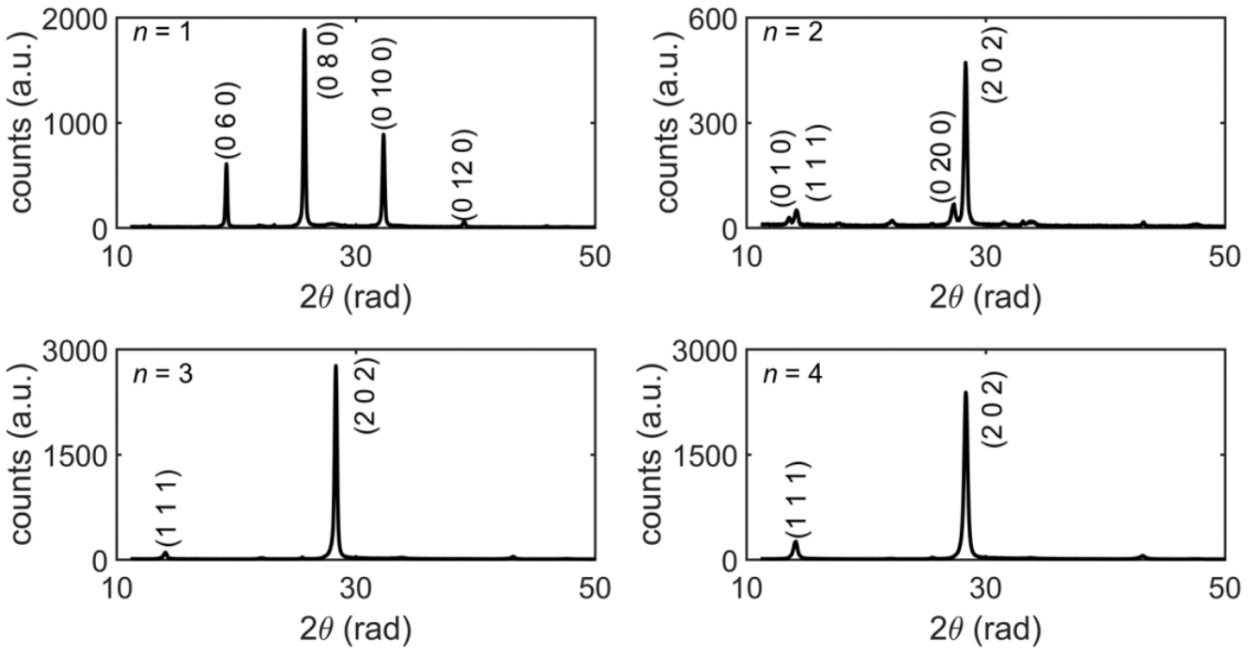

Figure 4.9. PXRD measurements of n = 1 – 4 thin films of $BA_2MA_{n-1}Pb_nI_{3n+1}$. Here, peaks in the data for n = 1 all represent planes parallel to the layers, indicating that the layers are parallel to the substrate. Peaks are bimodal for n = 2, and the major peaks of n = 3 and 4 represent crystal planes perpendicular to the layers, suggesting that layers are normal to the substrate.

Our FDTR measurements of thermal conductivity of n = 4 thin films are consistent with the value reported by Giri *et al.* due to orientational consistency between the two samples ($0.19 \pm 0.04/0.03$ *vs.* 0.17 ± 0.03 $Wm^{-1}K^{-1}$)[133]. However, we measure lower values of $\kappa_\perp$ in n = 4 single crystals since thermal transport induced by the pump laser in our technique is almost exclusively cross-layer. Moreover, our measurements of $\kappa_\perp$ of n = 1 are higher than those reported for thin films by Giri *et al.* (0.18 ± 0.04 $Wm^{-1}K^{-1}$)[133] and for single crystals by Rael *et al.* (0.125 ± 0.089 $Wm^{-1}K^{-1}$)[139]. We believe that the discrepancy between our measurements and the former study may arise from differences in sample preparation, particularly solvent choice and substrate

temperature management, which are understood to affect film morphology, homogeneity, and composition[120,130,138,140]. We hypothesize that the dissimilarity in our reported value with the latter study may be due to their increased laser heating (~14 K *vs.* ~30 K DC temperature increase) which they suggest may induce structural rearrangements.

The trend in similarly oriented RP phases shown in Fig. 4.6b (filled opaque data, $n = 1$ and 2 thin films and $n = 3 – 6$ single crystals) suggests that $\kappa_\perp$ initially decreases with increasing n (and consequently interface spacing), but plateaus at higher n. An entirely particle-like transport regime would require $\kappa_\perp$ to either increase or remain the same with increasing n, meaning that the observed result is likely a consequence of reduced contribution of coherent phonons to thermal conductivity with increasing layer spacing. Coherent phonons will always exist to some extent in superlattices and layered structures such as these RP phases, however their effect on thermal transport is minimal once layer spacing is increased sufficiently. We therefore hypothesize that a crossover point, similar to the one observed by Ravichandran *et al.*[123] may exist near the level-off in thermal conductivity that we observe.

We developed a reduced-order harmonic lattice dynamics model (chosen over molecular dynamics and first principles calculations due to its computational feasibility[141,142]) with a three-phonon phase space[143] to grain insight on the effects of group velocity of coherent phonons on $\kappa_\perp$ in $BA_2MA_{n-1}Pb_nI_{3n+1}$. Such an approach ignores high frequency incoherent phonons, however we do not expect these modes to contribute directly to thermal conductivity. Incoherent modes, however, affect scattering and are therefore needed for a fully quantitative model.

We grouped atoms into octahedron-like and BA-like beads to reduce computational complexity[144], as shown in Fig. 4.10, and invoke three spring constants (octahedron-octahedron, BA – BA, and BA – octahedron) to develop equations of motion to describe the system. The inter-

octahedron spring constant was fit from the experimental dispersion of $MAPbI_3$[145], while the other two were derived from experimental measurements of sound speed[146]. In this, we assumed that BA – BA and BA – octahedron spring constants are equal across all size phases. We find that the octahedron-octahedron spring constant, k_1, is 33.9 $\mathrm{Nm^{-1}}$, the octahedron – BA spring constant, k_2, is 3.6 $\mathrm{Nm^{-1}}$, and that the BA – BA spring constant, k_3, is 1.2 $\mathrm{Nm^{-1}}$.

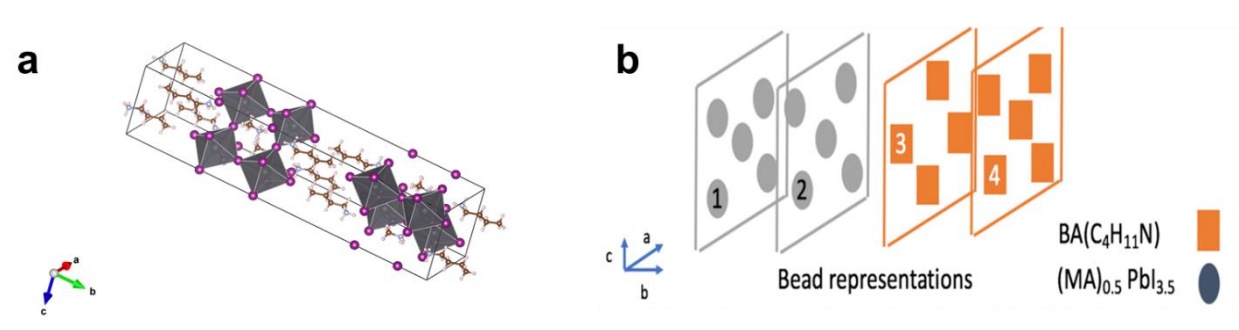

Figure 4.10. a) schematic representation of the n = 2 ($BA_2MAPb_2I_7$) unit cell, b) beads invoked in the reduced-order harmonic lattice calculations of n = 2.

The equation of motion for a bead, numerically labeled 0, is

$$\begin{aligned} F_x &= m_0 a_x \\ F_y &= m_0 a_y \\ F_z &= m_0 a_z \end{aligned} \qquad 4.2.4$$

where the acceleration term in any cartesian coordinate (denoted by $\mathcal{C}$) is

$$a_{\mathcal{C}} = m_0 \frac{d^2 u_0^{\mathcal{C}}}{d^2 t} \qquad 4.2.5$$

and $u_0^{\mathcal{C}}$ is the displacement of bead 0 from equilibrium. We defined the force along any coordinate as a function of the relative displacement of bead 0 along that coordinate direction:

$$F_{\mathcal{C}} = F_{\mathcal{C},rel.disp.along\ x-dir.} + F_{\mathcal{C},rel.disp.along\ y-dir.} + F_{\mathcal{C},rel.disp.along\ z-dir.} \qquad 4.2.6$$

Here, forces are broken down into the sum of forces caused by the bead's interactive neighbors (INs):

$$\begin{aligned} F_{\mathcal{C},rel.disp.along\ x-dir.} &= \sum_{i\in\{INs\}} k_{0,i}\alpha_{0,i}(u_i^x - u_0^x) \\ F_{\mathcal{C},rel.disp.along\ y-dir.} &= \sum_{i\in\{INs\}} k_{0,i}\beta_{0,i}(u_i^y - u_0^y) \\ F_{\mathcal{C},rel.disp.along\ z-dir.} &= \sum_{i\in\{INs\}} k_{0,i}\gamma_{0,i}(u_i^z - u_0^z) \end{aligned} \qquad 4.2.7$$

$k_{0,i}$ is the spring constant relating bead 0 and bead i, while $\alpha_{0,i}$, $\beta_{0,i}$, and $\gamma_{0,i}$ are coefficients that relate displacements and forces in a specific direction, and can be calculated by $\cos(\theta)\cos(\phi)$, where θ and ϕ are the angles between the relative displacement and spring, and force and spring, respectively.

Equations of motion can be reduced to

$$D\boldsymbol{U} = -\omega^2\boldsymbol{U} \qquad 4.2.8$$

where D is the dynamical matrix, ω is the phonon mode angular frequency, and $\boldsymbol{U}$ is the amplitude of the wave calculated by plugging bead displacement into an assumed plane wave solution:

$$\boldsymbol{u} = \boldsymbol{U}\exp[i(\boldsymbol{q}\mathfrak{C} - \omega t)] \qquad 4.2.9$$

where $\boldsymbol{q}$ is the wave vector, and $\mathfrak{C}$ is the bead's coordinate position. This approach allows us to solve for phonon frequencies according to wavevector as an eigenvalue problem.

Generally, Eq. 1.1.11 can be adapted to be written in terms of phonon lifetime rather than mean free path:

$$\kappa_{\perp} = \sum_{\beta} C_{V,\beta} v_{\perp,\beta}^2 \tau_{\beta} \qquad 4.2.10$$

where β denotes a particular phonon mode. The heat capacity contribution of a single mode was calculated as

$$C_{V,\beta} = \frac{(\hbar\omega)^2}{k_B T^2} \frac{\exp\left(\frac{\hbar\omega}{k_B T}\right)}{\left[\exp\left(\frac{\hbar\omega}{k_B T}\right) - 1\right]^2} \qquad 4.2.11$$

and the cross-layer phonon group velocity was determined using the corresponding component of the dispersion band:

$$v_{\perp,\beta} = \frac{\partial\omega}{\partial k_{\perp}} \qquad 4.2.12$$

The phonon dispersion relation derived from our reduced-order harmonic lattice dynamics calculations for n = 1, 3, and 6 are shown in Fig. 4.11a for the cross layer, or [0 1 0], crystal direction for $BA_2MA_{n-1}Pb_nI_{3n+1}$. A higher degree of band flattening at large wavevectors is seen as n increases, reducing cross-layer average phonon group velocity, particularly from n = 1 to n = 2 as shown in Fig. 4.11b. More bandgaps emerge as n increases as well, reducing the fraction of the total frequency range occupied by phonon modes. Such an effect indicates reduced phase space for phonon scattering that increases relaxation times and therefore thermal conductivity. However, the reduction in phase space caused by these bandgaps, as shown in Fig. 4.11c, is minor compared to the reduction in group velocity and 8% decrease in $C_{V,\beta}$ from n = 1 to 6, resulting in the decrease in $\kappa_\perp$ from n = 1 to 2 and flattening from n = 3 to 6.

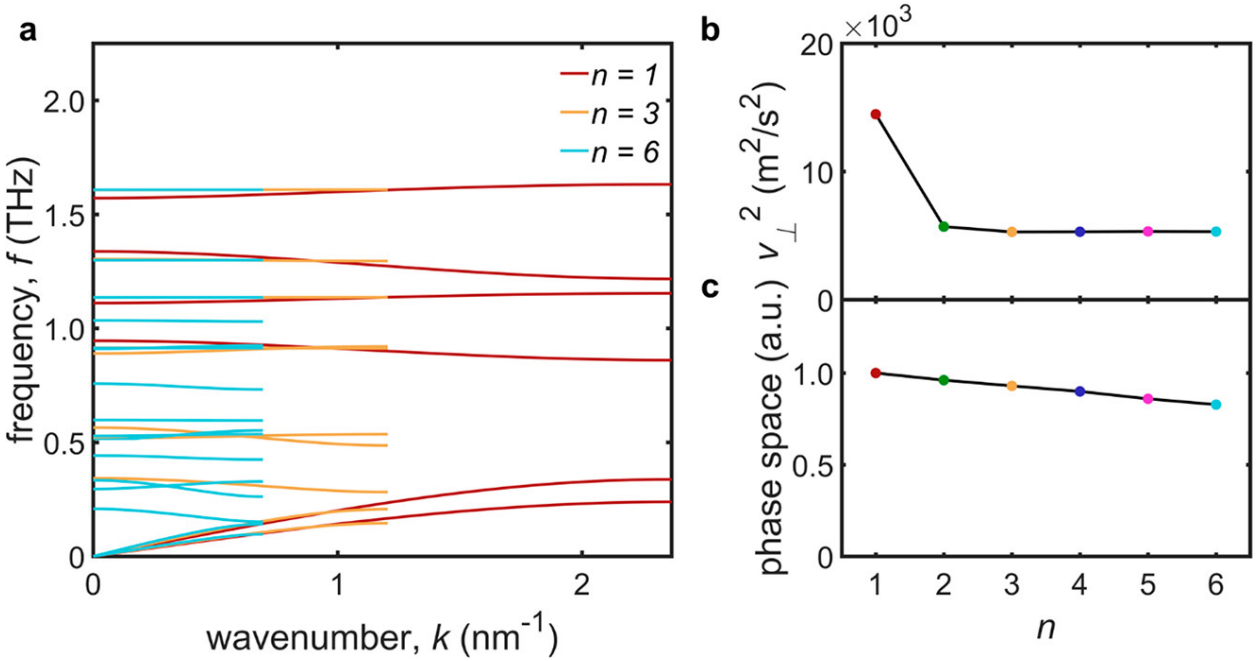

Figure 4.11. a) cross-layer phonon dispersion relation for n = 1, 3, and 6 $BA_2MA_{n-1}Pb_nI_{3n+1}$ RP phases, b) average cross-layer group velocity and c) normalized phase space for n = 1 – 6 RP phases.

The reduced-order harmonic lattice dynamics model can predict $\kappa_\perp$ in principle, however, average phonon lifetime, $\bar{\tau}$, for each RP phase is not known. Instead, we use our thermal conductivity data for similarly oriented RP phases (n = 1 and 2 thin films and n = 3 – 6 single crystals) in conjunction with the group velocity results of the model to fit to a single $\bar{\tau}$ for all n = 1 – 6 RP phases that minimizes mean squared error. We found that $\bar{\tau} = 100$ ps yields a model, shown in Fig. 4.6b, that agrees well with experimental data across all n. Relaxation times likely vary across orders of magnitude, but the close fit suggests that coherent phonon modes which contribute heavily to $\kappa_\perp$ have a narrow distribution. This relaxation time was converted to an average mean free path:

$$\bar{\Lambda}_\perp = \bar{\tau}\sqrt{\overline{v_\perp^2}} \qquad 4.2.13$$

which corresponds to ~ 7 nm for n = 6 and 12 nm for n = 1. These are larger to or similar to the period length, suggesting that coherent phonon modes play a larger role in lower n structures, and that they may still be significant in higher n RP phases.

In this study, we found that the cross layer thermal conductivity of $BA_2MA_{n-1}Pb_nI_{3n+1}$ RP phases decreases with increasing n. $\kappa_\perp$ decreases most significantly between n = 1 and 2, which we believe is due to a reduction in coherent phonon transport as interlayer spacing increases. Our FDTR measurements present ultralow thermal conductivities of n = 3 – 6 single crystals that rank among the lowest ever seen in fully dense solids. Our lattice dynamics calculations indicate that coherent phonon group velocity decreases with increasing n while average lifetimes may be more uniform. The results of our work suggest that these RP phases may be difficult to utilize in devices

due to their ultralow thermal conductivities which may respond poorly to thermal load. However, tunability in thermal transport through adjustment of inorganic layer thickness, *n*, along with improved stability over $MAPbI_3$, makes this class of perovskite appealing for multi-dimensional design in photovoltaic, optoelectronic, and thermoelectric applications.

4.2.1 Statement of Contribution

Alexander D. Christodoulides, Lingyun Dai, and Jonathan A. Malen: single crystal sample preparation and metal deposition, FDTR measurement of thermal conductivity.

Alexander D. Christodoulides and Jonathan A. Malen: MC estimation of uncertainty of FDTR data and thermally related analysis.

Peijun Guo, Richard D. Schaller, and Mercouri G. Kanatzidis: material synthesis and thin film sample preparation, PXRD.

Justin M. Hoffman, Xiaotong Li, Xiaobing Zuo, Daniel Rosenmann, and Alexandra Brumberg: GIWAXS measurements and analysis.

Lingyun Dai and Jonathan A. Malen: reduced-order harmonic lattice dynamics modeling of perovskites.

4.3 Two-Dimensional $MnCl_4$ Derivatives

Refrigeration is critically important in all facets of society. It is used for the preservation of food, medicine, and other perishable goods, and is needed for cooling electrical devices of all forms and sizes. A colossal 25 to 30 percent of all electricity is put towards refrigeration[147], and

unfortunately most of it is used to power vapor compression cycles (VPCs) which can be harmful to the environment due to the emission of chlorofluorocarbons (CFCs) and hydrochlorofluorocarbons (HCFCs)[148]. Efforts have therefore been aimed at phasing out VPCs where possible and replacing them with technologies reliant on solid-state caloric effects[149–151]. These alternative cooling methods are categorized by the applied external field: caloric effects caused by magnetic fields are termed magnetocaloric (MCE), those caused by electric fields are electrocaloric (ECE), and those caused by mechanical stress are mechanocaloric (this includes both elastocaloric (eCE) and barocaloric (BCE))[152].

Significant attention has been paid towards magnetocaloric materials and using them to potentially replace VPCs since the discovery of giant MCE in $Gd_2Si_2Ge_2$ at room temperature[153]. However, less time has been devoted to understanding the potential of mechanocaloric materials until the last decade which has seen them rival both MCE and ECE materials in performance[154]. One study found giant BCE effects in Ni-Mn-In magnetic shape-memory alloys of $24.4.\ \mathrm{Jkg^{-1}K^{-1}}$, which competes closely with reports of magnetic isothermal entropy change in MCE materials[155,156]. The relative ease of imposing mechanical stress (as opposed to very strong magnetic fields), combined with efficiency and eco-friendliness, makes mechanocaloric solids a material class of high priority to the renewable energy research community.

Layered perovskites, specifically $(C_nH_{2n+1}NH_3)_2MCl_4$ (where M = Mn, Cu, Hg, and Fe), have emerged as potential candidates for barocaloric solid state cooling. These two-dimensional perovskites, unlike the ones discussed in the previous section, are highly stable in oxygen-rich environments, and only begin to show thermal decomposition at and above 500 K. They are structurally similar, however, in that they are defined by alternating layers of perovskite octahedra and organic spacer molecules. The long alkylammonium chains are ionically bound at the A site

of the prototypical ABX_3 perovskite structure and are attracted to one another through weaker van der Waals bonds. Most notably, the chains undergo reversible solid-solid phase transitions in the near-ambient temperature range, while the inorganic cages are enthalpically inert[157,158]. These phase transitions are defined by high enthalpy and an iconic "chain-melting" process whereby the carbon backbone of the spacers transforms from a generally ordered zig-zagging pattern to a considerably more disordered, "liquid-like" configuration[159], as illustrated in Fig. 4.12. Characteristics of the transition (temperature, enthalpy, isothermal entropy and volume change, heat capacity behavior, etc.) are closely tied to the length of the alkylammonium chains[157].

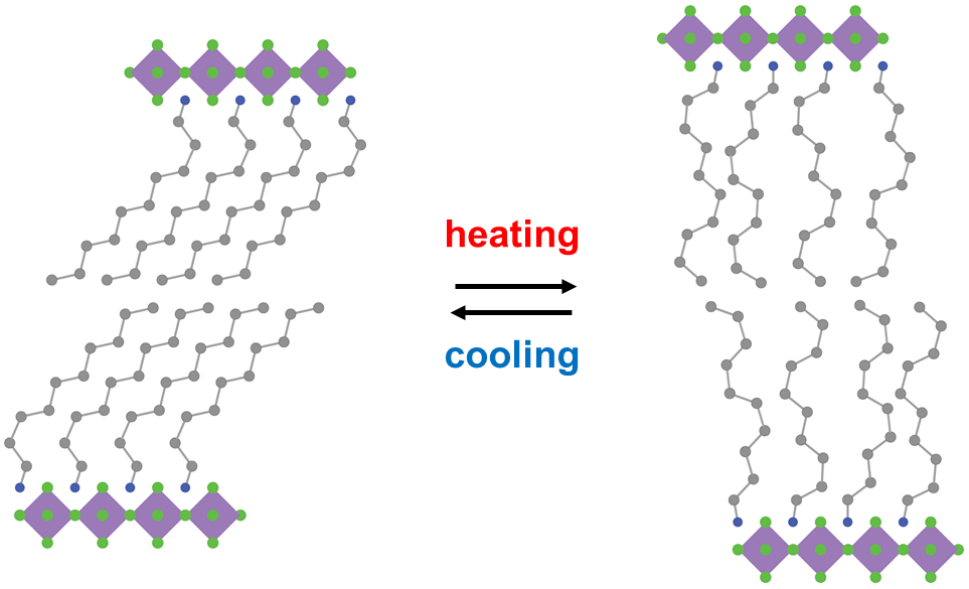

Figure 4.12. The first-order phase transition of $(C_nH_{2n+1}NH_3)_2MCl_4$ is marked by so-called melting, or disordering and conformational freedom, of alkylammonium chains as the material is heated.

The high reversibility, large entropy changes, sensitivity to hydrostatic pressure, and low hysteresis (1.5 K) associated with this order-disorder phase transition has naturally led to the discovery of colossal BCE in $(C_nH_{2n+1}NH_3)_2MCl_4$. Studies performed independently by Li *et al.*[160]

and Seo *et al.*[161] recently showed that these materials achieve high barocaloric coefficients resulting in large isothermal entropy changes when exposed to practically low hydrostatic pressures. The values they report are yet unrivaled and demonstrate the viability of BCE materials in replacing conventional refrigeration techniques such as VPCs in small devices.

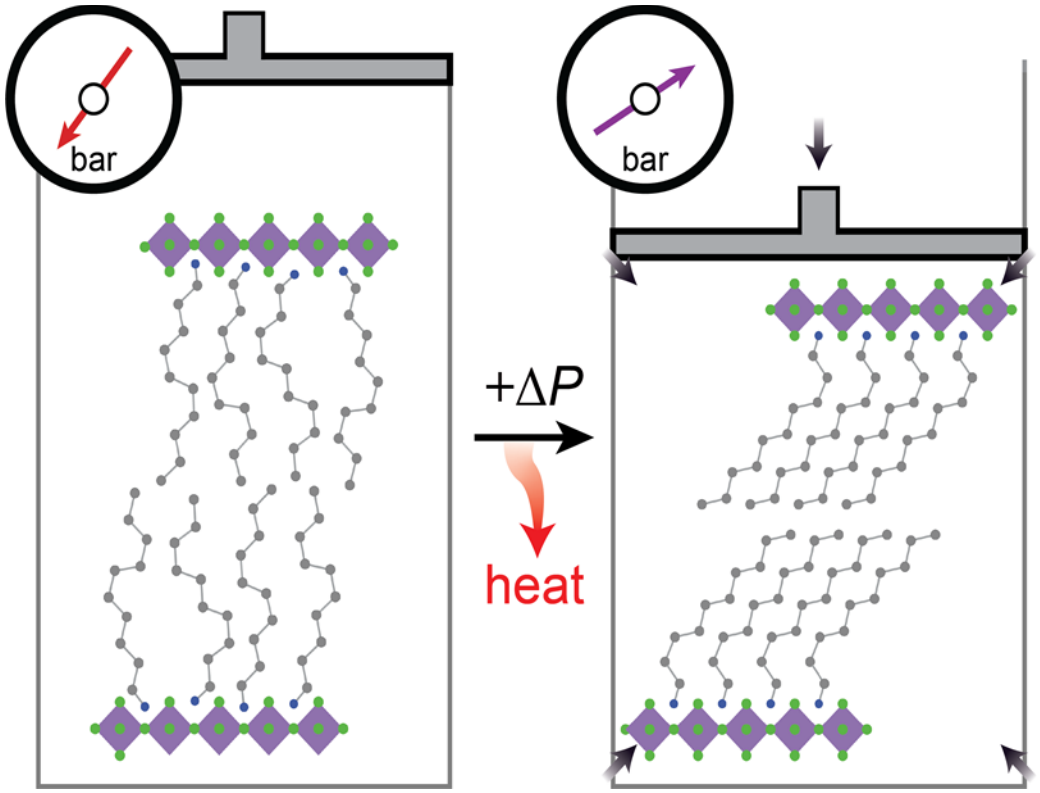

Figure 4.13. A theoretical BCE solid-state cooling device is shown here. The chain-melting process is highly reversible, and the entropy associated with the disorder-to-ordered transition can be used to remove heat from a source through the external application of hydrostatic pressure.

Successful barocaloric cooling relies on cyclically driving reversible phase transitions through thermodynamic processes that are designed to temporarily store waste heat in the solid-state material before transferring it to a heat sink. The functionality of this approach is dependent

on the barocaloric material's ability to exchange heat efficiently with both the heat source and sink, as well as its capacity to conduct heat internally and reach a uniform temperature for phase transition without local overheating. Designing for this requires knowledge of thermal conductivity, which is not yet understood in $(C_nH_{2n+1}NH_3)_2MCl_4$. It is expected that these perovskites will exhibit ultralow thermal conductivities similar to those reported in our study of $BA_2MA_{n-1}Pb_nI_{3n+1}$ RP phases. However, transport phenomena that dictate thermal conductivity, and the effects of chain-melting on thermal transport, are still unknown. In this study we seek to elucidate the underlying physics of cross-layer heat transfer in this class of perovskite by addressing what role, if any, chain-melting, interface chemistry, and bilayer composition/length play in dictating thermal conductivity.

We measured the thermal conductivities of $(C_nH_{2n+1}NH_3)_2MnCl_4$ for n = 10 and 12 (which we abbreviate as "C_{10}" and "C_{12}" respectively) as well as that of $(NH_3(CH_2)_4C_6H_5)_2MnCl_4$ (which we abbreviate as "C_4-phenyl), using FDTR. The first two sample types are characterized by alternating layers of manganese chloride perovskite octahedra and *n*-alyklammonium chains that are terminated at the perovskite by NH_3^+ molecules. They are distinguished from one another by the length of their carbon backbone: C_{12} contains two more carbons along the chain than C_{10} does. C_4-phenyl is similar to C_{10} and C_{12} in that it is also ionically bound to the perovskite via a NH_3^+ cation but differs in that the end at the organic-organic interface is a phenyl molecule. The phenyls are thermodynamically ordered such that in-layer carbon rings are orthogonally oriented to one another.

Samples were precipitated from solution by our collaborators at Harvard University. Examples of optical microscope and AFM images of single crystals and the corresponding chemical structure are shown in Fig. 4.14. As is the case with the RP phases in the previous section,

we expect that crystals grow such that the cross-layer crystal direction is uniformly oriented normal to the wafer. Crystals exhibit a high degree of topographical consistency and smoothness, which was measured *via* AFM, as shown in Fig. 4.15. C_{10} and C_{12} crystals have major lateral dimensions of ~50 μm, while C_4-phenyl samples are significantly smaller at ~10 μm. For this reason, we elected to use a higher magnification lens (50x *vs.* 20x) during FDTR measurements of C_4-phenyl samples to reduce the spot size needed for data collection.

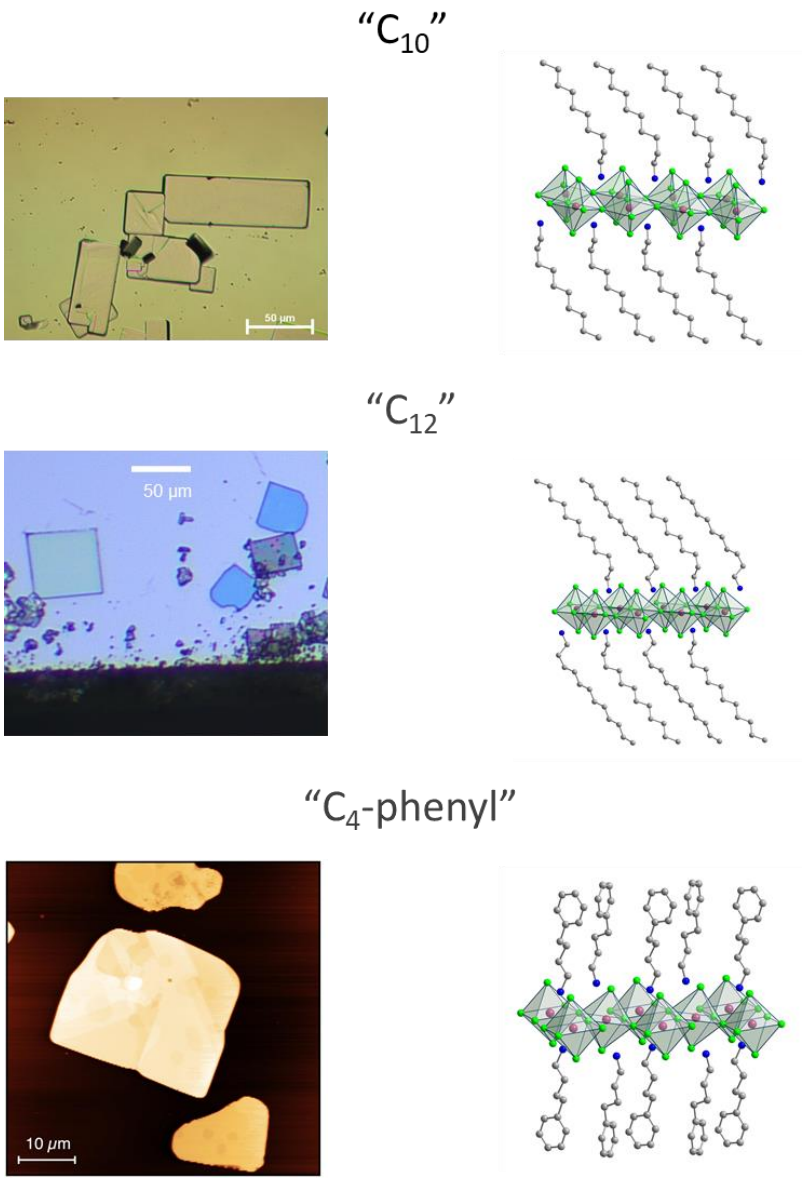

Figure 4.14. Microscope images (top, middle left) of single crystals of C_{10} and C_{12}, and an AFM topographical map of C_4-phenyl (bottom, left) are shown, as well as visualizations of the chemical structure of the bilayer for the corresponding crystal.

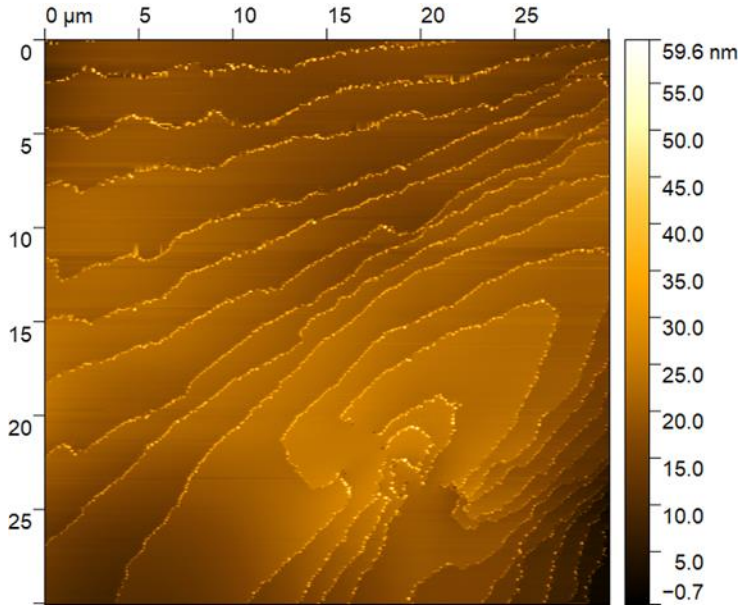

Figure 4.15. AFM data collected from a C_{10} crystal. The colormap represents changes in height recorded by the probe tip. The color uniformity of the crystal region suggests a low RMS roughness of 4.96 nm.

Differential scanning calorimetry (DSC) was used to identify the temperature at which the chain-melting phase transition occurs in C_{10}, C_{12}, and C_4-phenyl perovskites, as well as to measure heat capacity as a function of temperature. Heating and cooling cycles are shown in Fig. 4.16, where exothermic processes constitute positive heat flow. The phase transition in C_{10} resides closest to ambient temperature among the three sample types with an onset at ~37 °C. The extension of the carbon backbone of the alkylammonium chain increases the temperature of transition to ~56 °C in C_{12}. This result indicates that the chains are thermodynamically stabilized

by their increased length, and that greater activation energy is needed to initialize disorder. The phase transition of the C_4-phenyl perovskite is similarly high at ~67 °C. Slight hysteresis is observable between heating and cooling cycles for all three sample types that represents minor energy loss when cycled[162]. Additionally, a minor peak is present at 60 °C in C_{12} and 82 °C in C_4-phenyl. These peaks represent the onset of additional disorder in the carbon-carbon bonds even after the chain melting occurs. This is understood in C_{12} to be a result of additional gauche-to-trans conformational changes[163], while it is believed that phenyl rotation or twisting may occur in C_4-phenyl, as has been previously reported in related structures[164]. Heat capacity is extracted from the heat flow data, resulting in room temperature values of 1.73, 1.73, and 1.53 $kJm^{-3}K^{-1}$ for C_{10}, C_{12}, and C_4-phenyl respectively.

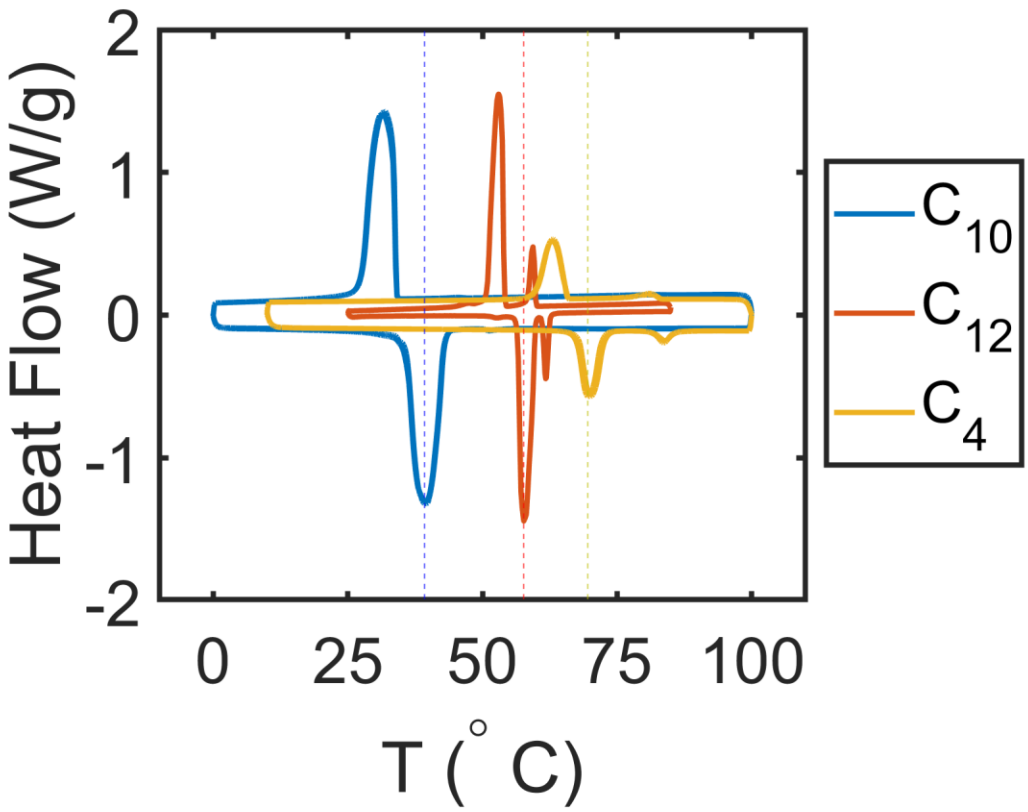

Figure 4.16. Heat flow measured during DSC measurement of C_{10}, C_{12}, and C_4-phenyl single crystals. Exothermic heat flow is positive, so heating and cooling profiles are represented by the bottom and top trends, respectively. Vertical dashed lines represent exothermic peaks of each transition. The reduced area associated with the peak of C_4-phenyl indicates its reduced heat capacity relative to C_{10} and C_{12}.

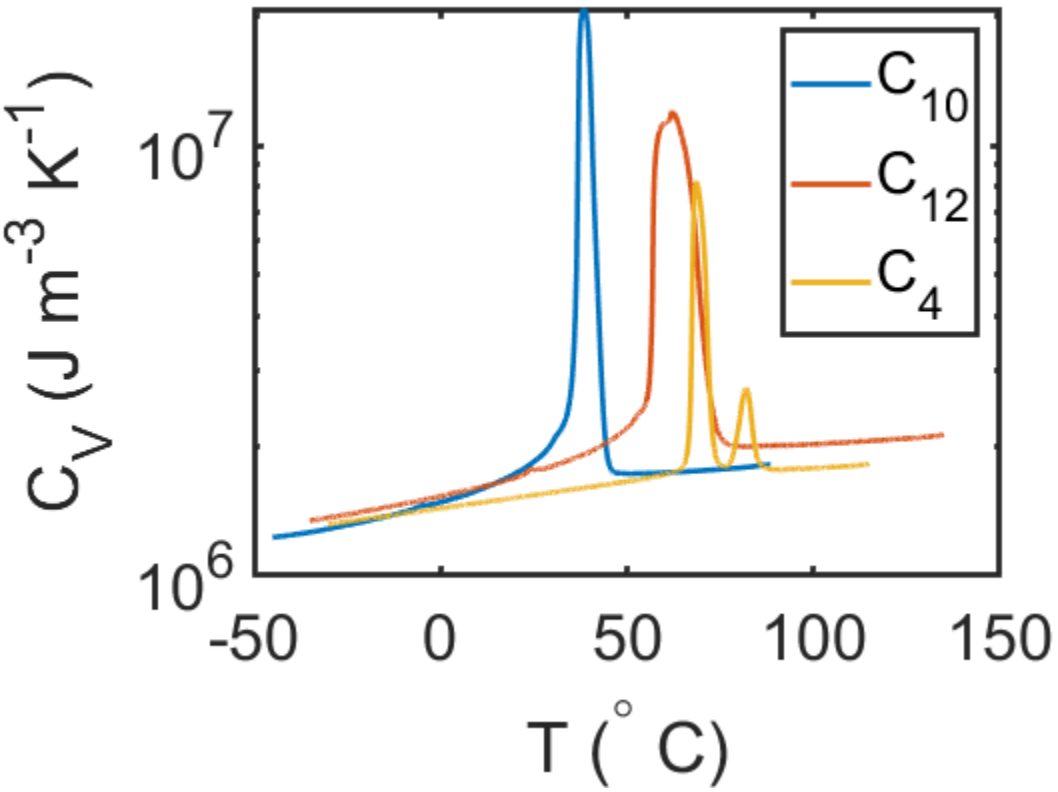

Figure 4.17. Baseline volumetric heat capacity information gathered through DSC measurements. Large peaks in the data represent the chain-melting transition. Consistent with the heat flow diagrams, C_{10} has the lowest transition temperature, followed by C_{12}, and finally C_4-phenyl.

The phase transitions of all three sample types are close to room temperature, so special consideration was made to limit laser power during thermal conductivity measurements to ensure

that measurements were made for both ordered and disordered states. We model both steady state (DC) and transient (AC) heating according to Eq. 1.4.8, where temperature rise is calculated iteratively to account for changes in heat capacity, density, and thickness (due to thermal expansion, particularly across the phase transition), according to the flow chart in Fig. 4.18. Solution convergence is set to a temperature difference of 0.1 K between iterations.

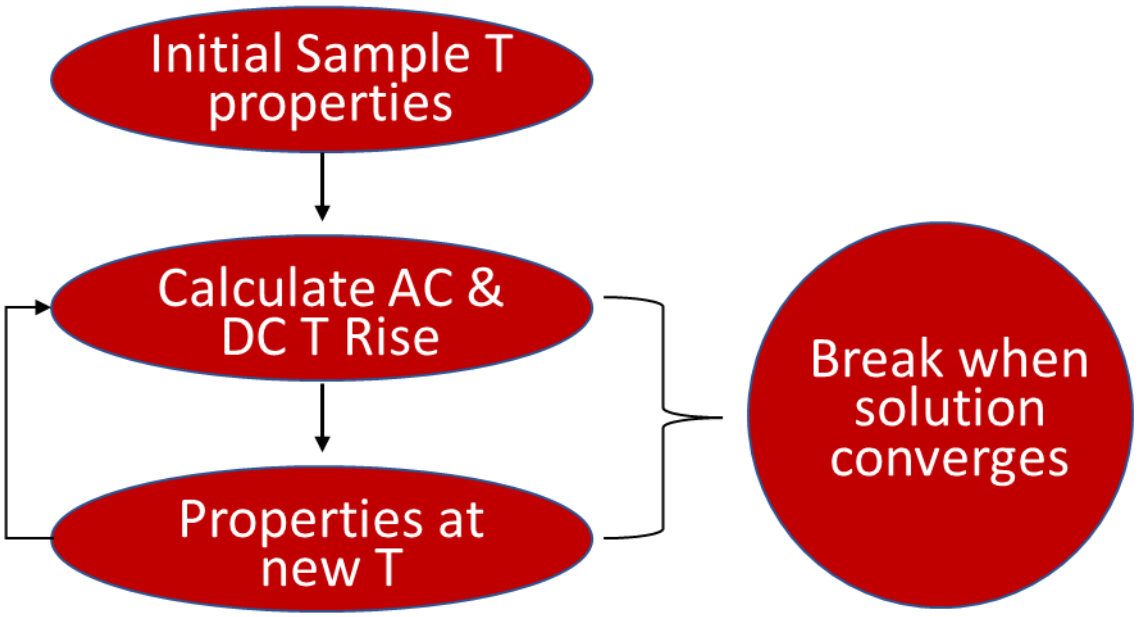

Figure 4.18. Flow chart illustrating the laser heating algorithm used to calculate sample temperature rise due to laser heating. Temperature increase is calculated for the minimum and maximum modulation frequency of the pump laser since AC heating is maximized at lower frequencies.

We placed samples in an Oxford Instruments MicrostatHe cryostat in order to perform measurements below and above room temperature. Samples were brought to higher temperatures using the resistance heater built into the cryostat. Care was taken to limit heating to below 1

°C/min. For cooling, the cryostat was evacuated to below 10^{-4} bar using a Pfeiffer HiCube 80 Eco Pump to minimize the risk of condensation formation or convective heat transfer. Liquid nitrogen was poured into the cryostat systematically to either reduce or maintain the temperature of the sample.

Preliminary thermal conductivity (κ) data for C_{10}, C_{12}, and C_4-phenyl gathered through FDTR is presented in Fig. 4.19. Only C_{10} was measured below room temperature since its phase transition temperature is closest to room temperature and could therefore be approached by laser heating alone. As expected, thermal conductivities are ultralow, and consistent with those reported for other two-dimensional perovskites[15,133,139]. The data suggests that the thermal conductivities of these perovskites are a weak function of temperature. Moreover, evidence of the chain-melting phase transition is remarkably absent in κ. This result indicates that cross-layer thermal transport is minimally affected by the disorder of the organic sections brought on by chain-melting, and that the ultralow thermal conductivity that we observe may be due to thermal bottlenecking elsewhere.

It is unlikely superlattice-like coherent phonons play a significant role in the thermal transport that we observe here. Were that the case, κ would decrease significantly across the phase transition, as chain-melting would likely destroy any periodicity that existed in the ordered phase that permitted coherent phonons to propagate. Instead, considering the length of the alternating organic (21.4, 25.3, and 18.9 Å in C_{10}, C_{12}, and C_4-phenyl respectively) and inorganic sections (5 Å in all perovskites), it is more realistic that short-range interatomic vibrations carry most of the heat within either layer, and that long-range modes are hindered by interfacial scattering or imperfect periodicity. Phenomena such as octahedral tilting (which occurs within the full range of temperature in Fig. 4.19) and chain-melting (which occurs at and beyond the phase transitions indicated in Fig. 4.16) may introduce randomness in the periodicity of the layers that could inhibit

coherent modes. Moreover, organic section thickness is larger than those of the RP perovskites of the previous section, (19 – 25 Å *vs.* 7 – 14 Å), which results in reduced interface densities. Finally, inorganic sections are composed of $MnCl_4$ rather than PbI_4 (as in n = 1 RP perovskites[15]) and they therefore may interact differently with the adjoining organic molecules, further complicating the cross-layer contributions of coherent phonon modes.

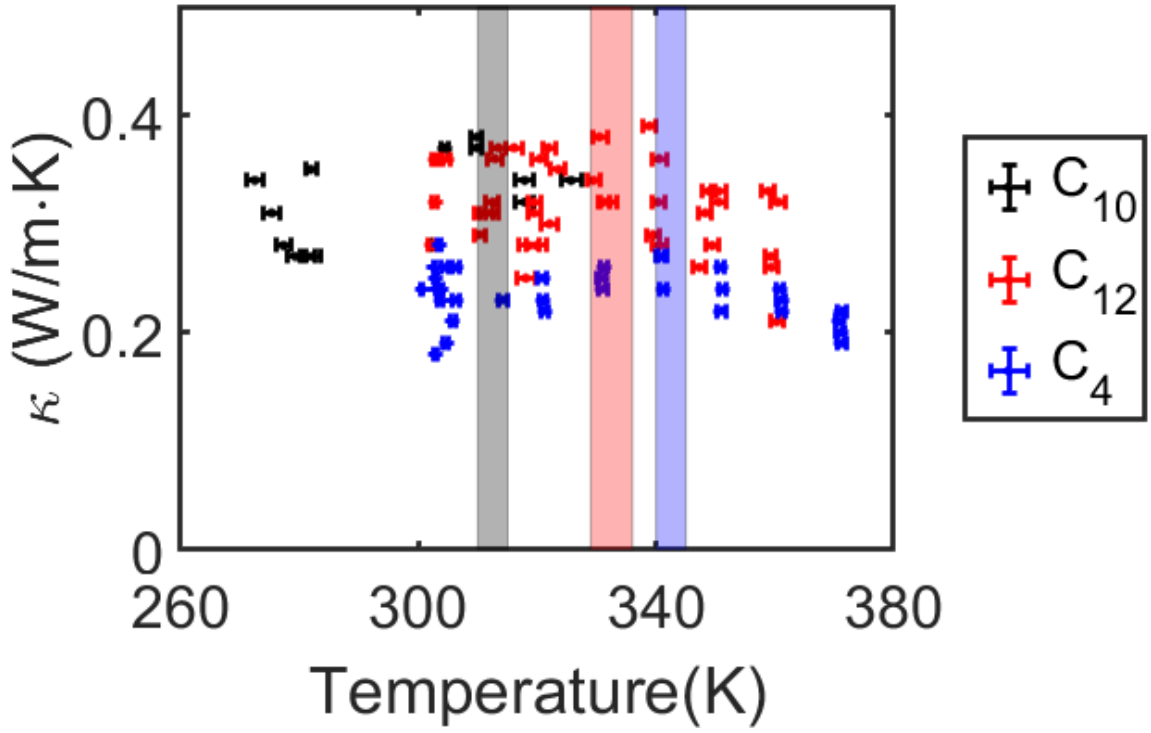

Figure 4.19. Thermal conductivity, κ, of C_{10}, C_{12}, and C_4-phenyl perovskites as a function of temperature. The shaded regions correspond to the expected chain-melting phase transition temperature of the respective sample type. Horizontal error bars represent the bottommost and uppermost temperatures experienced by the sample during measurement, since AC heating is dependent on the pump modulation frequency.

It is possible that heat flow is hindered by bonding chemistry at the inorganic-organic interface or lack thereof at the organic-organic interface. C_4-phenyl samples exhibit generally reduced κ relative to C_{10} and C_{12} samples. Since all three samples are terminated by NH_3^+ cations, we hypothesize that the organic-organic interface, which is characterized by orthogonally oriented phenyls, serves as a more significant center for phonon scattering than the than the alkylammonium chains. This theory is potentially contrasted, however, by preliminary nanoindentation data which reveals that C_4-phenyl perovskites exhibit higher Young's modulus than both C_{10} and C_{12}. Young's modulus is directly correlated to the low frequency limit of phonon group velocity (sound speed), and therefore is often used in conjunction with the phonon gas model in Eq. 1.1.11 to predict thermal conductivity. One might therefore expect higher thermal conductivities in materials with higher Young's moduli. While these results require further refinement, they may suggest that sound speed is decoupled from thermal conductivity, and that high frequency interatomic vibrations (which are poorly represented by sound speed) carry significant amounts of heat in the cross-layer direction. Alternatively, it is possible that phonon mean free path or lifetime may more immediately influence thermal conductivity than group velocity.

We developed a binning algorithm and applied it to the C_{12} data to assess whether they could be grouped within temperature ranges as statistically distinct groups. This algorithm defines six bins of variable size and location and quantifies the mean-squared error (MSE) within each bin to determine the combination of bin sizes and border locations that minimize the total error. The result is shown in Fig. 4.20a and indicates that all data belongs to the same group, meaning that no temperature dependent trend is observed. The algorithm is repeated by quantifying mean-squared displacement (MSD) rather than error in order to require the formation of six bins. However, the bin averages of κ are nearly identical, corroborating the result of the first calculation.

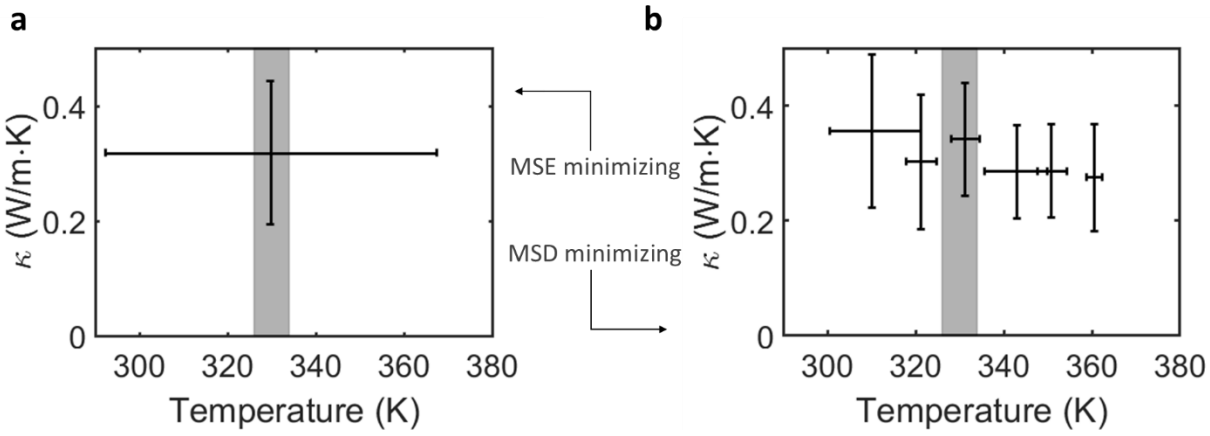

Figure 4.20. C_{12} data is binned by determining the bin size and location combination that minimizes the a) MSE and b) MSD of thermal conductivity of all bins when summed together. The result in both cases does not suggest a temperature dependent κ. The shaded gray region represents the temperature range of the chain-melting phase transition. Error bars represent 2σ of each bin's thermal conductivity and temperature range.

4.3.1 Future Work

We intend to continue this study to further our understanding of thermal transport in this important class of two-dimensional perovskite. Our collaborators have developed a new bilayer similar to C_4-phenyl but with a fluorine in the fourth position of the phenyl ring. This bilayer, 4-fluorobenzylamine (which we abbreviate "FBA") will presumably exhibit organic-organic interfacial properties that are unique (since bilayers will not be bound together by van der Waals forces as is the case in C_{10}, C_{12}, and C_4-phenyl) and will help us to distinguish the effect, if any, this interface has on thermal transport in these two-dimensional materials. In the future we also propose to measure thermal conductivity of Dion-Jacobson $MnCl_4$ perovskites which have organic

layers defined by a singular long diamene chain. We aim to understand how removing the organic-organic interface completely may impact cross-layer thermal conductivity. Finally, we resolve to investigate how varying the B site, which is currently occupied by Mn, affects thermal conductivity. This molecule is highly tunable, and can be replaced with Cu, Hg, and Fe[157,159]. We hope to isolate the heat transfer implications of the organic-inorganic interface through these measurements to hopefully modify thermal transport properties.

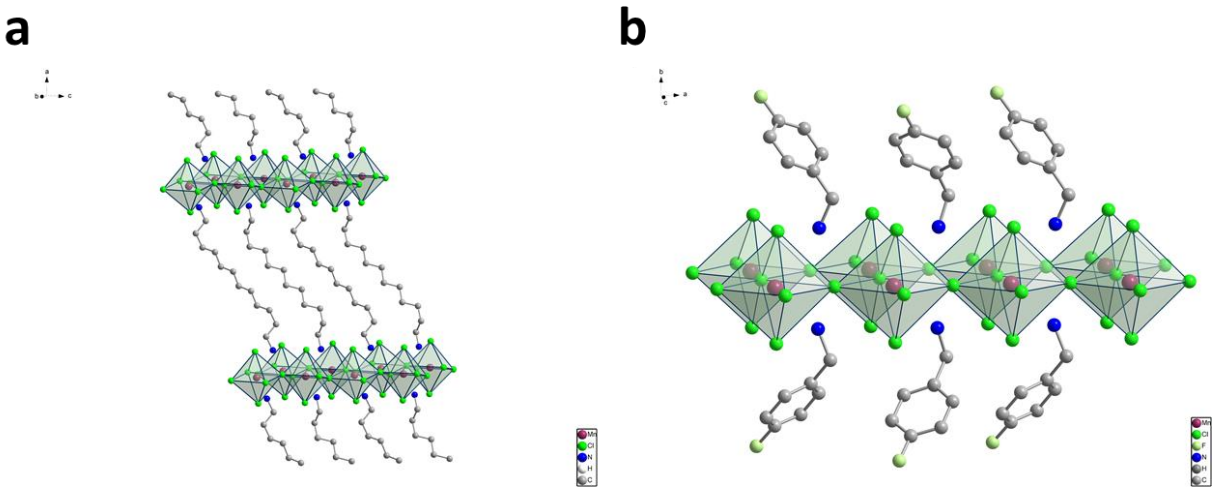

Figure 4.21. Crystallographic visualizations of $MnCl_4$-based two-dimensional perovskites with a) a single diamene chain in the bilayer (Dion-Jacobson structure) and b) 4-fluorobenzylamine in the bilayer.

Our collaborators have previously attempted nanoindentation to measure the Young's moduli of the perovskites but have had difficulty obtaining promising results due to experimental complications. Young's modulus is typically derived from the unloading curve of the nanoindentation since it is not associated with sample compression and deformity. Such an approach is made difficult here because samples commonly fracture or experience lateral shearing,

which prevents accurate measurement of the unloading process. Consequently, loading curves have been used to determine Young's modulus. We believe that AFM measurement may be more reliable, and our collaborators are therefore preparing samples for mechanical measurements *via* this technique instead.

Our results warrant thermal modeling to interpret the experimental data. The organic sections are reminiscent of polymers, and so the chain-melting may be well described by thermal modeling of similar systems such as single polyethylene chains[163], aligned polymers (either due to stress or curing)[165] or self-assembled monolayers (SAMs)[32]. At first glance, the length-invariant[166,167] but binding strength dependent[168] thermal interface conductance of many SAM structures appears to be similar to the bilayer invariant κ we observe. We therefore intend to investigate different models that may be capable of incapsulating the effects of chain alignment and interfacial bonding chemistry, one such example being the Cahill-Pohl minimum thermal conductivity model for disordered crystals[72] or the Simkin-Mahan model of minimum thermal conductivity in superlattices[169]. We may also attempt to model phonon dynamics through reduced-order harmonic lattice dynamics, similar to those used for layered perovskites in the past[15,146]. However, such an approach may be unlikely to yield additional information considering that no signatures of coherent or otherwise low-frequency phonon transport exist in the FDTR data.

4.3.2 Statement of Contribution

Alexander D. Christodoulides and Jonathan A. Malen: FDTR measurement of thermal conductivity and related analysis.

Rahil Ukani, Ryan McGillicuddy, and Jarad Mason: material synthesis, sample preparation, AFM characterization, DSC data collection, and nanoindentation.

5 Summary and Outlook

This document highlights several studies that investigate thermal transport phenomena in superstructured semiconducting materials. These sorts of materials are of increasing importance in science and engineering due the unique properties they exhibit that have not been observed in simpler semiconducting materials or basic metals. We classify the three material classes discussed herein (superatoms, nanocrystals, and two-dimensional perovskites) as superstructures as they are all characterized by nanoscale periodicity that exceeds the atomic scale. This periodicity gives rise to novel transport phenomena and tunable properties that may be functionalized in future technology.

Superatoms are atomically precise clusters of atoms that are intermediate in size and behave collectively as one would expect of a large singular atomic unit. Metal-chalcogenide – fullerene superatomic crystals (SACs), or structures defined by alternating units of metal-chalcogenide clusters and C_{60} or C_{70} cages stabilized and organized by organic capping ligands, have been investigated for their valuable properties such as redox activity, large magnetic moment, and luminescence[12].

Importantly, certain SACs, such as $Co_6Se_8(PEt_3)_6(C_{60})_2$, experience an ordered-to-disordered phase transition that enables the fullerene cages to rotate freely and initialize an amorphous-like thermal transport regime[14]. We therefore used frequency-domain thermoreflectance (FDTR) to investigate whether a similar SAC, $Co_6Te_8(PEt_3)_6(C_{70})_2$, would exhibit similar thermal transport switching behavior. Unlike the SACs characterized by spherical fullerene cages, [CoTe][C_{70}] contains oblong carbon cages (similar in shape to a rugby ball) and has two temperature-distinct phase transitions. Both monomeric (C_{70}^-) and dimeric (C_{140}^{2-})

fullerenes are locked in place in the low-temperature phase (Phase A) but begin to freely rotate along their long axis in the intermediate temperature phase (Phase B). Thermal conductivity is crystal-like in the low temperature phase and decreases with increasing temperature but becomes temperature-independent and amorphous-like in the intermediate temperature due to the increased scattering of phonons resulting from fullerene rotation. Dimeric fullerenes are separated in the high temperature phase (Phase C) as a result of homolytic cleavage which delocalizes electrons at the intersection of the two C_{70} molecules. This phenomenon creates a low-energy optical bandgap and greatly increases electrical conductivity and magnetic susceptibility[35]. This work demonstrates that ordered-to-disordered transitions are possible in many different SAC systems, and that they can result in significant thermal, magnetic, and optical property changes. The expansiveness of property tunability makes SAC materials valuable in highly dynamic applications that require high performance in a variety of operating conditions.

Electrostatic interactions between superatom clusters can be frustrated through careful solution processing to inhibit the formation of a crystalline structure. These materials, known as amorphous superatomic thin films, are highly tunable like the SACs but also exhibit unique properties well suited for thermoelectric (TE) applications. Our collaborators created films containing a cobalt-chalcogenide cluster, $Co_6Te_8(PPr_3)_6$ (abbreviated [Co]), and PCBM ($C_{72}H_{14}O_2$) which were made amorphous by the weak electrostatic interactions of the *n*-propylphosphine capping ligands. We measured thermal conductivity using FDTR and found that it is not a strong function of the molar ratio of [Co] to [PCBM]. However, electrical conductivity appears to be maximized at a molar ratio of 1:5 and exhibits a volcano-like trend. Our collaborators measured Seebeck coefficient and thermoelectric figure of merit (ZT) and found that these films show lower performance compared to other room-temperature TE materials[7]. However, their

tunability, which has not been realized in TE materials like bismuth chalcogenides, opens pathways for the development of new amorphous cluster-based solids that may exhibit enhanced multifunctional properties.

Colloidal nanocrystals (NCs) are similar to SACs in that they are inorganic clusters of particles stabilized into a solid (commonly referred to as a NC solid) by organic ligands that extend from the cluster surfaces. These materials garner attention for their excellent electronic[45–47], photovoltaic[48,49], thermoelectric[50], and optoelectronic[45–47,51] properties. Their solution processability and tunability make them attractive candidates for telecommunication technology and other next-generation devices.

NC solids have extremely low thermal conductivities, which is simultaneously advantageous in TE devices and disadvantageous in other applications. Our collaborators therefore created PbS nanocrystal superlattices (NCSLs) that differ from typical nanocrystal films (NCFs) by the long-range order of nanocrystals. Our FDTR measurements reveal that thermal conductivities of the NCSLs are strongly related to core diameter while those of NCFs are not. Our nanoindentation measurements provide similar data for Young's moduli, however the correlated change in sound speed is not sufficient to fully encompass the vast enlargement of thermal conductivity that we observe in NCSLs as core diameter is increased. An effective medium approximation (EMA)[64] shows that the thermal conductivity of NCSLs is strongly bound to that of the oleic acid matrix, and that the matrix thermal conductivity increases as core-diameter increases due to increased ligand alignment, order, and interdigitation. The matrix thermal conductivities of NCFs follow a minimum thermal conductivity model[69–72], whereas those of the NCLS do not, meaning that thermal transport in the NCF matrix is dominated by amorphous, incoherent phonon modes.

Perovskite materials have been studied in recent decades for their excellent performance in photovoltaic devices owing to properties such as solution processability[77], defect tolerance[78–80], carrier lifetime[78,79,81,82], optical bandgap[83], and absorption coefficient[84]. In particular, lead halide hybrid organic-inorganic perovskites (HOIPs) have achieved unrivaled power conversion efficiencies (PCEs) in relatively little time[84,87,89]. However, these materials are often unstable and have been demonstrated to degrade due to the presence of oxygen[108], moisture[108–110], light[109,111,112], and from elevated temperature[109–112]. Two-dimensional, layered perovskites have been developed in an effort to stabilize the perovskite structure with organic interlayer ligands while retaining the attractive properties that make them so popular.

We investigated thermal transport in a two-dimensional perovskite family, $BA_2MA_{n-1}Pb_nI_{3n+1}$, where n represents the number of perovskite octahedra in the cross-layer direction within each inorganic layer. We found that cross-layer thermal conductivity decreases with increasing layer thickness. The particle-like picture of phonon transport suggests that the opposite trend should occur since interfaces should scatter phonons and limit heat transfer. This result therefore indicates that coherent phonon modes, or those that are created by the secondary periodicity of the lattice, may be responsible for enhanced thermal conductivity in low n structures. Our reduced-order harmonic lattice dynamics calculations reveal that average cross-layer phonon group velocity decreases dramatically at low n, consistent with the trend we observe in cross-layer thermal conductivity. The similarity between the two corroborates the hypothesis that coherent phonons carry significant amounts of heat in low n structures. A singular average phonon lifetime is used to relate thermal conductivity data to the model, and the close fit could indicate that coherent phonons have similar lifetimes in these two-dimensional perovskites regardless of inorganic layer thickness. While the decreased thermal conductivities relative to $MAPbI_3$ make this class of

perovskite more susceptible to overheating, the improved stability and other possible property enhancements may make them useful in photovoltaic, optoelectronic, and thermoelectric devices.

A class of $MnCl_4$-based two dimensional perovskites, $(C_nH_{2n+1}NH_3)_2MCl_4$ (where M = Mn, Cu, Hg, and Fe), have been observed to exhibit a colossal barocaloric effect (BCE)[160,161], which makes them possible candidates for solid-state cooling devices. These materials undergo a "chain-melting" process whereby the bilayers become disordered. The enthalpy and change in entropy associated with this phase transition, along with hydrostatic pressure sensitivity and minimal hysteresis makes them potentially viable BCE materials. We measure the thermal conductivities of $(C_nH_{2n+1}NH_3)_2MnCl_4$ for n = 10 and 12 (which we abbreviate as "C_{10}" and "C_{12}" respectively) as well as that of $(NH_3(CH_2)_4C_6H_5)_2MnCl_4$ (which we abbreviate as "C_4-phenyl"), using FDTR. We find no evidence of the chain-melting phase transition in the thermal conductivity data of C_{10}, C_{12}, or C_4-phenyl, and find that thermal conductivity appears to be a weak function of temperature. Preliminary nanoindentation data suggests that C_4-phenyl, the material with the lowest measured thermal conductivity, holds the highest Young's modulus. The decoupled nature of the mechanical and thermal measurements may suggest that short-range interatomic vibrations are the dominant heat carriers in these materials. The results thus far indicate ultralow thermal conductivities, which may make using these perovskites in BCE cooling devices challenging due to local overheating and general heat flow concerns.

The studies discussed in the previous chapters may be used in future work to multiple ends. The thermal conductivity and other data we provide may be of practical benefit to engineering groups that aim to use these materials to develop novel technology. The superatomic structures, nanocrystals, and perovskites all present ultralow thermal conductivities that will pose a challenge in the design of devices that cannot utilize high temperature gradients. However, these works

demonstrate the high tunability of all three types of superstructures and may therefore provide insight for future work to exploit this tunability towards higher thermal conductivity or other material characteristic enhancements.

Significant attention has been paid to the thermal transport phenomena and fundamental physics that underlie experimental and modeling results. Ordered-to-disordered phase transitions, and coherent phonon transport have been invoked to understand trends in thermal transport behavior in SACs and perovskites, while the dynamics of short-range interatomic vibrations have been explored to understand heat flow in NC solids and amorphous superatomic thin films. Models such as EMAs and lattice dynamics were employed to elucidate certain transport phenomena unique to the materials under consideration. However, an overarching material characteristic has not been established to connect the thermal conductivity behaviors seen in all types of superstructures. This is an arduous endeavor as superstructured materials are typically described by parameters specific to the dimensionality of their periodicity. For example, while interface density or period length is a convenient metric for unit cell size in two-dimensional materials, average cluster diameter and spacing is more meaningful in systems with three-dimensional periodicity such as nanocrystal solids and superatomic crystals.

We therefore attempt to correlate more general properties, namely density and heat capacity, to thermal conductivity of superstructures. The room temperature thermal conductivity of semiconducting materials can be expressed according to kinetic theory, as shown in Eq. 1.1.11. The volumetric heat capacity, C_V, can be rewritten according to the Dulong-Petit limit of the Debye model established in Eq. 1.1.9:

$$C_V \sim 3Nk_B \tag{5.1}$$

Here, N represents the number density of vibrational units in the unit cell (sometimes molecules are considered to be a single unit if interatomic vibrations are not expected to contribute significantly to heat capacity). This can be rewritten in terms of density, ρ, molar mass, M, and Avocado's number, N_A,:

$$C_V \sim 3\frac{\rho N_A}{M} k_B \qquad 5.2$$

The kinetic theory approximation of thermal conductivity can finally be rewritten in terms of atomic density:

$$k \sim \frac{\rho N_A}{M} k_B \bar{v} \bar{\Lambda} \qquad 5.3$$

The superstructured materials discussed in previous chapters are described by complex and large unit cells, so M represents the total molar mass of the unit cell as a sum of its constituent molecules. Naturally, we expect that there may be some correlation between density and thermal conductivity ($k \propto \rho$). However, we find no evidence of a relationship between density and thermal conductivity, as shown in Fig. 5.1a, or between volumetric heat capacity and thermal conductivity, as shown in Fig. 5.1b. This may suggest that enhancements to thermal conductivity produced by increased density are offset by limited mean free path or group velocity of phonons, perhaps a consequence of increased localized scattering events.

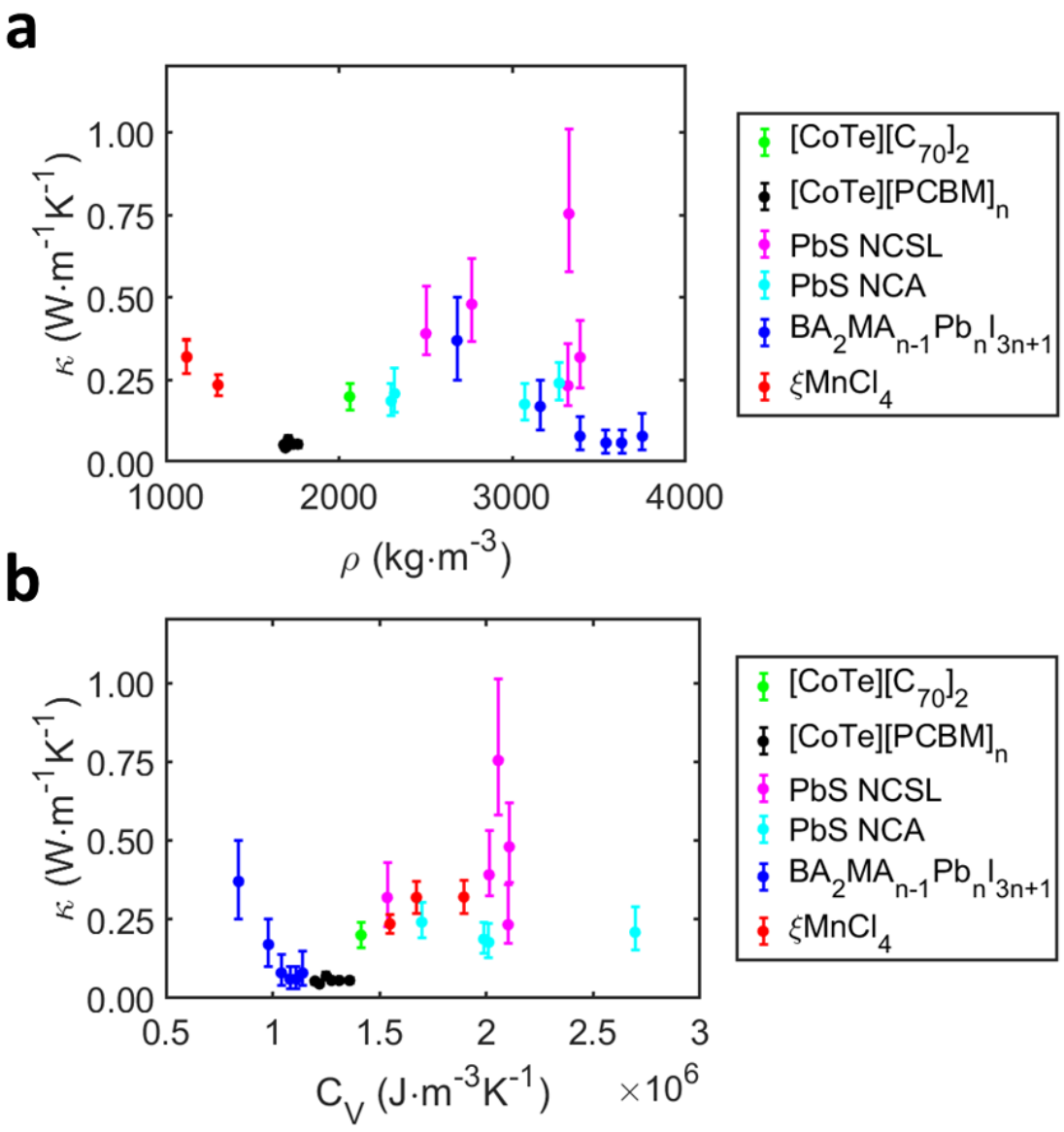

Figure 5.1. Room temperature thermal conductivities of superstructured semiconductors are plotted against a) density and b) heat capacity to determine if either property is strongly correlated to κ. The data does not indicate any clear association to density or heat capacity.

We believe that the information detailed in the previous chapters may be helpful to groups who aim to investigate transport phenomena in similarly superstructured or otherwise complex materials. These studies may be considered as part of a greater body of work devoted to

characterizing multifunctionality, tunability, and novelty of superstructures, and it is our hope that these findings will advance the field of nanoscale thermal transport, and that they might aid in the discovery of advanced energy materials that will be used in next-generation technology.

6 References

1. Kittel C. Introduction to Solid State Physics, 8th edition, Berkeley. *John Wiley & Sons, New York* (1996).

2. Chen, G. PhD. Nanoscale energy transport and conversion : a parallel treatment of electrons, molecules, phonons, and photons. 531 (2005).

3. Luo, T. & Chen, G. Nanoscale heat transfer – from computation to experiment. *Physical Chemistry Chemical Physics* **15**, 3389–3412 (2013).

4. Pop, E., Mann, D., Wang, Q., Goodson, K. & Dai, H. Thermal Conductance of an Individual Single-Wall Carbon Nanotube above Room Temperature. **22**, 47 (2022).

5. Balandin, A. A. *et al.* Superior Thermal Conductivity of Single-Layer Graphene. doi:10.1021/nl0731872.

6. Chiritescu, C. *et al.* Ultralow Thermal Conductivity in Disordered, Layered WSe_2 Crystals. *Science* **315**, 351–353 (2007).

7. Yang, J. *et al.* Solution-Processable Superatomic Thin-Films. *J. Am. Chem. Soc.* **141**, 10967–10971 (2019).

8. Duda, J. C., Hopkins, P. E., Shen, Y. & Gupta, M. C. Exceptionally Low Thermal Conductivities of Films of the Fullerene Derivative PCBM. *Phys. Rev. Lett.* **110**, 015902 (2013).

9. Wang, X., Liman, C. D., Treat, N. D., Chabinyc, M. L. & Cahill, D. G. Ultralow Thermal Conductivity of Fullerene Derivatives. *Phys. Rev. B: Condens. Matter Mater. Phys.* **88**, 075310 (2013).

10. Moore, A. L. & Shi, L. Emerging challenges and materials for thermal management of electronics. *Materials Today* **17**, 163–174 (2014).

11. Feng, T., Lindsay, L. & Ruan, X. Four-phonon scattering significantly reduces intrinsic thermal conductivity of solids. *Physical Review B* **96**, 161201 (2017).

12. Doud, E. A. *et al.* Superatoms in materials science. *Nature Reviews Materials* vol. 5 371–387 (2020).

13. Haque, M. A., Kee, S., Villalva, D. R., Ong, W. L. & Baran, D. Halide Perovskites: Thermal Transport and Prospects for Thermoelectricity. *Advanced Science* **7**, 1903389 (2020).

14. Ong, W. L. *et al.* Orientational Order Controls Crystalline and Amorphous Thermal Transport in Superatomic Crystals. *Nat. Mater.* **16**, 83–88 (2017).

15. Christodoulides, A. D. *et al.* Signatures of Coherent Phonon Transport in Ultralow Thermal Conductivity Two-Dimensional Ruddlesden−Popper Phase Perovskites. (2021) doi:10.1021/acsnano.0c03595.

16. Ong, W. L., Rupich, S. M., Talapin, D. v., McGaughey, A. J. H. & Malen, J. A. Surface chemistry mediates thermal transport in three-dimensional nanocrystal arrays. *Nature Materials* **12**, 410–415 (2013).

17. Cheng, Z. *et al.* Tunable Thermal Energy Transport across Diamond Membranes and Diamond-Si Interfaces by Nanoscale Graphoepitaxy. *ACS Applied Materials and Interfaces* **11**, 18517–18527 (2019).

18. Chen, K. *et al.* Ultrahigh thermal conductivity in isotope-enriched cubic boron nitride. *Science* **367**, 555–559 (2020).

19. Epstein, J., Ong, W. L., Bettinger, C. J. & Malen, J. A. Temperature Dependent Thermal Conductivity and Thermal Interface Resistance of Pentacene Thin Films with Varying Morphology. *ACS Applied Materials and Interfaces* **8**, 19168–19174 (2016).

20. Cahill, D. G. Analysis of Heat Flow in Layered Structures for Time-Domain Thermoreflectance. *Rev. Sci. Instrum.* **75**, 5119–5122 (2004).

21. Hamby, D. M. A review of techniques for parameter sensitivity analysis of environmental models. *Environmental Monitoring and Assessment* **32**, 135–154 (1994).

22. Jiang, P., Qian, X. & Yang, R. Time-domain thermoreflectance (TDTR) measurements of anisotropic thermal conductivity using a variable spot size approach. *Review of Scientific Instruments* **88**, 074901 (2017).

23. Hopkins, P. E. *et al.* Criteria for cross-plane dominated thermal transport in multilayer thin film systems during modulated laser heating. *Journal of Heat Transfer* **132**, 1–10 (2010).

24. Zhu, J. *et al.* Ultrafast thermoreflectance techniques for measuring thermal conductivity and interface thermal conductance of thin films. *Journal of Applied Physics* **108**, 094315 (2010).

25. Liu, J. *et al.* Simultaneous measurement of thermal conductivity and heat capacity of bulk and thin film materials using frequency-dependent transient thermoreflectance method. *Review of Scientific Instruments* **84**, 034902 (2013).

26. Wang, X., Jeong, M., McGaughey, A. J. H. & Malen, J. A. Reducing the uncertainty caused by the laser spot radius in frequency-domain thermoreflectance measurements of thermal properties. *Review of Scientific Instruments* **93**, 023001 (2022).

27. Collier, C. P., Vossmeyer, T. & Heath, J. R. NANOCRYSTAL SUPERLATTICES. *http://dx.doi.org/10.1146/annurev.physchem.49.1.371* **49**, 371–404 (2003).

28. Auyeung, E. *et al.* Synthetically programmable nanoparticle superlattices using a hollow three-dimensional spacer approach. *Nature Nanotechnology 2011 7:1* **7**, 24–28 (2011).

29. Shevchenko, E. v., Talapin, D. v., Kotov, N. A., O'Brien, S. & Murray, C. B. Structural diversity in binary nanoparticle superlattices. *Nature* **439**, 55–59 (2006).

30. Roy, X. *et al.* Nanoscale atoms in solid-state chemistry. *Science* **341**, 157–160 (2013).

31. Ong, W. L., Majumdar, S., Malen, J. A. & McGaughey, A. J. H. Coupling of organic and inorganic vibrational states and their thermal transport in nanocrystal arrays. *Journal of Physical Chemistry C* **118**, 7288–7295 (2014).

32. Majumdar, S. *et al.* Vibrational mismatch of metal leads controls thermal conductance of self-assembled monolayer junctions. *Nano Letters* **15**, 2985–2991 (2015).

33. Lu, J. P., Li, X. P. & Martin, R. M. Ground state and phase transitions in solid C60. *Physical review letters* **68**, 1551–1554 (1992).

34. David, W. I. F. *et al.* Crystal structure and bonding of ordered C60. *Nature 1991 353:6340* **353**, 147–149 (1991).

35. O'Brien, E. S. *et al.* Spontaneous Electronic Band Formation and Switchable Behaviors in a Phase-Rich Superatomic Crystal. *J. Am. Chem. Soc.* **140**, 15601–15605 (2018).

36. X-Ray Diffraction (XRD) - XOS. https://www.xos.com/XRD.

37. Konarev, D. v. *et al.* Formation of single-bonded (C60-)2 and (C70-)2 dimers in crystalline ionic complexes of fullerenes. *Journal of the American Chemical Society* **125**, 10074–10083 (2003).

38. Malen, J. A. *et al.* Optical Measurement of Thermal Conductivity Using Fiber Aligned Frequency Domain Thermoreflectance. *J. Heat Transfer* **133**, 081601 (2011).

39. Turkiewicz, A. *et al.* Assembling hierarchical cluster solids with atomic precision. *Journal of the American Chemical Society* **136**, 15873–15876 (2014).

40. Paternò, G. *et al.* Micro-focused X-ray diffraction characterization of high-quality [6,6]-phenyl-C61-butyric acid methyl ester single crystals without solvent impurities. *Journal of Materials Chemistry C* **1**, 5619–5623 (2013).

41. Pei, Y. *et al.* Convergence of electronic bands for high performance bulk thermoelectrics. *Nature 2011 473:7345* **473**, 66–69 (2011).

42. Pei, Y., Lalonde, A., Iwanaga, S. & Snyder, G. J. High thermoelectric figure of merit in heavy hole dominated PbTe. *Energy & Environmental Science* **4**, 2085–2089 (2011).

43. Heremans, J. P. *et al.* Enhancement of thermoelectric efficiency in PbTe by distortion of the electronic density of states. *Science* **321**, 554–557 (2008).

44. Chung, D. Y. *et al.* Complex bismuth chalcogenides as thermoelectrics. *International Conference on Thermoelectrics, ICT, Proceedings* 459–462 (1997) doi:10.1109/ICT.1997.667185.

45. Oh, S. J. *et al.* Engineering charge injection and charge transport for high performance PbSe nanocrystal thin film devices and circuits. *Nano Letters* **14**, 6210–6216 (2014).

46. Lee, J. S., Kovalenko, M. v., Huang, J., Chung, D. S. & Talapin, D. v. Band-like transport, high electron mobility and high photoconductivity in all-inorganic nanocrystal arrays. *Nature Nanotechnology 2011 6:6* **6**, 348–352 (2011).

47. Talapin, D. v., Lee, J. S., Kovalenko, M. v. & Shevchenko, E. v. Prospects of Colloidal Nanocrystals for Electronic and Optoelectronic Applications. *Chemical Reviews* **110**, 389–458 (2009).

48. Yuan, M., Liu, M. & Sargent, E. H. Colloidal quantum dot solids for solution-processed solar cells. *Nature Energy 2016 1:3* **1**, 1–9 (2016).

49. Tang, J. *et al.* Colloidal-quantum-dot photovoltaics using atomic-ligand passivation. *Nature Materials 2011 10:10* **10**, 765–771 (2011).

50. Wang, R. Y. *et al.* Enhanced thermopower in PbSe nanocrystal quantum dot superlattices. *Nano Letters* **8**, 2283–2288 (2008).

51. Saran, R. & Curry, R. J. Lead sulphide nanocrystal photodetector technologies. *Nature Photonics 2016 10:2* **10**, 81–92 (2016).

52. Franchi, S., Trevisi, G., Seravalli, L. & Frigeri, P. Quantum dot nanostructures and molecular beam epitaxy. *Progress in Crystal Growth and Characterization of Materials* **47**, 166–195 (2003).

53. Wang, Z. *et al.* Ligand Crosslinking Boosts Thermal Transport in Colloidal Nanocrystal Solids. *Angewandte Chemie* **132**, 9643–9650 (2020).

54. Liu, M., Ma, Y. & Wang, R. Y. Modifying Thermal Transport in Colloidal Nanocrystal Solids with Surface Chemistry. *ACS Nano* **9**, 12079–12087 (2015).

55. Henry, A. THERMAL TRANSPORT IN POLYMERS. *Annual Review of Heat Transfer* **17**, 485–520 (2014).

56. Shen, S., Henry, A., Tong, J., Zheng, R. & Chen, G. Polyethylene nanofibres with very high thermal conductivities. *Nature Nanotechnology 2010 5:4* **5**, 251–255 (2010).

57. Luo, T. & Lloyd, J. R. Non-equilibrium molecular dynamics study of thermal energy transport in Au–SAM–Au junctions. *International Journal of Heat and Mass Transfer* **53**, 1–11 (2010).

58. O'Brien, P. J. *et al.* Bonding-induced thermal conductance enhancement at inorganic heterointerfaces using nanomolecular monolayers. *Nature Materials 2012 12:2* **12**, 118–122 (2012).

59. Lee, B. *et al.* Comparison of structural behavior of nanocrystals in randomly packed films and long-range ordered superlattices by time-resolved small angle X-ray scattering. *Journal of the American Chemical Society* **131**, 16386–16388 (2009).

60. Bougher, T. L. *et al.* Thermal Boundary Resistance in GaN Films Measured by Time Domain Thermoreflectance with Robust Monte Carlo Uncertainty Estimation. *Nanoscale Microscale Thermophys. Eng.* **20**, 22–32 (2016).

61. Saha, D. *et al.* Enhancing Thermal Interface Conductance to Graphene Using Ni–Pd Alloy Contacts. *ACS Appl. Mater. Interfaces* **12**, 59 (2020).

62. He, J. *et al.* Fabrication and Mechanical Properties of Large-Scale Freestanding Nanoparticle Membranes. *Small* **6**, 1449–1456 (2010).

63. Hostetler, M. J., Stokes, J. J. & Murray, R. W. Infrared Spectroscopy of Three-Dimensional Self-Assembled Monolayers: N-Alkanethiolate Monolayers on Gold Cluster Compounds. *Langmuir* **12**, 3604–3612 (1996).

64. Hasselman, D. P. H. & Johnson, L. F. Effective Thermal Conductivity of Composites with Interfacial Thermal Barrier Resistance. *Journal of Composite Materials* **21**, 508–515 (1987).

65. Pei, Y. L. & Liu, Y. Electrical and thermal transport properties of Pb-based chalcogenides: PbTe, PbSe, and PbS. *Journal of Alloys and Compounds* **514**, 40–44 (2012).

66. Wang, H., Wang, J., Cao, X. & Snyder, G. J. Thermoelectric alloys between PbSe and PbS with effective thermal conductivity reduction and high figure of merit. *Journal of Materials Chemistry A* **2**, 3169–3174 (2014).

67. Wang, H., Schechtel, E., Pei, Y. & Snyder, G. J. High thermoelectric effi ciency of n-type PbS. *Advanced Energy Materials* **3**, 488–495 (2013).

68. Baroncini, C., di Filippo, P., Latini, G. & Pacetti, M. Organic liquid thermal conductivity: A prediction method in the reduced temperature range 0.3 to 0.8. *International Journal of Thermophysics* **2**, 21–38 (1981).

69. Xie, X. *et al.* Thermal Conductivity, Heat Capacity, and Elastic Constants of Water-Soluble Polymers and Polymer Blends. *Macromolecules* **49**, 972–978 (2016).

70. Xie, X. *et al.* High and low thermal conductivity of amorphous macromolecules. *Physical Review B* **95**, 035406 (2017).

71. Cahill, D. G. & Pohl, R. O. Heat flow and lattice vibrations in glasses. *Solid State Communications* **70**, 927–930 (1989).

72. Cahill, D. G., Watson, S. K. & Pohl, R. O. Lower limit to the thermal conductivity of disordered crystals. *Physical Review B* **46**, 6131 (1992).

73. Harikrishnan, S. & Kalaiselvam, S. Preparation and thermal characteristics of CuO–oleic acid nanofluids as a phase change material. *Thermochimica Acta* **533**, 46–55 (2012).

74. Affdl, J. C. H. & Kardos, J. L. The Halpin-Tsai equations: A review. *Polymer Engineering & Science* **16**, 344–352 (1976).

75. Podsiadlo, P. *et al.* The role of order, nanocrystal size, and capping ligands in the collective mechanical response of three-dimensional nanocrystal solids. *Journal of the American Chemical Society* **132**, 8953–8960 (2010).

76. Artini, C. Crystal chemistry, stability and properties of interlanthanide perovskites: A review. *Journal of the European Ceramic Society* **37**, 427–440 (2017).

77. Burschka, J. *et al.* Sequential Deposition as a Route to High-Performance Perovskite-Sensitized Solar Cells. *Nature* **499**, 316–319 (2013).

78. Veldhuis, S. A. *et al.* Perovskite Materials for Light-Emitting Diodes and Lasers. *Adv. Mater.* **28**, 6804–6834 (2016).

79. Du, M. H. Efficient Carrier Transport in Halide Perovskites: Theoretical Perspectives. *J. Mater. Chem. A* **2**, 9091–9098 (2014).

80. Miyata, K. *et al.* Large Polarons in Lead Halide Perovskites. *Sci. Adv.* **3**, 1701217 (2017).

81. Herz, L. M. Charge-Carrier Dynamics in Organic-Inorganic Metal Halide Perovskites. *Annu. Rev. Phys. Chem.* **67**, 65–89 (2016).

82. Milot, R. L. *et al.* Charge-Carrier Dynamics in 2D Hybrid Metal-Halide Perovskites. *Nano Lett.* **16**, 7001–7007 (2016).

83. Leguy, A. M. A. *et al.* Experimental and Theoretical Optical Properties of Methylammonium Lead Halide Perovskites. *Nanoscale* **8**, 6317–6327 (2016).

84. Brenner, T. M., Egger, D. A., Kronik, L., Hodes, G. & Cahen, D. Hybrid Organic-Inorganic Perovskites: Low-Cost Semiconductors with Intriguing Charge-Transport Properties. *Nat. Rev. Mater.* **1**, 15007 (2016).

85. Weber, D. CH3NH3SnBrxI3-x (x = 0—3), ein Sn(II)-System mit kubischer Perowskitstruktur. *Zeitschrift fur Naturforschung - Section B Journal of Chemical Sciences* **33**, 862–865 (1978).

86. Weber, D. CH3NH3PbX3, ein Pb(II)-System mit kubischer Perowskitstruktur. *Zeitschrift fur Naturforschung - Section B Journal of Chemical Sciences* **33**, 1443–1445 (1978).

87. Stranks, S. D. & Snaith, H. J. Metal-Halide Perovskites for Photovoltaic and Light-Emitting Devices. *Nat. Nanotechnol.* **10**, 391–402 (2015).

88. Raghavan, C. M. *et al.* Low-Threshold Lasing from 2D Homologous Organic-Inorganic Hybrid Ruddlesden-Popper Perovskite Single Crystals. *Nano Lett.* **18**, 3221–3228 (2018).

89. Kim, H. *et al.* Enhanced Stability of $MAPbI_3$ Perovskite Solar Cells using Poly(*p*-chloro-xylylene) Encapsulation. *Sci. Rep.* **9**, 1–6 (2019).

90. Miyata, K., Atallah, T. L. & Zhu, X. Y. Lead halide perovskites: Crystal-liquid duality, phonon glass electron crystals, and large polaron formation. *Science Advances* **3**, (2017).

91. Pisoni, A. *et al.* Ultra-Low Thermal Conductivity in Organic–Inorganic Hybrid Perovskite $CH_3NH_3PbI_3$. *J. Phys. Chem. Lett.* **5**, 2488–2492 (2014).

92. *Testing and Measuring Equipment/Allowed Subcontracting Thin-Film Terrestrial Photovoltaic (PV) Modules-Design Qualification and Type Approval*. (International Electrotechnical Commission, 1998).

93. Stoumpos, C. C., Malliakas, C. D. & Kanatzidis, M. G. Semiconducting Tin and Lead Iodide Perovskites with Organic Cations: Phase Transitions, High Mobilities, and Near-Infrared Photoluminescent Properties. *Inorg. Chem.* **52**, 9019–9038 (2013).

94. Chen, Y., Zhao, Y. & Liang, Z. Solution processed organic thermoelectrics: towards flexible thermoelectric modules. *Energy & Environmental Science* **8**, 401–422 (2015).

95. Russ, B., Glaudell, A., Urban, J. J., Chabinyc, M. L. & Segalman, R. A. Organic thermoelectric materials for energy harvesting and temperature control. *Nature Reviews Materials 2016 1:10* **1**, 1–14 (2016).

96. Kee, S., Haque, M. A., Corzo, D., Alshareef, H. N. & Baran, D. Self-Healing and Stretchable 3D-Printed Organic Thermoelectrics. *Advanced Functional Materials* **29**, 1905426 (2019).

97. Zhu, H. *et al.* Screening in crystalline liquids protects energetic carriers in hybrid perovskites. *Science* **353**, 1409–1413 (2016).

98. Wang, M. & Lin, S. Anisotropic and Ultralow Phonon Thermal Transport in Organic–Inorganic Hybrid Perovskites: Atomistic Insights into Solar Cell Thermal Management and Thermoelectric Energy Conversion Efficiency. *Advanced Functional Materials* **26**, 5297–5306 (2016).

99. Hata, T., Giorgi, G. & Yamashita, K. The Effects of the Organic-Inorganic Interactions on the Thermal Transport Properties of CH3NH3PbI3. *Nano Letters* **16**, 2749–2753 (2016).

100. Whalley, L. D., Skelton, J. M., Frost, J. M. & Walsh, A. Phonon anharmonicity, lifetimes, and thermal transport in CH3NH3PbI3 from many-body perturbation theory. *Physical Review B* **94**, 220301 (2016).

101. Elbaz, G. A. *et al.* Phonon Speed, Not Scattering, Differentiates Thermal Transport in Lead Halide Perovskites. *Nano Lett.* **17**, 5734–5739 (2017).

102. Callaway, J. Model for Lattice Thermal Conductivity at Low Temperatures. *Physical Review* **113**, 1046 (1959).

103. Tse, J. S. & White, M. A. Origin of Glassy Crystalline Behavior in the Thermal Properties of Clathrate Hydrates: A Thermal Conductivity Study of Tetrahydrofuran Hydrate1. *J. Phys. Chem* **92**, 5006–5011 (1988).

104. Zhu, T. & Ertekin, E. Mixed phononic and non-phononic transport in hybrid lead halide perovskites: glass-crystal duality, dynamical disorder, and anharmonicity. *Energy & Environmental Science* **12**, 216–229 (2019).

105. Leguy, A. M. A. *et al.* The dynamics of methylammonium ions in hybrid organic–inorganic perovskite solar cells. *Nature Communications 2015 6:1* **6**, 1–11 (2015).

106. Wang, S., Jiang, Y., Juarez-Perez, E. J., Ono, L. K. & Qi, Y. Accelerated Degradation of Methylammonium Lead Iodide Perovskites Induced by exposure to Iodine Vapour. *Nat. Energy* **2**, 1–8 (2017).

107. Berhe, T. A. *et al.* Organometal Halide Perovskite Solar Cells: Degradation and Stability. *Energy Environ. Sci.* **9**, 323–356 (2016).

108. Alberti, A. *et al.* Similar Structural Dynamics for the Degradation of $CH_3NH_3PbI_3$ in Air and in Vacuum. *ChemPhysChem* **16**, 3064–3071 (2015).

109. Tsai, H. *et al.* High-efficiency two-dimensional ruddlesden-popper perovskite solar cells. *Nature* **536**, 312–317 (2016).

110. Han, Y. *et al.* Degradation Observations of Encapsulated Planar $CH_3NH_3PbI_3$ Perovskite Solar Cells at High Temperatures and Humidity. *J. Mater. Chem. A* **3**, 8139–8147 (2015).

111. Abdelmageed, G. *et al.* Effect of Temperature on Light Induced Degradation in Methylammonium Lead Iodide Perovskite Thin Films and Solar Cells. *Sol. Energy Mater. Sol. Cells* **174**, 566–571 (2018).

112. Conings, B. *et al.* Intrinsic Thermal Instability of Methylammonium Lead Trihalide Perovskite. *Adv. Energy Mater.* **5**, 1500477 (2015).

113. Brinkmann, K. O. *et al.* Suppressed Decomposition of Organometal Halide Perovskites by Impermeable Electron-Extraction Layers in Inverted Solar Cells. *Nat. Commun.* **8**, 1–9 (2017).

114. Ono, L. K. *et al.* Pinhole-Free Hole Transport Layers Significantly Improve the Stability of $MAPbI_3$-Based Perovskite Solar Cells under Operating Conditions. *J. Mater. Chem. A* **3**, 15451–15456 (2015).

115. Smith, I. C., Hoke, E. T., Solis-Ibarra, D., McGehee, M. D. & Karunadasa, H. I. A Layered Hybrid Perovskite Solar-Cell Absorber with Enhanced Moisture Stability. *Angew. Chem.* **126**, 11414–11417 (2014).

116. Myae Soe, C. M. *et al.* Structural and Thermodynamic Limits of Layer Thickness in 2D Halide Perovskites. *Proc. Natl. Acad. Sci. U. S. A.* **116**, 58–66 (2019).

117. Cao, D. H., Stoumpos, C. C., Farha, O. K., Hupp, J. T. & Kanatzidis, M. G. 2D Homologous Perovskites as Light-Absorbing Materials for Solar Cell Applications. *J. Am. Chem. Soc.* **137**, 7843–7850 (2015).

118. Fu, W., Chen, H. & Jen, A. K. Y. Two-dimensional perovskites for photovoltaics. *Materials Today Nano* **14**, 100117 (2021).

119. Mao, L. *et al.* Seven-Layered 2D Hybrid Lead Iodide Perovskites. *Chem* **5**, 2593–2604 (2019).

120. Stoumpos, C. C. *et al.* Ruddlesden-Popper Hybrid Lead Iodide Perovskite 2D Homologous Semiconductors. *Chem. Mater.* **28**, 2852–2867 (2016).

121. Gao, L. *et al.* Enhanced Charge Transport by Incorporating Formamidinium and Cesium Cations into Two-Dimensional Perovskite Solar Cells. *Angewandte Chemie* **131**, 11863–11867 (2019).

122. Liu, Z., Wang, L. & Xie, X. Improving the performance of inverted two-dimensional perovskite solar cells by adding an anti-solvent into the perovskite precursor. *Journal of Materials Chemistry C* **8**, 11882–11889 (2020).

123. Ravichandran, J. *et al.* Crossover from Incoherent to Coherent Phonon Scattering in Epitaxial Oxide Superlattices. *Nat. Mater.* **13**, 168–172 (2014).

124. Luckyanova, M. N. *et al.* Coherent Phonon Heat Conduction in Superlattices. *Science* **338**, 936–939 (2012).

125. Mauck, C. M. *et al.* Inorganic Cage Motion Dominates Excited-State Dynamics in 2D-Layered Perovskites $(C_xH_{2x+1}NH_3)_2PbI_4$ (x = 4-9). *J. Phys. Chem. C* **123**, 27904–27916 (2019).

126. Thouin, F. *et al.* Phonon Coherences Reveal the Polaronic Character of Excitons in Two-Dimensional Lead Halide Perovskites. *Nat. Mater.* **18**, 349–356 (2019).

127. Guo, Z., Wu, X., Zhu, T., Zhu, X. & Huang, L. Electron-Phonon Scattering in Atomically Thin 2D Perovskites. *ACS Nano* **10**, 9992–9998 (2016).

128. Maity, P. *et al.* Layer-Dependent Coherent Acoustic Phonons in Two-Dimensional Ruddlesden−Popper Perovskite Crystals. *J. Phys. Chem. Lett* **10**, 5259–5264 (2019).

129. Chernatynskiy, A., Grimes, R. W., Zurbuchen, M. A., Clarke, D. R. & Phillpot, S. R. Crossover in Thermal Transport Properties of Natural, Perovskite-Structured Superlattices. *Appl. Phys. Lett.* **95**, 161906 (2009).

130. Stoumpos, C. C. *et al.* High Members of the 2D Ruddlesden-Popper Halide Perovskites: Synthesis, Optical Properties, and Solar Cells of $(CH_3(CH_2)_3NH_3)_2(CH_3NH_3)_4Pb_5I_{16}$. *Chem* **2**, 427–440 (2017).

131. Onoda-Yamamuro, N., Matsuo, T. & Suga, H. Calorimetric and IR Spectroscopic Studies of Phase Transitions in Methylammonium Trihalogenoplumbates (II). *J. Phys. Chem. Solids* **51**, 1383–1395 (1990).

132. M.W. Chase Jr. *NIST-JANAF Thermochemical Tables*. *J. Phys. Chem. Ref. Data Monogr.* (American Institute of Physics, 1998).

133. Giri, A. *et al.* Ultralow Thermal Conductivity of Two-Dimensional Metal Halide Perovskites. *Nano Lett.* **20**, 3331–3337 (2020).

134. Ye, T. *et al.* Ultra-High Seebeck Coefficient and Low Thermal Conductivity of a Centimeter-Sized Perovskite Single Crystal Acquired by a Modified Fast Growth Method. *J. Mater. Chem. C* **5**, 1255–1260 (2017).

135. Smilgies, D. M. Grazing-Incidence X-Ray Scattering of Lamellar Thin Films. *J. Appl. Crystallogr.* **52**, 247–251 (2019).

136. Jiang, Z. GIXSGUI: A MATLAB Toolbox for Ggrazing-Incidence X-Ray Scattering Data Visualization and Reduction, and Indexing of Buried Three-Dimensional Periodic Nanostructured Films. *J. Appl. Crystallogr.* **48**, 917–926 (2015).

137. Zhang, X. *et al.* Phase Transition Control for High Performance Ruddlesden–Popper Perovskite Solar Cells. *Adv. Mater.* **30**, 1707166 (2018).

138. Dahlman, C. J. *et al.* Controlling Solvate Intermediate Growth for Phase-Pure Organic Lead Iodide Ruddlesden-Popper $(C_4H_9NH_3)_2(CH_3NH_3)_{n-1}Pb_nI_{3n+1}$ Perovskite Thin Films. *Chem. Mater.* **31**, 5832–5844 (2019).

139. Rasel, M. A. J. *et al.* Chain-Length Dependence of Thermal Conductivity in 2D Alkylammonium Lead Iodide Single Crystals. *ACS Appl. Mater. Interfaces* **12**, 53705–53711 (2020).

140. Qin, Y. *et al.* Coordination Engineering of Single-Crystal Precursor for Phase Control in Ruddlesden–Popper Perovskite Solar Cells. *Adv. Energy Mater.* **10**, 1904050 (2020).

141. Landry, E. S., Hussein, M. I. & McGaughey, A. J. H. Complex Superlattice Unit Cell Designs for Reduced Thermal Conductivity. *Phys. Rev. B: Condens. Matter Mater. Phys.* **77**, 184302 (2008).

142. Broido, D. A., Malorny, M., Birner, G., Mingo, N. & Stewart, D. A. Intrinsic Lattice Thermal Conductivity of Semiconductors from First Principles. *Appl. Phys. Lett.* **91**, 231922 (2007).

143. Lindsay, L., & Broido, D. A. Three-Phonon Phase Space and Lattice Thermal Conductivity in Semiconductors. *J. Phys.: Condens. Matter* **20**, 165209 (2008).

144. Kmiecik, S. *et al.* Coarse-Grained Protein Models and Their Applications. *Chem. Rev.* **116**, 7898–7936 (2016).

145. Beecher, A. N. *et al.* Direct Observation of Dynamic Symmetry Breaking above Room Temperature in Methylammonium Lead Iodide Perovskite. *ACS Energy Lett.* **1**, 880–887 (2016).

146. Guo, P. *et al.* Cross-Plane Coherent Acoustic Phonons in Two-Dimensional Organic-Inorganic Hybrid Perovskites. *Nat. Commun.* **9**, 1–9 (2018).

147. United Nations Environment Programme. The Importance of Energy Efficiency in the Refrigeration, Air-conditioning and Heat Pump Sectors. (2018).

148. Molenbroek, E., Smith, M., Surmeli, N. & Schimschar, S. European Commission Savings and benefits of global regulations for energy efficient products. (2015).

149. Mañosa, L. & Planes, A. Materials with Giant Mechanocaloric Effects: Cooling by Strength. *Advanced Materials* **29**, 1603607 (2017).

150. Scott, J. F. Electrocaloric Materials. *Annual Review of Materials Research* **41**, 229–240 (2011).

151. Shen, B. G., Sun, J. R., Hu, F. X., Zhang, H. W. & Cheng, Z. H. Recent Progress in Exploring Magnetocaloric Materials. *Advanced Materials* **21**, 4545–4564 (2009).

152. Lu, B. & Liu, J. Mechanocaloric materials for solid-state cooling. *Science Bulletin* **60**, 1638–1643 (2015).

153. Pecharsky, V. K. & Gschneidner, K. A. Giant Magnetocaloric Effect in Gd 5 Si 2 Ge 2. (1997).

154. Mañosa, L. & Planes, A. Solid-state cooling by stress: A perspective. *Applied Physics Letters* **116**, 050501 (2020).

155. Mañosa, L. *et al.* Giant solid-state barocaloric effect in the Ni–Mn–In magnetic shape-memory alloy. *Nature Materials 2010 9:6* **9**, 478–481 (2010).

156. Ekkes Bruck. Developments in magnetocaloric refrigeration. *Journal of Physics D: Applied Physics* **38**, R381 (2005).

157. Busico, V., Carfagna, C., Salerno, V., Vacatello, M. & Fittipaldi, F. The layer perovskites as thermal energy storage systems. *Solar Energy* **24**, 575–579 (1980).

158. Arend, H., Tichy, K., Baberschke, K. & Rys, F. Chloride perovskite layer compounds of [NH3-(CH2)n-NH3]MnCl4 formula. *Solid State Communications* **18**, 999–1003 (1976).

159. Paraggio, C., Salerno, V., Busico, V. & Vacatello, M. The thermal behaviour of mixed long chain alkylammonium tetrachloromanganates(II). *Thermochimica Acta* **42**, 185–191 (1980).

160. Li, J. *et al.* Colossal Reversible Barocaloric Effects in Layered Hybrid Perovskite (C10H21NH3)2MnCl4 under Low Pressure Near Room Temperature. *Advanced Functional Materials* **31**, 2105154 (2021).

161. Mason, J. *et al.* Colossal Barocaloric Effects with Ultralow Hysteresis in Two-Dimensional Metal-Halide Perovskites. (2021) doi:10.21203/rs.3.rs-426701/v1.

162. Hsu, T. H. *et al.* Thermal hysteresis in phase-change materials: Encapsulated metal alloy core-shell microparticles. *Nano Energy* **51**, 563–570 (2018).

163. Duan, X., Li, Z., Liu, J., Chen, G. & Li, X. Roles of kink on the thermal transport in single polyethylene chains. *Journal of Applied Physics* **125**, 164303 (2019).

164. Bergantin, S., Moret, M., Buth, G. & Fabbiani, F. P. A. Pressure-induced conformational change in organic semiconductors: Triggering a reversible phase transition in rubrene. *Journal of Physical Chemistry C* **118**, 13476–13483 (2014).

165. Liu, J. & Yang, R. Tuning the thermal conductivity of polymers with mechanical strains. *Physical Review B - Condensed Matter and Materials Physics* **81**, 174122 (2010).

166. Wang, R. Y., Segalman, R. A. & Majumdar, A. Room temperature thermal conductance of alkanedithiol self-assembled monolayers. *Applied Physics Letters* **89**, 173113 (2006).

167. Meier, T. *et al.* Length-dependent thermal transport along molecular chains. *Physical Review Letters* **113**, 060801 (2014).

168. Losego, M. D., Grady, M. E., Sottos, N. R., Cahill, D. G. & Braun, P. v. Effects of chemical bonding on heat transport across interfaces. *Nature Materials 2012 11:6* **11**, 502–506 (2012).

169. Simkin, M. v & Mahan, G. D. Minimum Thermal Conductivity of Superlattices. *Phys. Rev. Lett.* **84**, 927–930 (2000).